

6.78MHz Omnidirectional Wireless Power Transfer System  
for Portable Devices Application

Junjie Feng

Dissertation submitted to the Faculty of  
Virginia Polytechnic Institute and State University  
in partial fulfillment of the requirements for the degree of

Doctor of Philosophy  
in  
Electrical Engineering

Qiang Li, Chair  
Fred C. Lee  
Majid Manteghi  
Virgilio A. Centeno  
Steve C. Southward

Nov. 9<sup>th</sup>, 2020  
Blacksburg, Virginia

Keywords: Wireless Power Transfer, Magnetic Field, Resonant  
Converter, High Frequency, Soft-switching, Shielding  
Copyright © 2020 Junjie Feng

# 6.78MHz Omnidirectional Wireless Power Transfer System for Portable Devices Application

Junjie Feng

## Abstract

Wireless power transfer (WPT) with loosely coupled coils is a promising solution to deliver power to a battery in a variety of applications. Due to its convenience, wireless power transfer technology has become popular in consumer electronics. Thus far, the majority of the coupled coils in these systems are planar structure, and the magnetic field induced by the transmitter coil is in one direction, meaning that the energy power transfer capability degrades greatly when there is some angle misalignment between the coupled coils.

To improve the charging flexibility, a three-dimensional (3D) coils structure is proposed to transfer energy in different directions. With appropriate modulation current flowing through each transmitter coil, the magnetic field rotates in different directions and covers all the directions in 3D space. With omnidirectional magnetic field, the charging platform can provide energy transfer in any direction; therefore, the angle alignment between the transmitter coil and receiver coil is no longer needed.

Compensation networks are normally used to improve the power transfer capability of a WPT system with loosely coupled coils. The resonant circuits, formed by the loosely coupled coils and external compensation inductors or capacitors, are crucial in the converter design. In WPT system, the coupling coefficient between the transmitting coil and the receiving coil is subject to the receiver's positioning. The variable coupling condition is a big challenge to the resonant topology

selection. The detailed requirements of the resonant converter in an omnidirectional WPT system are identified as follows: 1). coupling independent resonant frequency; 2). load independent output voltage; 3). load independent transmitter coil current; 4). maximum efficiency power transfer; 5). soft switching of active devices. A LCCL-LC resonant converter is derived to satisfy all of the five requirements.

In consumer electronics applications, Megahertz (MHz) WPT systems are used to improve the charging spatial freedom. 6.78 MHz is selected as the system operation in AirFuel standard, a wireless charging standard for commercial electronics. The zero voltage switching (ZVS) operation of the switching devices is essential in reducing the switching loss and the switching related electromagnetic interference (EMI) issue in a MHz system; therefore, a comprehensive evaluation of ZVS condition in an omnidirectional WPT system is performed. And a design methodology of the LCCL-LC converter to achieve ZVS operation is proposed.

The big hurdle of the WPT technology is the safety issue related to human exposure of electromagnetic fields (EMF). A double layer shield structure, including a magnetic layer and a conductive layer, is proposed in a three dimensional charging setup to reduce the stray magnetic field level. A parametric analysis of the double shield structure is conducted to improve the attenuation capability of the shielding structure.

In an omnidirectional WPT system, the energy can be transferred in any direction; however the receiving devices has its preferred field direction based on its positioning and orientation. To focus power transfer towards targeted loads, a smart detection algorithm for identifying the positioning and orientation of receiver devices based on the input power information is presented. The system efficiency is further improved by a maximum efficiency point tracking function. A

novel power flow control with a load combination strategy to charge multiple loads simultaneously is explained. The charging speed of the omnidirectional WPT system is greatly improved with proposed power flow control.

# 6.78MHz Omnidirectional Wireless Power Transfer System for Portable Devices Application

Junjie Feng

## General Audience Abstract

Wireless power transfer (WPT) is a promising solution to deliver power to a battery in a variety of applications. Due to its convenience, wireless power transfer technology with loosely coupled coils has become popular in consumer electronics. In such system, the receiving coil embedded in the receiving device picks up magnetic field induced by the transmitter coil; therefore, energy is transferred through the magnetic field and contactless charging is achieved. Thus far, the majority of the coupled coils in these systems are planar structure, and the magnetic field induced by the transmitter coil is in one direction, meaning that the energy power transfer capability degrades greatly when there is some angle misalignment between the coupled coils.

To improve the charging flexibility, a three-dimensional (3D) coils structure is proposed to transfer energy in different directions, also known as in omnidirectional manner. With omnidirectional magnetic field, the charging platform can provide energy transfer in any direction; therefore, the angle alignment between the transmitter coil and receiver coil is no longer needed.

In a WPT system with loosely coupled coils, the energy transfer capability suffers from weak coupling condition. To improve the power transfer capability, the electrical resonance concept between the inductor and capacitor at the power transfer frequency is adopted. A novel compensation network is proposed to form a resonant tank with the loosely coupled coils and maximize the power transfer at the operating frequency.

As for the WPT system with loosely coupled coils, the energy transfer capability is also proportional to the operating frequency. Therefore, Megahertz (MHz) WPT systems are used to improve the charging spatial freedom. 6.78 MHz is selected as the system operation in AirFuel standard, a wireless charging standard for commercial electronics. The zero voltage switching (ZVS) operation of the switching devices is essential in reducing the switching loss and the switching related electromagnetic interference (EMI) issue in a MHz system; therefore, a comprehensive evaluation of ZVS condition in an omnidirectional WPT system is performed.

The big hurdle of the WPT technology is the safety concern related to human exposure of electromagnetic fields (EMF). Therefore, a double layer shield structure is first applied in a three dimensional charging setup to confine the electromagnetic fields effectively. The stray field level in our charging platform is well below the safety level required by the regulation agent.

Although the energy can be transferred in an omnidirectional manner in the proposed charging platform, the energy should be directed to the target loads to avoid unnecessary energy waste. Therefore, a smart detection method is proposed to detect the receiver coil's orientation and focus the energy transfer to certain direction preferred by the receiver in the setup. The energy beaming strategy greatly improves the charging speed of the charging setup.

***To My Parents:***

*Shaolian Feng and Guoxia Cai*

***To My Wife***

*Xin Ning*

## Acknowledgement

First and foremost, I would like to thank my advisor, Dr. Qiang Li and my committee member, Dr. Fred Lee, for their guidance and education during the past six years. It is their profound knowledge, rich experience, and rigorous attitude to research that help me finish this work. The challenging spirit they taught me is a lifetime treasure and I will carry it in the future career.

I am also grateful to my other committee members Dr. Majid Manteghi, Dr. Virgilio Centeno and Dr. Steve Southward for their insightful comments and suggestions during the preliminary examination and the final defense.

I want to express my gratitude to all the amazing faculty and staffs in CPES: Dr. Dushan Boroyevich, Dr. Rolando Burgos, Dr. Khai Ngo, Dr. Guo-Quan Lu, Dr. Yuhao Zhang, Dr. Bo Wen, Dr. David Gilham, Dr. Igor Cvetkovic, Ms. Teresa Shaw, Ms. Trish Rose, Ms. Marianne Hawthorne, Ms. Linda Long, Ms. Lauren Shutt, Ms. Na Ren, Ms. Yan Sun, Ms. Audri Cunningham, Mr. Matthew Scanland, Mr. Gennis Grove. Thank you all for the kind support and help.

A special thanks to Dr. Xiucheng Huang, who mentored me since the first day I came to CPES. His hands-on experience benefits me a lot and his attitude to life encourages me during all the tough times in the past six years.

I also want to thank all my colleagues in the CPES: Dr. Mingkai Mu, Dr. Shuilin Tian, Dr. Zhengyang Liu, Dr. Yang Jiao, Dr. Jun Wang, Dr. Yucheng Yang, Dr. Dongbin Hou, Dr. Zheming Zhang, Dr. Chao Fei, Dr. Qiong Wang, Dr. Chi Li, Dr. Ming Lu, Dr. Bingyao Sun, Dr. Syed Bari, Dr. Niloofar Rashidimehrabadi, Dr. Christina DiMarino, Dr. Sunjae Ohn, Dr. Bin Li, Dr. Ting Ge,

Dr. Zichen Miao, Dr. Mohamed Ahmed, Dr. Lujie Zhang, Dr. Yi-Hsum Hsieh, Dr. Chien-An Chen, Dr. Zhengrong Huang, Mr. Shishuo Zhao, Mr. Tao Liu, Mr. Yadong Lyu, Ms. Virginia Li, Ms. Ye Tang, Mr. Jianghui Yu, Mr. Slavko Mocevic, Mr. Joseph Koazk, Ms. Ye Fan, Ms. Weizhen Sun, Mr. Rimon Gaderlrab, Mr. Shuo Wang, Mr. Feiyang Zhu, Mr. Yinsong Cai, Mr. Zheqing Li, Mr. Xin Lou, Mr. Feng Jin, Mr. Chunyang Zhao, Mr. Gibong Son, Mr. Ahmed Naibh, Mr. Ding Chao, Mr. Shengchang Lu, Mr. Keyao Sun, Ms. Le Wang, Mr. Lee Gill, Ms. Yingying Gui, Ms. Jiewn Hu, Mr. Cong Tu, Mr. Bo Li, Ms. Tianyu Zhao, Ms. Grace Watt, Ms. Emma Raszmann, Mr. Xingyu Chen, Mr. Tianlong Yuan, Mr. Ruizhe Zhang, Mr. Boyan Wang, . We shared so many valuable discussions and happiness during the past six years. It is a wonderful experience to become friends with you. All the best, my dear friends.

Many intelligent visitor scholars came and left in these years. Among them, special thanks go to Dr. Minfan Fu since we have worked in the same project and shared so many precious memories together. I also want to thank Mr. Jincun Liu for the happiness and joy we shared together during playing basketball. Thanks all the visiting scholars for their expertise and valuable comments for my research.

Last but not least, I want to sincerely thank all my family members: my father Shaolian Feng, my mother Guoxia Cai, my wife Xin Ning and my sister Yuping Feng. It is your love, understanding and encouragement which supports me during the past years.

# Table of Contents

<b>Chapter 1</b>	<b>Introduction .....</b>	<b>1</b>
1.1	Background of Wireless Power Transfer Technology .....	1
1.2	Overview of Wireless Power Transfer Technologies .....	4
1.3	Inductive Power Transfer Technology.....	6
1.4	High Frequency Operation vs. Low Frequency Operation.....	10
1.5	From Directional WPT system to Omnidirectional WPT system .....	12
1.6	Challenges in Omnidirectional WPT system.....	13
1.6.1	Transmitter Coils Structure to Generate Omnidirectional Field Distribution .	13
1.6.2	Effective Power Transfer under Weak and Variable Coupling Condition .....	14
1.6.3	Stray Field Reduction for Human Health .....	17
1.6.4	Intelligent Charging Strategy.....	18
1.7	Proposed Dissertation Outline .....	19
<b>Chapter 2</b>	<b>Transmitter Coils Structure for Omnidirectional WPT System.....</b>	<b>21</b>
2.1	Introduction.....	21
2.2	Proposed Wireless Charging Bowl .....	23
2.2.1	Magnetic Field Preference in a Charging Bowl .....	23
2.2.2	Proposed Transmitter Coils Structure.....	24
2.3	Transmitter Coils Optimization .....	27

2.4	Experiment Verification.....	36
2.5	Conclusion .....	43
<b>Chapter 3 6.78MHz Resonant Converter for Omnidirectional WPT System .....</b>		<b>45</b>
3.1	Introduction.....	45
3.2	Synthesis of Multiple Element Resonant Converter.....	49
3.3	Experiment Verification.....	53
3.4	Conclusion .....	57
<b>Chapter 4 Soft-switching Realization of the 6.78MHz LCCL-LC Converter.....</b>		<b>58</b>
4.1	Introduction.....	58
4.2	Reactance of Full Bridge Rectifier at 6.78MHz .....	59
4.3	ZVS Achievement in One Transmitter Coil Case.....	62
4.3.1	Parameter Design for ZVS Operation .....	62
4.3.2	Turn-off current Calculation.....	64
4.3.3	Considering effect of the dead-time period .....	70
4.4	ZVS Analysis in Multiple Transmitter Coils Case .....	72
4.4.1	Identify the worst case for method I.....	76
4.4.2	Identify the worst case for method II.....	77
4.5	Experiment Verification.....	81
4.5.1	One transmitter coil case .....	81
4.5.2	Two transmitter coil case.....	85

4.6	Conclusion .....	89
<b>Chapter 5 Stray Field Reduction for Human Health .....</b>		<b>91</b>
5.1	Introduction.....	91
5.2	A Square-shaped Wireless Charging Bowl.....	92
5.3	Shielding Study of the Wireless Charging Bowl .....	96
5.3.1	Single Layer Magnetic Shield .....	97
5.3.2	Double Layer Shield Structure .....	100
5.4	Experimental Verification.....	104
5.5	Conclusion .....	106
<b>Chapter 6 Intelligent Charging Strategy .....</b>		<b>108</b>
6.1	Introduction.....	108
6.2	Omnidirectional Wireless Charging Bowl System Structure .....	109
6.3	Control Algorithm for the Omnidirectional WPT System.....	116
6.3.1	Review of State-of-Art Control Algorithm .....	116
6.3.2	Proposed Smart Detection Algorithm .....	117
6.3.3	Maximum Efficiency Tracking Function .....	123
6.3.4	Power Flow Control.....	124
6.4	Experimental Verification.....	126
6.4.1	Smart Detection Algorithm Verification .....	128
6.4.2	Maximum Efficiency Tracking Function Verification .....	129

6.4.3	Power Flow Control Verification .....	130
6.5	Conclusion .....	135
<b>Chapter 7</b>	<b>Summary .....</b>	<b>136</b>
<b>Reference</b>	<b>.....</b>	<b>139</b>
<b>Appendix: A Planar Omnidirectional Wireless Power Transfer System.....</b>		<b>149</b>
A.1	Introduction.....	149
A.2	Proposed Planar Transmitter Coils Structure.....	150
A.3	Reduce Parasitic Capacitances.....	153
A.4	Experimental Results .....	156

# List of Figures

Fig. 1-1. Telsa’s public demonstrations of wireless power transfer in 1891. ....	1
Fig. 1-2. Global unit shipments of wireless charging devices from 2014 to 2018. (Source from IHS Markit)....	3
Fig. 1-3. Capacitive coupling wireless power transfer system diagram. ....	5
Fig. 1-4. Inductive power transfer concept with loosely coupled coils. ....	6
Fig. 1-5. The circuit model of loosely coupled coils. (a). Original circuit model. (b). Decoupled circuit model. .	7
Fig. 1-6. The decoupled circuit model of the loosely coupled coils with compensation capacitor.....	8
Fig. 1-7. A general system structure of a loosely coupled coils system.....	9
Fig. 1-8. Two charging scenario for smart phone device of a commercial Qi charging pad. (a). There is no misalignment between transmitter and receiver. (b). There is misalignment between transmitter and receiver. ....	11
Fig. 1-9. Two charging scenario for wearable device of a planar charging pad (a). Receiver device is in perpendicular with the magnetic field. (b). Receiver device is in parallel with the magnetic field. ....	12
Fig. 1-10. The field distribution with loosely coupled coils [48].....	17
Fig. 1-11. An omnidirectional wireless charging setup with multiple receiver devices. ....	19
Fig. 2-1. Transmitter coils structure reported in [13]. (a). Transmitter coils structure. (b). The magnetic field trajectory at point O. (c). The magnetic field trajectory at point A.....	23
Fig. 2-2. Magnetic field preference for different devices in charging bowl. ....	24
Fig. 2-3. Proposed transmitter coils structure for the wireless charging bowl.....	25
Fig. 2-4. Magnetic field distribution of the side coil. (a) On the side face. (b) At the base. ....	25
Fig. 2-5. Magnetic field distribution at the base of the proposed charging bowl at different time instant. (a) $\omega_1 t = \pi / 10, \omega_0 t = \pi / 4$ . (b) $\omega_1 t = \pi / 8, \omega_0 t = 7\pi / 4$ . (c) $\omega_1 t = 5\pi / 4, \omega_0 t = 15\pi / 8$ . ....	26
Fig. 2-6. Magnetic field trajectory at two example points. (a) At $O_1$ . (b) At $O_2$ . ....	27
(b) Fig. 2-7. Geometry of the charging bowl fixture and side coil 1. (a) 3D view. (b) Side view. ....	29
Fig. 2-8. Target zone of the charging bowl for the side coil 1 optimization. ....	30
Fig. 2-9. $B_{avg}$ - $B_{std}$ Pareto Frontier result for the side coil 1 optimization. ....	32
Fig. 2-10. Field distribution at the base plane after the optimization. ....	32

Fig. 2-11. $ B_y $ distribution at the base plane. (a) Before the coil optimization. (b) After the coil optimization.	33
Fig. 2-12. Geometry of the bottom coil 5 in the charging bowl.....	34
Fig. 2-13. $\mu$ - $\sigma$ Pareto Frontier of the bottom coil optimization.....	34
Fig. 2-14. The transmitter coils structure after the optimization. ....	35
Fig. 2-15. Field distribution at the base with the optimized coil 5. ....	35
Fig. 2-16. Magnetic field distribution at different time instant with optimized coils structure. (a) $\omega_1 t = \pi / 10, \omega_0 t = \pi / 4$ . (b) $\omega_1 t = \pi / 8, \omega_0 t = 7\pi / 4$ . (c) $\omega_1 t = 5\pi / 4, \omega_0 t = 15\pi / 8$ . ....	36
Fig. 2-17. Magnetic field trajectory at two example points after the coil optimization. (a) At $O_1$ . (b) At $O_2$ .....	36
Fig. 2-18. Experiment setup of proposed omnidirectional WPT system.....	37
Fig. 2-19. Experiment waveform of modulated transmitter coils excitation current in proposed omnidirectional WPT system. ....	37
Fig. 2-20. The magnetic field trajectory at point $O_1$ . (a) During $T_a$ . (b) During $T_b$ .....	38
Fig. 2-21. The magnetic field trajectory measurement result. (a) At $O_1$ . (b) At $O_2$ .....	39
Fig. 2-22. Possible positioning of a receiver coil for wearable devices. ....	40
Fig. 2-23. Output voltage measurement results for an apple watch receiver. (a) When laying on the base. (b) When standing on the base. ....	41
Fig. 2-24. Smart phone receiver positioning description parameter $(\theta_1, \theta_2)$ .....	42
Fig. 2-25. Output voltage and efficiency measurement result for smart phone receiver with different positioning. (a). Output voltage; (b). Efficiency. ....	43
Fig. 3-1. The series – series compensated converter. ....	46
Fig. 3-2. Voltage gain curves of a SS compensated converter under different coupling condition. (a) $k = 0.4$ . (b) $k = 0.2$ . ....	46
Fig. 3-3. The LLC resonant converter. ....	48
Fig. 3-4. Voltage gain curves of a LLC converter under different coupling condition. (a) $k = 0.4$ . (b) $k = 0.2$ . ....	48
Fig. 3-5. The general ac circuit model of a wireless power transfer system.....	49
Fig. 3-6. Parallel resonant tank and its equivalent circuit with the Norton's equivalent circuit. ....	50
Fig. 3-7. Two resonant converter candidates. (a) LCCL-LC resonant converter. (b) CLCL-LC resonant converter. ....	52

Fig. 3-8. Voltage gain curves of the LCCL-LC converter under different coupling coefficient. (a) $k = 0.4$ . (b) $k = 0.2$ . .....	53
Fig. 3-9. The physical setup of the omnidirectional IPT system. ....	55
Fig. 3-10. Experimental waveform of switching node voltage and current. ....	55
Fig. 3-11. Experimental and calculated results of the <i>rms</i> current of transmitter coil and the output voltage. (a) $k = 0.12$ . (b) $k = 0.2$ . ....	56
Fig. 4-1. The LCCL-LC resonant converter.....	60
Fig. 4-2. Voltage and current waveform at the input port of the rectifier. ....	60
Fig. 4-3. Equivalent circuit of the LCCL-LC converter with fundamental approximation.....	60
Fig. 4-4. The voltage and current waveform of the rectifier with the fundamental approximation.....	61
Fig. 4-5. The relationship of $\sin(2\theta)/(2\theta)$ versus $\theta/\pi$ .....	62
Fig. 4-6. The voltage and current waveform of the rectifier with the fundamental approximation.....	64
Fig. 4-7. Equivalent circuit of the LCCL-LC converter with secondary side circuit reflected to primary side. ....	65
Fig. 4-8. Decomposition of the input current waveform in time domain. ....	66
Fig. 4-9. Turn off current of the designed system under different coupling coefficient and output power information. ....	70
Fig. 4-10. Simplified equivalent circuit for the discharging of the junction cap of the switching devices during the dead-time period. ....	71
Fig. 4-11. Transmitter coils and a receiver coil in an omnidirectional WPT system. (a). 3D view. (b). Top View. ....	72
Fig. 4-12. Two phase LCCL-LC circuit diagram with two transmitter coils. ....	73
Fig. 4-13. Equivalent decoupled circuit at fundamental frequency.....	73
Fig. 4-14. Mutual inductance between receiver coil and transmitter coils 1a, coil 2a ( $M_1, M_2$ ) versus under different yaw angle $\theta_y$ of the receiver. ....	76
Fig. 4-15. Turn off current of two transmitter circuits versus different yaw angle $\theta_y$ of the wearable receiver for modulation method I. ....	77

Fig. 4-16. Turn off current of two transmitter circuits versus different yaw angle $\theta_y$ of the receiver for modulation method II when $M_3 = 0$ .	78
Fig. 4-17. Normalized turn off current of two transmitter circuits versus different yaw angle $\theta_y$ of the receiver for modulation method II when $M_3 \neq 0$ ( $k_3 = 0.05$ ).	80
Fig. 4-18. The physical setup of the omnidirectional WPT system.	81
Fig. 4-19. Experimental switching node voltage and current waveform for one transmitter (coil 1a excited) and one receiver case (smart phone receiver Rx). (a). $k = 0.24$ , $P_o = 5W$ (Worst case). (b). $k = 0.12$ , $P_o = 5W$ . (c). $k = 0.24$ , $P_o = 2W$ .	83
Fig. 4-20. Efficiency of the LCCL-LC converter in one transmitter case.	83
Fig. 4-21. Experimental switching node voltage and current waveforms under $k = 0.2$ , $P_o = 5W$ . (a) ZVS case. (b). Non ZVS case.	85
Fig. 4-22. Loss breakdown of the converter for ZVS and non-ZVS case. (Unit: W)	85
Fig. 4-23. Experimental switching node voltage and current waveform for two transmitter and one receiver case with excitation current method I. (a). $\theta_y = 0^\circ$ , $P_o = 2.5W$ . (b). $\theta_y = 45^\circ$ , $P_o = 2.5W$ (worst case for channel I). (c). $\theta_y = 135^\circ$ , $P_o = 2.5W$ (worst case for channel II).	87
Fig. 4-24. Experimental switching node voltage and current waveform for two transmitter and one receiver case with excitation current method II. (a). $\theta_y = 100^\circ$ , $P_o = 2.5W$ ( $M_1/M_2 = 5$ , worst case for channel II). (b). $\theta_y = 135^\circ$ , $P_o = 2.5W$ . (c). $\theta_y = 170^\circ$ , $P_o = 2.5W$ ( $M_2/M_1 = 5$ , worst case for channel I).	89
Fig. 4-25. System efficiency versus different yaw angle of the receiver for two transmitter and one receiver case.	89
Fig. 5-1. The transmitter coils structure.	93
Fig. 5-2. Smart phone receiver positioning description parameter ( $\theta_1, \theta_2$ ).	93
Fig. 5-3. Coupling coefficient ( $k$ ) between transmitter coil 1 and the receiver coil under different positioning of the receiver coil.	94
Fig. 5-4. The proposed coils structure in a square-shaped charging bowl.	95
Fig. 5-5. Receiver positioning index $d$ definition.	95
Fig. 5-6. Coupling coefficient ( $k$ ) between transmitter coil 1 and the receiver coil under different positioning of the receiver coil.	96

Fig. 5-7. Field distribution in YZ plane in the square-shaped charging bowl. ....	97
Fig. 5-8. Field distribution in YZ plane with single layer ferromagnetic shield. ....	98
Fig. 5-9. Field distribution along $z = -0.05\text{m}$ for different $u_r$ . ....	99
Fig. 5-10. $B_{pk}$ at $(0, 0.12\text{m}, -0.05\text{m})$ v.s. different $u_r$ and thickness. ....	99
Fig. 5-11. Field distribution in YZ plane with a double layer shield. ....	101
Fig. 5-12. The impact of conductive layer on field distribution. ....	102
Fig. 5-13. The impact of the ferrite layer on field distribution. ....	103
Fig. 5-14. $B_{pk}$ at $(0, 0.05\text{m}, -0.05\text{m})$ v.s. different $u_r$ and thickness. ....	103
Fig. 5-15. The picture of the measurement setup. (a). Top view; (b). Side view with near field probe. ....	105
Fig. 6-1. Transmitter coils structure of an omnidirectional WPT system. ....	110
Fig. 6-2. Proposed system structure for the omnidirectional WPT charging bowl system. ....	112
Fig. 6-3. Switching node voltage and transmitter coil current waveforms under different modulation components. (a). Positive modulation component; (b). Negative modulation component. ....	113
Fig. 6-4. The waveforms under exciting three transmitter coils one by one in the example receiver positioning scenario of Fig. 6-2 . ....	118
Fig. 6-5. The waveforms under exciting the transmitter coil 1 and coil 2 together with modulated excitation in the example receiver positioning scenario of Fig. 6-2 . ....	119
Fig. 6-6. The waveform for identifying the load information transferred to Rx 1 in two transmitter coil 1 and 2 excitation case. ....	120
Fig. 6-7. The input power information for transmitter coil 1 and coil excitation case after subtracting load power transferred to Rx 1. ....	120
Fig. 6-8. The magnetic field directions in xy plane when the transmitter coil 1 and coil 2 are excited simultaneously in step II. ....	122
Fig. 6-9. The circuit diagram under one transmitter and one receiver case. ....	123
Fig. 6-10. The picture of the experiment setup. ....	127
Fig. 6-11. Experimental waveforms for smart detection algorithm. ....	129
Fig. 6-12. Experimental waveforms for the maximum efficiency tracking function for Rx 1. ....	130
Fig. 6-13. Experimental waveforms for the load combination strategy. ....	130

**Fig. 6-14. The picture of receiver positioning under different test scenarios. (a). Case I. (b). Case II. (c). Case III. (d). .....132**

**Fig. 6-15. Experimental waveforms for smart detection algorithm under different cases. (a). Case I. (b) Case II. (c). Case III. (d). Case IV. ....134**

# List of Tables

<b>Table 1.1 Summary of Omnidirectional IPT system in existing Literature .....</b>	<b>14</b>
<b>Table 3.1 Spectifications of the WPT System.....</b>	<b>54</b>
<b>Table 4.1 Spectifications of the WPT System.....</b>	<b>68</b>
<b>Table 4.2 Passive Component Values in the LCCL-LC Converter .....</b>	<b>69</b>
<b>Table 5.1 FCC Part 1 Field Limintation.....</b>	<b>96</b>
<b>Table 5.2 The Parameter of the coupled coils in the system .....</b>	<b>105</b>
<b>Table 5.3 The magnetic field strength at point A.....</b>	<b>106</b>
<b>Table 6.1 Parameter of Passive Components in the System.....</b>	<b>127</b>
<b>Table 6.2 Summary for Test Result Under Different Cases.....</b>	<b>132</b>

# Chapter 1 Introduction

## 1.1 Background of Wireless Power Transfer Technology

James Clerk Maxwell, a greatest physicist of all time, formulated the classical theory of electromagnetic wave in 1865 [1]. Maxwell's equations lay the foundation for the electromagnetic wave study. About 20 years later, Heinrich Rudolf Hertz proved the existence of the electromagnetic waves by a series of experiments [2]. Soon afterwards, the first wireless telegraphy system was invented by Guglielmo Marconi in 1897 [3]. Instead of transmitting information, Nicolas Tesla aimed at transferring energy through the electromagnetic wave [4]. He invented the resonant transformer later called as the Tesla coil to transfer energy wirelessly. He conducted several public demonstrations where he powered Geissler tubes wirelessly as shown in [5]. He hoped to build the Wardenclyffe World Wireless system station and transmit power wirelessly to the users. Unfortunately, the project is not finished because of lack of finance. Even though Tesla's pioneering work is not commercialized at the time, his idea inspired many engineers afterwards.

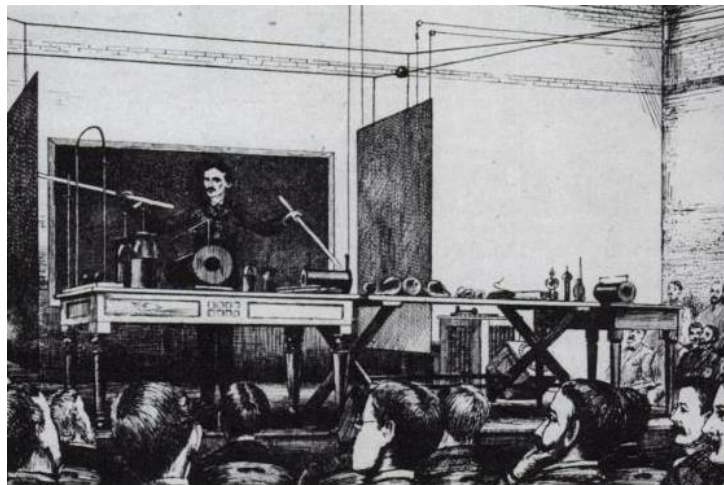


**Fig. 1-1. Tesla's public demonstrations of wireless power transfer in 1891.**

In the middle of 20<sup>th</sup> century, the wireless charging technology is evaluated for electric vehicles. However, the technology is not commercialized because the system frequency is very low (around 400 Hz) considering the absence of fast semiconductor devices, good ferrite material and litz wires [6]. The low frequency operation leads to a large coil current of thousands amperes, a heavy power supply, large pick up coils and a high construction cost, large acoustic noises and low system efficiencies. Therefore, the wireless charging technology is not commercialized for the electric vehicles at that time.

In late 20<sup>th</sup> century, the litz wire technology and semiconductor technology is proposed in power electronics field [7]. With these technology, it is possible to push the system operation frequency to kHz range with low cost. With high frequency operation, it is easier to transfer the energy with the electromagnetic wave and therefore the wireless power technologies are re-gained the attention of the engineers. The wireless charging technology is applied in the transcutaneous energy systems for medical implants [8] [9] and induction heaters [10] since 1970s. Soon afterwards, the wireless charging technology attracted much attention for portable equipment. Due to the special water-proof requirement, wireless charging with inductive power transfer technology for electric toothbrush is commercialized successfully in the market. In addition, the “Qi” standard was launched by the Wireless Power Consortium to define the inductive power transfer technology for consumer electronics. Since then, the wireless charging technology shows promising future for portable devices applications [11].

Coming to the era of 21<sup>st</sup> century, the Internet of Things (IoT) devices are gaining popularity in the everyday life of most people [12]. Gartner forecasts that 11.2 billion connected things will be in use worldwide in 2018 and by 2020 will reach 20.4 billion [13]. Most of the IoT devices is powered by a lithium battery and the battery needs to be charged periodically. Right now, the

common method to charge the battery is using a conductive wires. The power transfer with wire is simple; however, the wireless charging technology has demonstrated unique advantages in consumer electronics. First of all, it is convenient to charge the devices without any plug, especially for those devices requiring frequent charging. For example, a wireless charging for a smart phone device can provide great convenience for the users. Secondly, the wireless charging technology is reliable in wet, dirty and flammable environment. Thirdly, a seamless design is desired for some IoT devices and the wireless charging technology provides such opportunity for consumer electronics. Considering these advantages, the wireless charging technology is promising and it could lead to a technological revolution for the power supply for portable devices application. Therefore, the wireless charging technology has been studied intensely in recent years due to the large market potential. The global shipments of consumer devices with wireless charging feature according to IHS Markit report is shown in Fig. 1-2 [14]. As demonstrated in Fig. 1-2, wireless charging technology is gaining popularity in consumer electronics applications recently. This dissertation addresses the multiple aspects of the wireless charging technology in the low power applications.

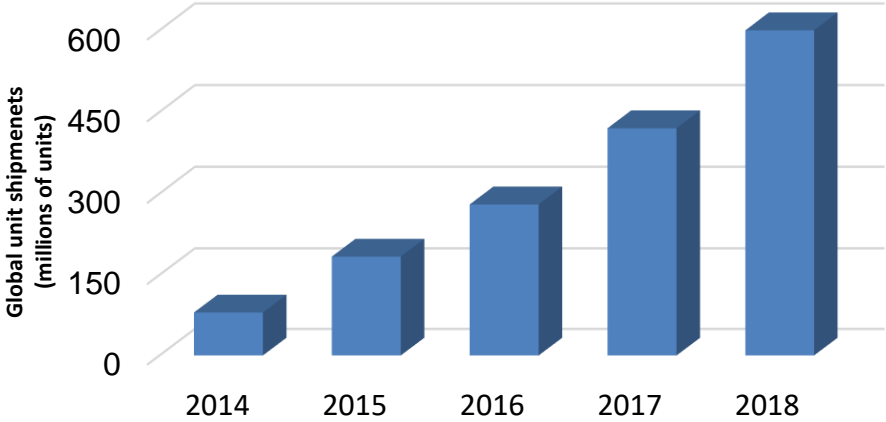


**Fig. 1-2. Global unit shipments of wireless charging devices from 2014 to 2018. (Source from IHS Markit).**

## 1.2 Overview of Wireless Power Transfer Technologies

Starting from Nicolas Tesla, wireless power transfer (WPT) technology has been studied intensely in the past century. According to the transmission distance, wireless power transfer technologies are divided into two categories: radiative and non-radiative power transfer.

Radiative power is emitted from an antenna and the transfer region is beyond the wavelength of electromagnetic wave [15]. According to the operation frequency, microwave beam and laser beam can be used to transfer energy through a long transmission distance. The microwave method has been pursued for more than 50 years. In 1960s, Brown successfully powered a helicopter by a ground station through microwave power [16]. Afterwards, several research efforts were made on utilizing microwave beam to transfer power from satellites to the earth since 1970s even though the feasibility is still questionable [17]. Similarly, laser beam wireless power transfer technology to transfer the energy from the solar farm in the outer space to the earth is also evaluated [18], [19]. The major challenges of the radiated power transfer are the low transmission efficiency and safety issues related to human exposure to electric and magnetic field [20]. Besides, the power transmission might be interrupted by any foreign objects in the space. Therefore, the radiated power transfer technology is suitable for uninhabited areas, for example, the outer space [21].

Non-radiative wireless power transfer is limited in the range of the wavelength of electromagnetic wave. In this near field region, there are two types power transfer methods: capacitive coupling and inductive coupling. The capacitive coupling systems transfer power by electric field between two metal plates and the system diagram is shown in Fig. 1-3. Capacitive power transfer technology is evaluated in both consumer electronics and electric vehicles application [22]-[24]. The power level of the system is related to the coupled capacitance value and the capacitance value is determined by the area of the plate, the permittivity of the medium

between plates and the gap between plates. Due to the low permittivity of the air, it is hard to raise the power rating of a capacitive coupling wireless power transfer system. In addition, at the same transfer power level the safety issue related to the magnetic field is not as serious as the electric field [20]. Therefore, near-field inductive coupling is promising in consumer electronics application where safety issue is valued [34]-[36].

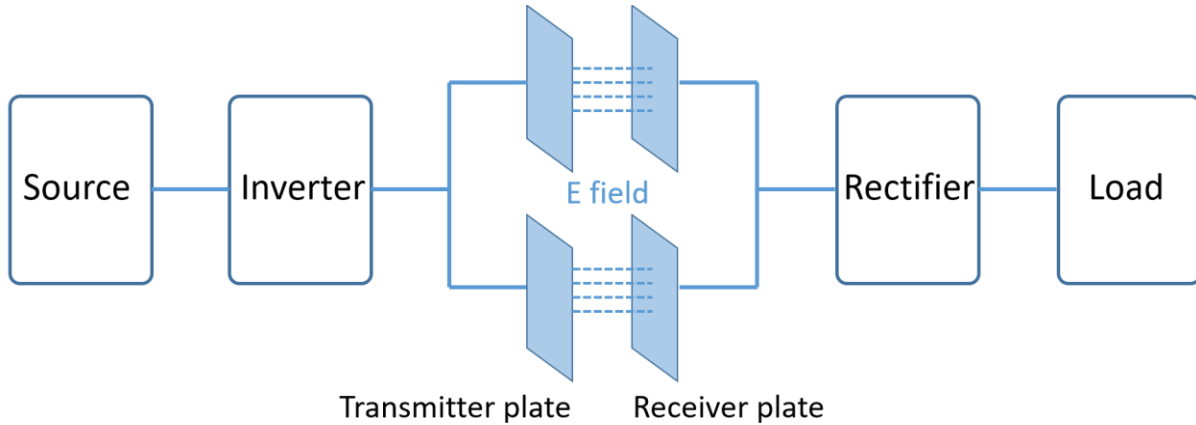


**Fig. 1-3. Capacitive coupling wireless power transfer system diagram.**

The near field inductive power transfer technology use the magnetic field to transfer energy. According to the Faraday’s law, the alternating magnetic flux enclosed by a coil induces a voltage in the coil loop. The transformer is a successful example of utilizing inductive coupling to transfer energy. With a gapped magnetic core, the wireless power transfer is achieved. The near field inductive power transfer is the most successful among all the wireless charging technologies due to its safety and flexibility to increase the power level in different situations. Starting from Nikola Telsa, the inductive power transfer was explored generation after generation. As mentioned in section 1.1, the inductive power transfer is applied in biomedical application since 1970s. And the research team in the Auckland university has made great contributions to apply this technology in electric vehicles application [25]-[28] since 1990s. Soon afterwards, the research team in the

University of Hong Kong has done lots of work to promote inductive power transfer for consumer electronics application and led the remarkable establishment of Wireless Power Consortium for the industry [11], [20].

### 1.3 Inductive Power Transfer Technology

Inductive power transfer utilizes the near field magnetic field to transfer energy from a transmitter coil to a receiver coil. In Fig. 1-4, the excitation current ( $i_p$ ) flowing through the transmitter coil induces magnetic field around it. And a receiver coil around it captures part of the magnetic field and voltage is induced in the receiver loop. The induced voltage can supply the load and energy is transferred wirelessly.

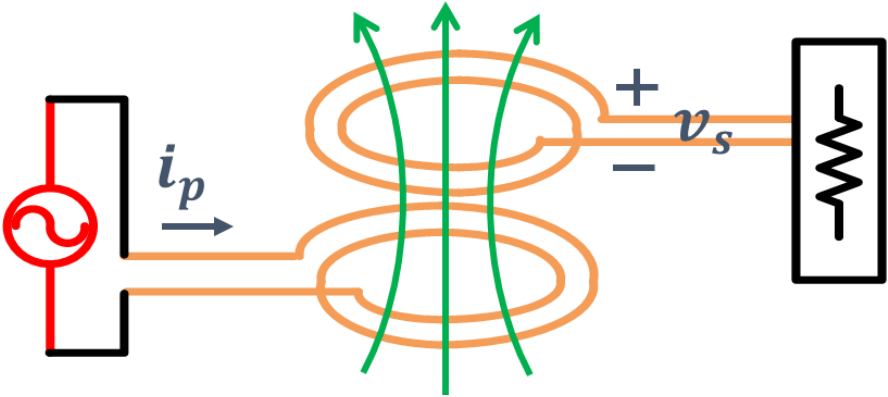


Fig. 1-4. Inductive power transfer concept with loosely coupled coils.

The equivalent circuit mode of the loosely coupled coils is shown in Fig. 1-5, where  $i_p$  and  $i_s$  are the excitation current of the transmitter and receiver coil separately;  $L_p$  and  $L_s$  are the self-inductance of the transmitter and receiver coil separately;  $R_p$  and  $R_s$  are the equivalent resistance of the transmitter and receiver coil separately;  $M$  is the mutual inductance between the coupled coils;  $\omega$  is the angular frequency of the operation frequency;  $R_L$  is the ac load resistance;  $V_s$  is the

output voltage across the load resistance. According to the decoupled circuit model in Fig. 1-5, the output voltage across the load resistance is derived as:

$$V_s = \frac{R_L}{R_L + R_s + j\omega L_s} j\omega M I_p \quad (1.1)$$

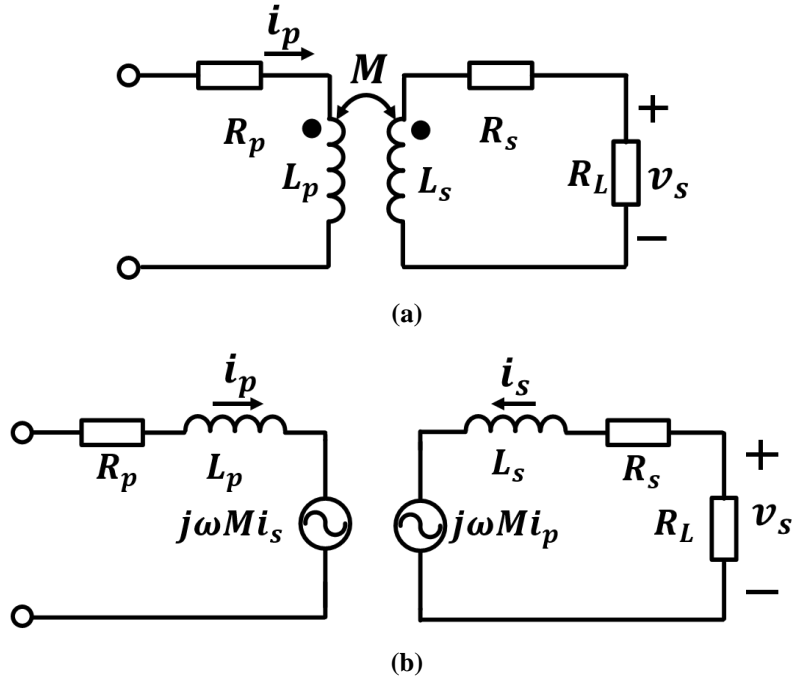


Fig. 1-5. The circuit model of loosely coupled coils. (a). Original circuit model. (b). Decoupled circuit model.

As illustrated by (1.1), the output voltage ( $V_s$ ) is divided by the impedance of the receiver coil and load resistance. To increase the power transfer capability, a compensation capacitor ( $C_s$ ) is normally added in series with the receiver coil as shown in Fig. 1-6 and the impedance of the receiver coil is cancelled by the compensation capacitor. With the resonance of the compensation capacitor and the receiver coil, the output voltage is increased as follows:

$$V_s = \frac{R_L}{R_L + R_s + j\omega L_s + \frac{1}{j\omega C_s}} j\omega M I_p = \frac{R_L}{R_L + R_s} j\omega M I_p \quad (1.2)$$

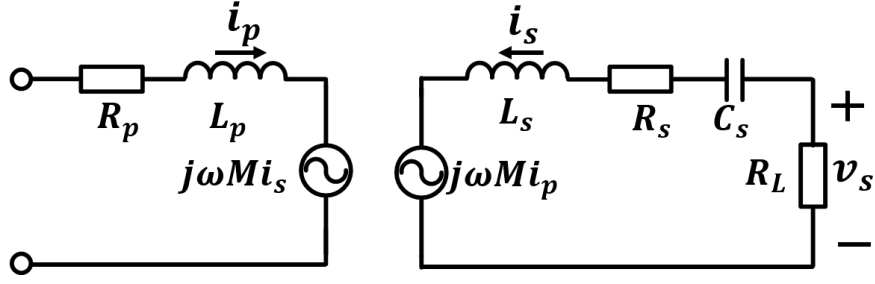


Fig. 1-6. The decoupled circuit model of the loosely coupled coils with compensation capacitor.

As shown in (1.2), the output voltage is mainly determined by the operation frequency, the mutual inductance and the excitation current of the transmitter coil. In addition, the coil to coil transfer efficiency is calculated as:

$$\eta_{coil} = \frac{I_s^2 R_L}{I_s^2 R_L + I_s^2 R_s + I_p^2 R_p} = \frac{R_L}{R_L + R_s + \frac{(R_L + R_s)^2}{\omega^2 M^2}} \quad (1.3)$$

where the mutual inductance between the transmitter coil and the receiver coil can be expressed as:

$$M = k\sqrt{L_p L_s} \quad (1.4)$$

Meanwhile, the coil resistance can be expressed by the coil quality factor ( $Q_p$ ,  $Q_s$ ) as:

$$R_p = \frac{\omega L_p}{Q_p}, \quad R_s = \frac{\omega L_s}{Q_s}. \quad (1.5)$$

With (1.4) and (1.5), (1.3) is organized as:

$$\eta_{coil} = \frac{R_L}{R_L + R_s + \frac{(R_L + R_s)^2}{k^2 Q_p Q_s R_s}} \quad (1.6)$$

To achieve the optimum coil to coil efficiency, (1.7) must be satisfied.

$$\frac{d\eta_{coil}}{dR_L} = 0 \quad (1.7)$$

Solving (1.7), the optimum load resistance to achieve the best coil to coil efficiency is:

$$R_{L\_opt} = R_s \sqrt{1 + k^2 Q_p Q_s} \quad (1.8)$$

And the coil to coil efficiency at the optimum load resistance is:

$$\eta_{coil\_max} = \frac{k^2 Q_p Q_s}{(1 + \sqrt{1 + k^2 Q_p Q_s})^2} \quad (1.9)$$

Therefore, the maximum coil to coil efficiency is determined by  $k^2 Q_p Q_s$ , which is defined as the figure-of-merit for inductive coupled coils [25]. In inductive power transfer system, it is essential to increase the coupling coefficient of the coupled coils and the quality factor of the coils.

Similarly as the compensation capacitor in the receiver side, the compensation network is also added in the transmitter side to improve the power transfer capability. To drive the resonant tank, an inverter is adopted in the system as illustrated in Fig. 1-7. The system is powered by a DC input source, which comes from an adapter or a USB port in consumer electronics application. The inverter stage changes DC power to AC power and drives the resonant tank. In the receiver side, a rectifier stage is adopted to transfer AC power to DC power and charge the battery load. The general system structure behaves like a conventional DC-DC resonant converter in power electronics field and the difference is that the traditional transformer is substituted by a loosely coupled coils. It is worth noting that the system structure in Fig. 1-7 is simplified case to illustrate the working principles. In real application scenario, a DC-DC converter can be added after the rectifier to regulate the output for charging a battery.

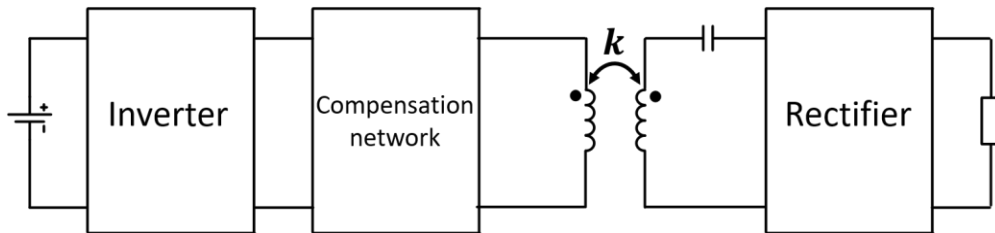


**Fig. 1-7. A general system structure of a loosely coupled coils system.**

Other than two coil system, a four coil wireless power transfer system are reported by the research team in MIT [29]. With two intermediate coils, the power transfer range is increased. A detailed circuit analysis of four coil system is conducted in [30] and it is found that the basic principle of four coil system is the same as two coil system. In addition, wireless domino-resonator systems with even more intermediate coils is proposed by the research group in the University of Hong Kong [31]-[33]. The intermediate coils can guide the near field magnetic field in certain direction and improve the power transfer range. However, it is not practical to add these relay coil resonator in consumer electronics application.

#### **1.4 High Frequency Operation vs. Low Frequency Operation**

Nowadays, there are two major wireless charging standards for consumer electronics applications, including the Qi standard (100-205 kHz) and the AirFuel Standard (6.78 MHz) [20]. The power transfer capability of the WPT system is related to the operation frequency according to (1.2). Higher operation frequency improves the induced voltage in the receiver coil. In addition, the coil link efficiency, as shown in (1.9), is related to the magnetic coupling condition between coupled coils and the coil quality factor ( $Q$ ), as defined in (1.10), where  $\omega$  is angular operation frequency;  $L$  is the self-inductance of the coil;  $R$  is the parasitic resistance of the coil. In low frequency system, the coil quality factor is lower; therefore, a strong coupling condition between the transmitter coil and the receiver coil is needed to maintain good system efficiency. In other words, good alignment between the charging pad and receiver device is required in Qi charging pad. Two charging scenario for a smart phone in Qi charging pad is shown in Fig. 1-8. The system cannot work when there is misalignment between the charging pad and the smart phone receiving

device. On the contrary, it is easy to achieve high coil quality factor for the AirFuel standard (6.78MHz). In this sense, the 6.78MHz system can achieve efficient power transfer even with a weaker coupling condition. Therefore, high frequency operation is desired to improve the charging spatial freedom.

$$Q = \frac{\omega L}{R} \quad (1.10)$$

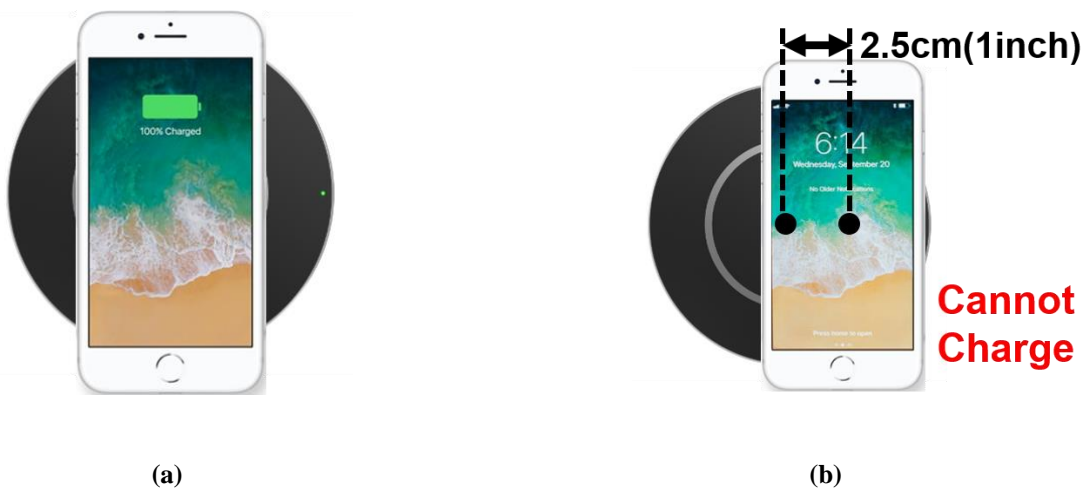


**Fig. 1-8. Two charging scenario for smart phone device of a commercial Qi charging pad. (a). There is no misalignment between transmitter and receiver. (b). There is misalignment between transmitter and receiver.**

The performance of the loosely coupled coils benefits from the high frequency operation. However, the 6.78 MHz operation leads to design challenge for the inverter and rectifier stage. With the traditional Si devices, the switching loss increases substantially in MHz range. Fortunately, the emerging semiconductor devices with wide band gap material exceed the limit of Si devices and are utilized to pursue groundbreaking high frequency, high efficiency power conversion. With the help of Gallium nitride (GaN) devices, the system switching frequency is selected as 6.78 MHz to achieve good spatial charging freedom in the dissertation

## 1.5 From Directional WPT system to Omnidirectional WPT system

The majority of the charging coils in inductive power transfer system are planar structure [25] [37]. The magnetic field induced by a planar charging coil is mainly in vertical direction as shown in Fig. 1-9(a) and energy flows in one direction. For small portable devices, such as Bluetooth earphones and wearable devices, the orientation is flexible. The receiver coil embedded in the device receives small amount of magnetic flux when the angle of the receiver plane and the magnetic field is very small. The angle misalignment between the transmitter coil and the receiver coil degrades the power transfer capability for the inductive power transfer system. As demonstrated in Fig. 1-9(b), the planar charging pad cannot provide the energy for a receiver device standing on the charging setup.



**Fig. 1-9. Two charging scenario for wearable device of a planar charging pad (a). Receiver device is in perpendicular with the magnetic field. (b). Receiver device is in parallel with the magnetic field.**

To deal with angle misalignment issue, the transmitter should has the capability to generate the magnetic field in different directions. In another words, the omnidirectional magnetic field is desired in the setup. Since 2010s, the omnidirectional wireless charging system becomes a hot research topic in academia due to its charging flexibility [38]-[47]. In the dissertation, a

comprehensive study of the omnidirectional WPT system is conducted.

## **1.6 Challenges in Omnidirectional WPT system**

### **1.6.1 Transmitter Coils Structure to Generate Omnidirectional Field Distribution**

Recently, omnidirectional wireless power transfer systems have been studied intensely due to their improved flexibility when compared with their planar counterparts. In [38], the multiple orthogonal transmitter coils structure was proposed to enable multi-angle wireless power transmission. In [39], [40], a bowl-shaped transmitter coils structure was proposed to provide multiple direction magnetic field distribution. All of these works were using a 3D transmitter coils structure and a one-dimensional receiver coil, which is denoted as a 3Tx-1Rx coils structure in this paper. The excitation current of each transmitter coil is identical. The total magnetic field vector is the vector sum of the field induced by each transmitter coil and is in one fixed direction. In such system, the angular misalignment between the transmitter coil and receiver coil degrades power transfer because the tilted planar receiver coil only captures a fraction of the vertical field induced by the transmitter coil. Hence, there is no true omnidirectional magnetic field and it is still possible that a small receiver coil receives a small amount of energy when it is in parallel with the field vector.

To cope with this problem, a 3D receiver coils structure was proposed in [41], [43]. In this way, different receiver coils can pick up different direction magnetic field and receive enough flux with arbitrary magnetic field direction. However, the 3D receiver coil structure occupies too much space and is not desired in consumer electronics applications. Another method to solve this issue is to excite transmitter coils with non-identical current [44]-[47]. In a multiple transmitter coils

WPT system, the magnetic field at one point is the vector sum of field induced by each transmitter coil, according to the superposition theorem. The magnetic field induced by each coil is used as the basis vector. With a different ratio between different basis vectors, the total magnet field vector is in a different direction and rotates in a 3D manner. Therefore, true omnidirectional WPT capability is achieved by a 3D coils structure with modulation excitation current. The summary of the omnidirectional WPT system in existing literature is provide in Table 1.1.

In [44], [45], a three orthogonal transmitter coils structure is adopted, and the limitation is that omnidirectional WPT capability is only achieved near the center region of the transmitter. Free-positioning characteristic is not achieved, which is particularly important for charging mobile devices. In [46], [47], a cross-dipole receiver coil with a ferrite core is adopted, but the drawback is that it occupies more space than a single planar coil. In consumer electronics applications, a novel transmitter coils structure is needed to provide free-positioning omnidirectional WPT capability for a planar receiver coil.

TABLE 1.1 SUMMARY OF OMNIDIRECTIONAL IPT SYSTEM IN EXISTING LITERATURE

Coils structure	Without modulated excitation current	With modulated excitation current
3Tx-1Rx	[38][39][40]	[44][45]
3Tx-3Rx	[41]	N/A
1Tx-3Rx	[43]	N/A
2Tx-2Rx	[42]	[46][47]

### 1.6.2 Effective Power Transfer under Weak and Variable Coupling Condition

Compensation networks are normally used to improve the power transfer capability of a WPT system with loosely coupled coils. The resonant circuits, formed by the loosely coupled coils and external compensation inductors or capacitors, are crucial in the converter design.

One crucial challenge of the compensation network design in an omnidirectional IPT system

is weak and variable coupling coefficient ( $k$ ) between the transmitter coil and receiver coil. To improve the power transfer capability at weak coupling condition, high frequency operation is adopted. In this dissertation, a fixed operating frequency at 6.78 MHz is selected to follow AirFuel charging standard in consumer electronics application. The characteristics of a compensation network is related to the operation frequency and the system normally operates at the resonant frequency of the network to maximize power transfer capability. If the resonant frequency is dependent on  $k$ , variable frequency control against  $k$  variations might be adopted to track the resonant frequency [49], [50], which increases the system control complexity and decreases the reliability. However, the operating frequency is fixed at 6.78MHz according to the charging standard. Regarding this, the resonant frequency of the compensation network had better to be independent of coupling coefficient. Therefore, the resonant converter topology study is conducted to find a resonate converter which has a load independent resonant frequency.

Other than the crucial challenge, the second challenge of the compensation network design in an omnidirectional IPT system is voltage controllability under load change [51]. The lithium-ion battery in receiver device is equivalent to different resistors at different charging stage in its charging profile. A load-independent output voltage characteristics is preferred to reduce the regulation complexity.

The third challenge of the compensation network design in an omnidirectional IPT system is how to decouple multiple transmitter coils from a control point of view. In an omnidirectional IPT system, the excitation current of each transmitter coil is controlled to induce magnetic field in different direction [45]. The cross coupling between different transmitter coils makes the control of the excitation current much more complicated. Considering this, a current source characteristics of the transmitter coil is desired to simplify system control in omnidirectional IPT system.

The fourth challenge of the compensation network design in an omnidirectional IPT is maximum efficiency operation due to the loosely coupling between the transmitter coil and receiver coil. As studied in [52], the transfer efficiency in omnidirectional IPT system is not only related to the compensation network, but also the control method of the transmitter coil current. But these two factors are independent of each other so that current control method is not considered in the compensation design. The coil link efficiency is only related to the compensation network in the receiver side and it should be able to minimize the reactance in the receiver loop and maximize the current transfer [53].

The fifth challenge of the compensation network design is zero voltage switching (ZVS) of the switching device. Megahertz (MHz) wireless charging system is used to improve charging spatial freedom in low power application. ZVS of the switching devices is essential to reduce the switching loss and the switching related electromagnetic interference (EMI) issue in a MHz system. To achieve ZVS, the inductive input impedance of the system is required [54].

These five requirements for the compensation network design in omnidirectional IPT system is summarized as follows: (1). coupling independent resonant frequency; (2). load independent output voltage; (3). load independent transmitter coil current; (4). maximum power transfer efficiency; (5). inductive input impedance required by ZVS operation. Four basic types of compensation networks depending on how the external capacitors are connected to the transmitter and receiver coil, namely, series-series, series-parallel, parallel-series, and parallel-parallel topologies have been studied comprehensively in [54]. None of these four compensation topologies can satisfy all the requirements. Therefore, high order resonant circuits with more compensation component is needed.

### 1.6.3 Stray Field Reduction for Human Health

An importance concern of a WPT system with the inductive power transfer technology is the safety issue related to stray field. The stray field distribution with the loosely coupled coils is shown in Fig. 1-10 [48]. The stray field around the charging setup might cause adverse biological effects to the human body exposed to it [85]. To avoid such safety issue, the stray field level must comply with certain guideline or standards given by the government or regulation organizations [85]-[87].

In a Qi charging system for consumer electronics application, the human exposure problems can be mitigated by a magnetic shield [20]. However, the effectiveness of a magnetic shield is not evaluated in a 6.78MHz system in the existing literature. Due to the available material technology, the permeability of the magnetic material at 6.78MHz is much lower than low frequency case. It is found that the stray field cannot comply with the human exposure regulations due to low permeability of the magnetic material. Therefore, an effective shielding method is desired for a 6.78 MHz WPT system.

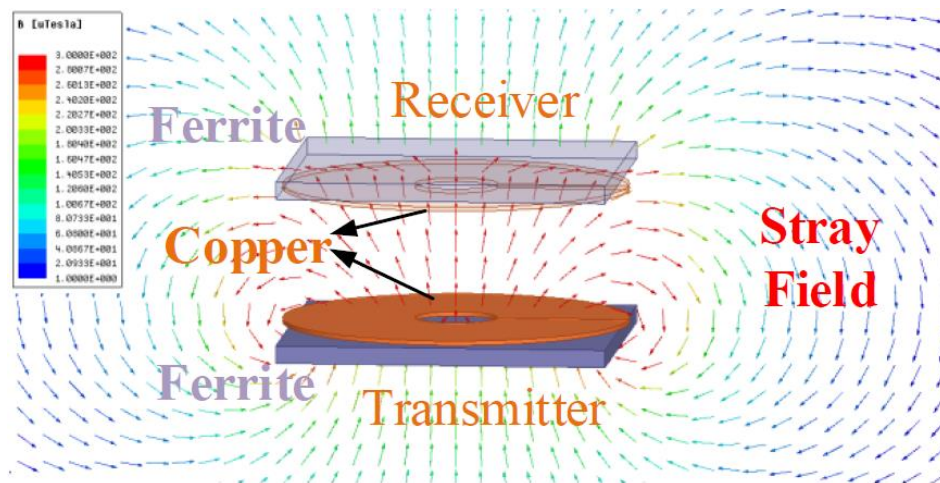
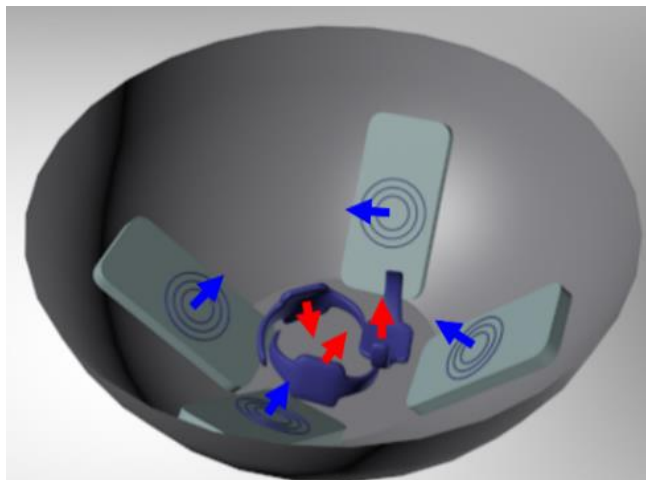


Fig. 1-10. The field distribution with loosely coupled coils [48].

#### **1.6.4 Intelligent Charging Strategy**

In an omnidirectional WPT system, there are multiple receiving devices to fully utilize the power transfer potential. An omnidirectional WPT system with multiple receiver devices is shown in Fig. 1-11. The power transfer performance to a certain receiver device is related to its orientation and the power transfer capability is maximized when the magnetic field is perpendicular to the receiver plane. Therefore, a smart detection method to identify the orientation of the receiver devices is desired. The simply way to predict the load information is utilizing the input power information; however, the load information of different receiver devices is mixed up in the total input power information. A control algorithm to decouple the load information for different receiver devices is needed.

After the identifying the orientation of the receiver devices, the charging setup should has the capability to point the magnetic field towards the optimum direction desired by different receiver coils. As illustrated in Fig. 1-11, the optimum field direction for different receiver devices is not necessarily the same. Therefore, it is difficult to charge all the receiver devices with the optimal field direction simultaneously. Regarding this, a power allocation strategy to charge multiple devices quickly and efficiently is desired.



**Fig. 1-11. An omnidirectional wireless charging setup with multiple receiver devices.**

## **1.7 Proposed Dissertation Outline**

Chapter 1 introduces the historical background of wireless power transfer technology. Different available WPT technologies are reviewed and inductive power transfer is promising in consumer electronics application. Basic theory behind the inductive power system is introduced and the issue with planar charging system is demonstrated. To improve the charging flexibility, omnidirectional WPT system has bright future and therefore, the state-of-the-art solutions in consumer electronics application are reviewed and the challenges in this research area are identified. The research objectives of this work is to solve all the challenges and promote omnidirectional WPT technology for consumer electronics application.

Chapter 2 proposes a novel transmitter coils structure to generate omnidirectional magnetic field distribution. With the proposed coils structure, the charging platform can deliver energy in any direction to the receiving device. Therefore, the alignment between the transmitter coil and the receiver coil is no longer needed.

Chapter 3 clarifies the requirements of the compensation network in omnidirectional WPT system. A systematic way to find proper compensation network satisfying the requirement is derived. The LCCL-LC resonant converter is selected due to its low harmonics and low extra compensation components.

Chapter 4 illustrates a design methodology of the LCCL-LC converter at 6.78MHz. The soft-switching of primary devices is realized to reduce switching loss and switching related loss. Hardware is fabricated and tested and the performance is analyzed.

Chapter 5 evaluates the stray field reduction effect of a magnetic shielding layer in our charging setup. It is found that a single layer shielding is not effective enough due to the low permeability of available high frequency magnetic material. Therefore, an extra conductive layer is added to further confine the magnetic field. Simulation and experiment result validates the effectiveness of the double layer shielding structure.

Chapter 6 develops a smart detection method to predict the receiving device's orientation and focus the field direction on the optimal direction. Meanwhile, a strategy to deal with power allocation among multiple receiving devices is illustrated.

Chapter 7 concludes the dissertation and gives the research topics that would be worked on in the future.

# Chapter 2 Transmitter Coils Structure for Omnidirectional WPT System

## 2.1 Introduction

The reported omnidirectional WPT systems in the literature can be classified into two categories: 1). the omnidirectional WPT system with identical excitation current flowing through different transmitter coils [38]-[42]; 2). the omnidirectional WPT system with non-identical excitation current flowing through different transmitter coils [44]-[47]. In [38]-[42], 3D transmitter coils structure is adopted to generate different directions field in different areas due to field curvature. If the receiver coil is large enough, the enclosed area by the coil contains different directions magnetic field and the energy transfer degradation issue under angle misalignment is mitigated. However, the magnetic field at one point is still in one fixed direction, which is determined by the vector summation of the field vector induced by each transmitter coil. Even though there is different directions magnetic field in different areas in the first category system, the magnetic field at one point is still limited to one direction. In another words, the omnidirectional field is only achieved in space perspective, not in time perspective. To rotate the magnetic field at one point, the excitation current of each transmitter coil is controlled and therefore the basis field vector of each coil is controlled. With a different ratio of each field vector, the total magnetic field can be directed to different directions and true omnidirectional power transfer capability is achieved in the second category systems [44]-[47].

One example of an omnidirectional WPT platform with modulated transmitter coils excitation current, is introduced with detail in this section [44], [45]. The transmitter coils structure is shown in Fig. 2-1, and coils 1-3 are orthogonal with each other. The corresponding excitation current of

the three coils ( $i_1, i_2, i_3$ ) is shown in (2.1)-(2.3), where:  $\omega_0 = 2\pi \cdot 6.78\text{MHz}$ : frequency of the ac current;  $\omega_1 = 2\pi \cdot 450\text{Hz}$ : modulation frequency of the current amplitude;  $I_m$ : amplitude of the current;

$$i_1(t) = I_m \sin(\omega_0 t) \quad (2.1)$$

$$i_2(t) = I_m \sin(\omega_1 t) \cos(\omega_0 t) \quad (2.2)$$

$$i_3(t) = I_m \cos(\omega_1 t) \cos(\omega_0 t) \quad (2.3)$$

The magnetic field at center O induced by each coil ( $\mathbf{B}_1, \mathbf{B}_2, \mathbf{B}_3$ ) is then calculated with Biot-Savart law as (2.4)-(2.6) [55],

$$\mathbf{B}_1 = \frac{\mu_0}{2R} I_m \sin \omega_0 t \hat{\mathbf{x}} \quad (2.4)$$

$$\mathbf{B}_2 = \frac{\mu_0}{2R} I_m \sin(\omega_1 t) \cos(\omega_0 t) \hat{\mathbf{y}} \quad (2.5)$$

$$\mathbf{B}_3 = \frac{\mu_0}{2R} I_m \cos(\omega_1 t) \cos(\omega_0 t) \hat{\mathbf{z}} \quad (2.6)$$

where  $\mu_0$ : vacuum permeability;  $\hat{\mathbf{x}}, \hat{\mathbf{y}}, \hat{\mathbf{z}}$ : standard basis vector;  $R$ : radius of the transmitter coil.

The total magnetic field  $\mathbf{B}_t$  at center O is the vector summation of  $\mathbf{B}_1, \mathbf{B}_2, \mathbf{B}_3$ , which is a time varying vector. At a different time instant, the total magnetic field  $\mathbf{B}_t$  is at a different direction. Therefore, a single planer receiver coil can receive enough flux, even with angle misalignment between transmitter coils.

The magnitude of  $\mathbf{B}_t$  is calculated in (2.7), which is a constant value. If the end point of  $\mathbf{B}_t$  is plotted, the magnetic field trajectory at center O is on the surface of a sphere, as shown in Fig. 2-1 (b). The total magnetic field rotates in a different direction, and an omnidirectional magnetic field is obtained.

$$|\mathbf{B}_t|^2 = |\mathbf{B}_1|^2 + |\mathbf{B}_2|^2 + |\mathbf{B}_3|^2 = \frac{\mu_0^2 I_m^2}{4R^2} \quad (2.7)$$

The magnetic field trajectory at point A (defined in Fig. 2-1(a)), which is near the surface of the sphere, is plotted, as shown in Fig. 2-1(c). At point A, the magnetic field induced by coil 1 and coil 2 is much smaller than the magnetic field induced by coil 3, which means the field is mainly in a z direction. Consequently, there is no omnidirectional magnetic field at point A. Similarly, an omnidirectional magnetic field is also not induced at the bottom of the sphere fixture. In this platform, the omnidirectional magnetic field distribution is only obtained near the center area. However, it is not realistic to hang the receiver device in the center of the sphere fixture in practical applications. Therefore, free-positioning characteristic of the receiver coil is not achieved with the coils structure. A new coil structure with free positioning omnidirectional power transfer capability is desired.

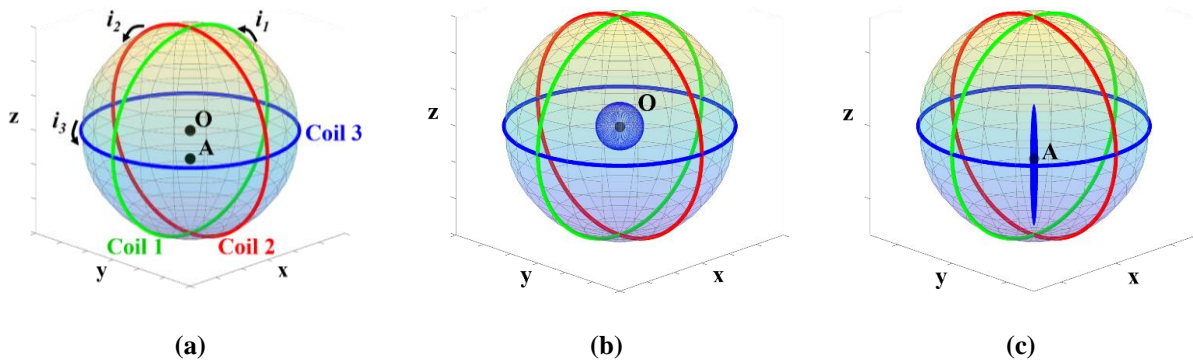


**Fig. 2-1. Transmitter coils structure reported in [13]. (a). Transmitter coils structure. (b). The magnetic field trajectory at point O. (c). The magnetic field trajectory at point A.**

## 2.2 Proposed Wireless Charging Bowl

### 2.2.1 Magnetic Field Preference in a Charging Bowl

In a charging bowl, the field preference for different devices, such as smart phones and wearable devices, are shown in Fig. 2-2. In most situations, a planar device is likely to lay on the

side face of the bowl. However, due to gravity, it is difficult for small portable electronic devices, such as hearing aids and wearable electronics devices, to stay on the side face of the bowl. They often fall into the bottom of the charging bowl. Therefore, perpendicular magnetic field to the surface is preferred to charge a planar device efficiently on the side face of the bowl. On the other hand, the orientation of a small portable device is very flexible and can be placed in any direction. Accordingly, omnidirectional magnetic field distribution is necessary at the bottom of the charging bowl.

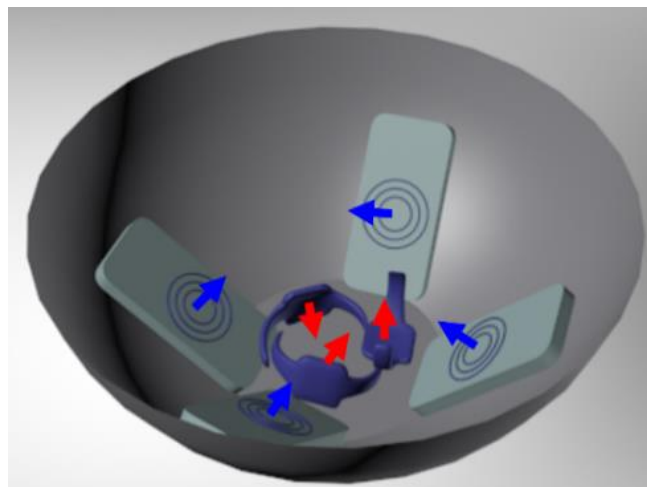


**Fig. 2-2. Magnetic field preference for different devices in charging bowl.**

### **2.2.2 Proposed Transmitter Coils Structure**

Based on the field preference in the wireless charging bowl, a novel transmitter coils structure is proposed, as shown in Fig. 2-3. There are five coils: coils 1-4 are wound from the bottom to the side face of the bowl; coil 5 is placed around the bottom of the bowl.

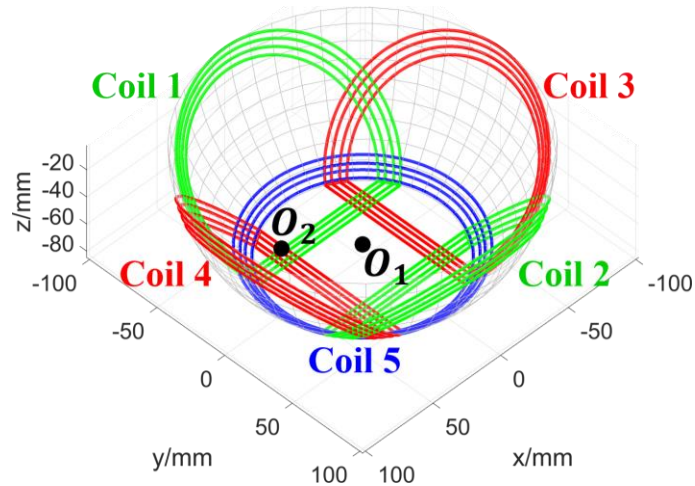


**Fig. 2-3. Proposed transmitter coils structure for the wireless charging bowl.**

The magnetic field distribution on the side face induced by coil 1, is simulated by finite analysis element software (ANSYS MAXWELL) and is demonstrated in Fig. 2-4(a). With this perpendicular field distribution, a planar device such as a smart phone, can be charged efficiently when placed on the side face. As illustrated in Fig. 2-4(a), field distribution is reasonably uniform and therefore free positioning characteristic for a smart phone receiver is guaranteed when placed on the side face.

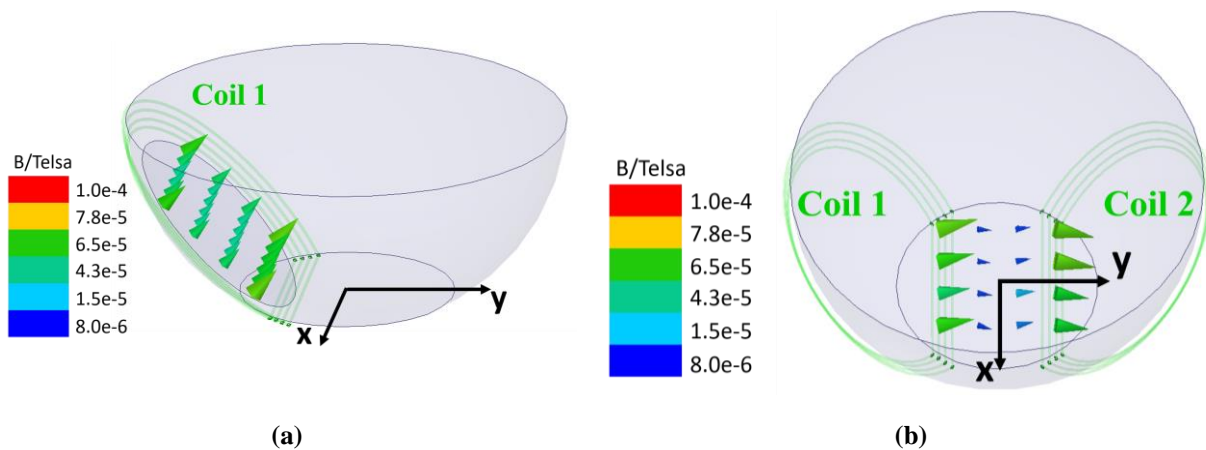


**Fig. 2-4. Magnetic field distribution of the side coil. (a) On the side face. (b) At the base.**

In addition, the magnetic field induced by coil 1 and coil 2 at the base of bowl, is mainly in y

direction, as shown in Fig. 2-4(b). In symmetry, the magnetic field induced by coil 3 and coil 4 is mainly in x direction at the bottom of the bowl. The magnetic field induced by coil 5 is mainly in z direction. With x, y, and z direction magnetic field at the base, the magnetic field can rotate in different directions with modulated excitation current  $i_1(t)$ ,  $i_2(t)$ ,  $i_3(t)$ , defined in (2.1)-(2.3) in Section 2.1. Here, coil 1 and coil 2 carry the same excitation current  $i_1(t)$ ; coil 3 and coil 4 carry the same excitation current  $i_2(t)$ ; coil 5 carries excitation current  $i_3(t)$ . The magnetic field distribution at the base of the bowl, at a different time instant, is shown in Fig. 2-5. With the proposed coil structure, a 3D rotating magnetic field can be achieved at the bottom of the charging bowl. If the end point of the field vector is plotted, the 3D field trajectory is obtained. Here the field trajectory at two example points  $O_1(-5, 5, -82\text{mm})$ , and  $O_2(30,-30,-78\text{mm})$  is shown in Fig. 2-6. Basically, the field trajectory is on the surface of an ellipsoid. As demonstrated in Fig. 2-5 and Fig. 2-6, the magnetic field distribution is not uniform. Therefore, transmitter coils geometry optimization is desired to achieve uniform omnidirectional field distribution.

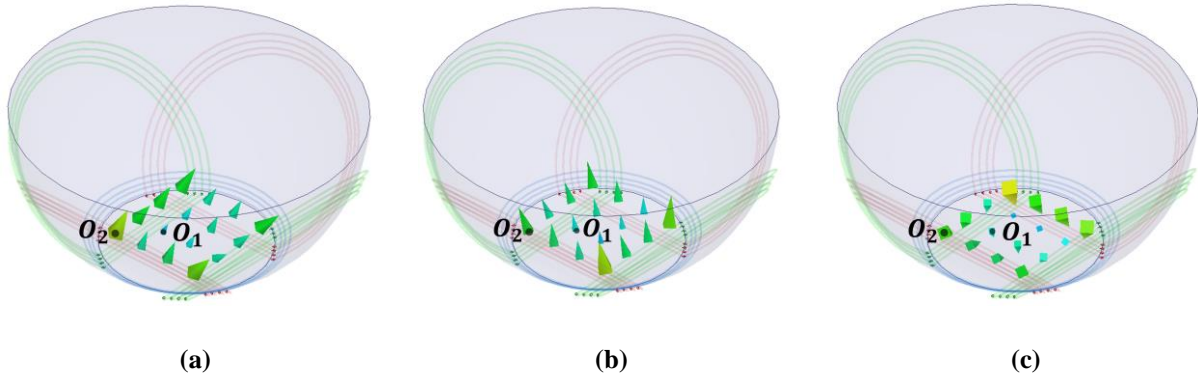


**Fig. 2-5. Magnetic field distribution at the base of the proposed charging bowl at different time instant. (a)  $\omega_1 t = \pi/10, \omega_0 t = \pi/4$ . (b)  $\omega_1 t = \pi/8, \omega_0 t = 7\pi/4$ . (c)  $\omega_1 t = 5\pi/4, \omega_0 t = 15\pi/8$ .**

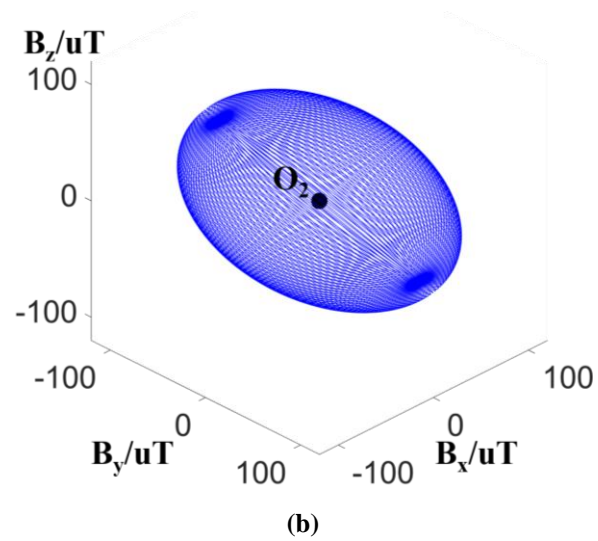
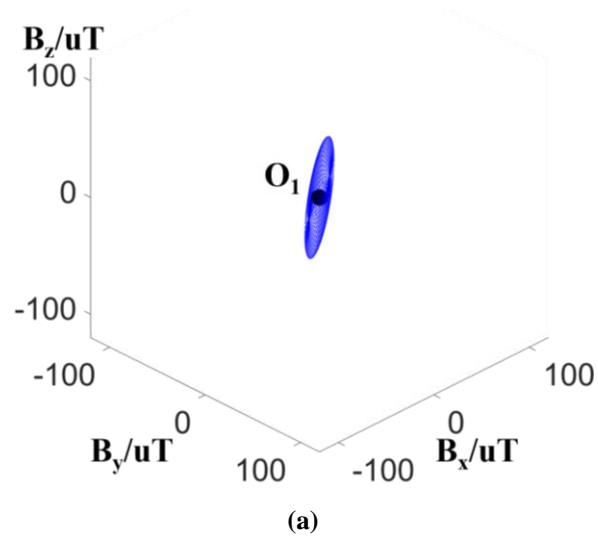


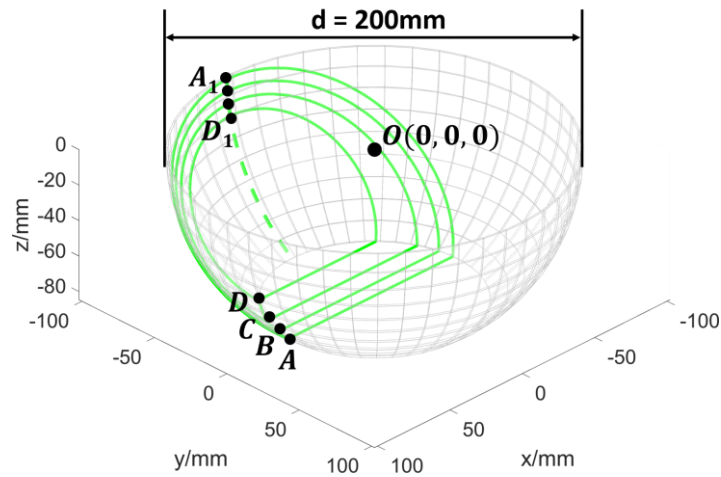
Fig. 2-6. Magnetic field trajectory at two example points. (a) At  $O_1$ . (b) At  $O_2$ .

### 2.3 Transmitter Coils Optimization

The simple way to achieve uniform omnidirectional field distribution at the base of the bowl is to make the field distribution of each set of coils is uniform. Simply put, the y-direction magnetic field induced by coil 1 and coil 2 and so on.

Coil optimization to get uniform field distribution is addressed in this section. Due to symmetry between coils 1 - 4, coil 1 optimization is used as an example to illustrate the

optimization methodology. In Fig. 2-7, the dimension of the charging bowl and design variables of coil 1 are illustrated. The turns number of the side coil is selected as four to achieve good trade-off between good coil efficiency and fabrication cost. The turns number selection study is reported in [56]. The charging bowl fixture is a half sphere cut with a horizontal plane at the bottom. The diameter of the sphere is set as 200 mm, and the height of the bowl fixture is 85 mm to accommodate several smart phones (typical dimension 60×120 mm) and small portable devices (typical dimension 42 × 36 mm). A Cartesian coordinate system is built to describe the position of coil 1. The origin of the coordinate system is at the center of the sphere. Coil 1 is embedded in the surface of the bowl fixture and is symmetrical about the y axis. The position of coil 1 can be determined by eight points (A-D, A<sub>1</sub>-D<sub>1</sub>). Points (A - D) are on the edge of the base plane of the bowl fixture and are described by four variables  $y_1, y_2, y_3, y_4$ , which is the y coordinate of these points. Points (A<sub>1</sub> - D<sub>1</sub>) are on the intersection line between the YZ plane and the side face of the bowl. With the coordinates of these eight points, side coil 1 can be determined.



(a)

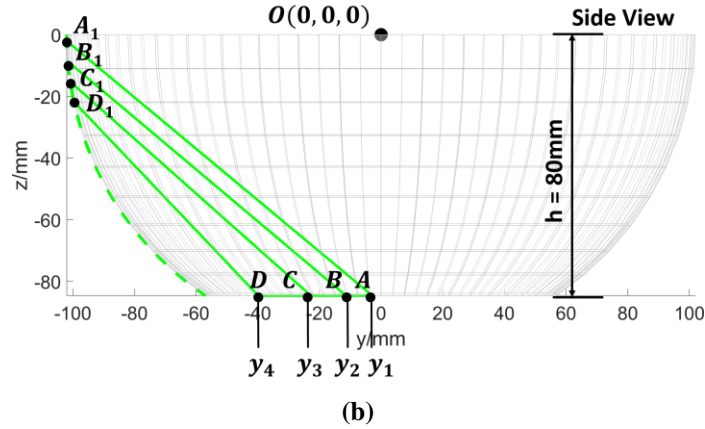


Fig. 2-7. Geometry of the charging bowl fixture and side coil 1. (a) 3D view. (b) Side view.

The objective of the coil 1 design is to induce strong and uniform magnetic field distribution at the base of the bowl. The target zone for the coil optimization is shown as the shaded area in Fig. 2-8. The height of the target zone is 35 mm to accommodate typical small portable devices in the market. In the target zone,  $N$  points with quasi-random sampling are considered for field calculation. Normally, the finite element analysis software is utilized to get magnetic field distribution, but it is time-consuming and not suitable for optimization. Therefore, an analytical model to calculate magnetic field distribution based on the Biot-Savart law as (2.8) [55], is built in this paper. The magnetic field vector at  $N$  sample points is calculated by the numerical integral of the Biot-Savart law. Then, the  $y$  component of the field vector at each sampling point is obtained as (2.9). The average ( $\mathbf{B}_{avg}$ ) and the standard variation ( $\mathbf{B}_{std}$ ) of ( $\mathbf{B}_{y1} \dots \mathbf{B}_{yN}$ ) is calculated in (2.10).

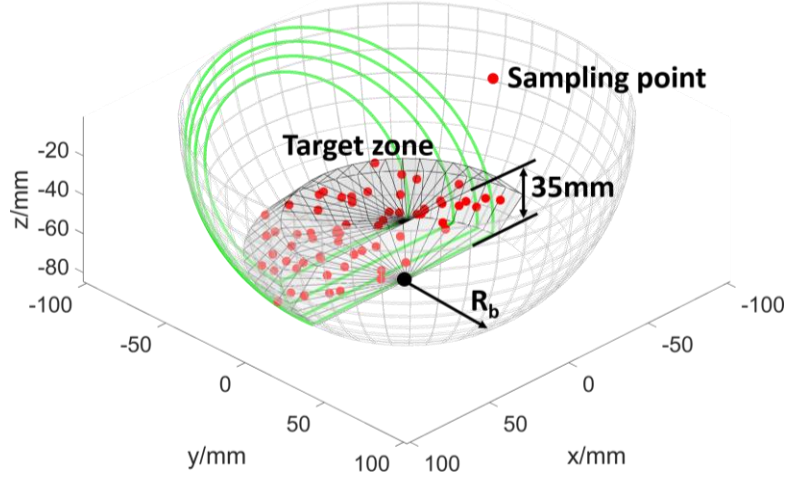


Fig. 2-8. Target zone of the charging bowl for the side coil 1 optimization.

To achieve strong and uniform  $y$  direction field distribution, the average ( $\mathbf{B}_{avg}$ ) of ( $\mathbf{B}_{y1} \dots \mathbf{B}_{yN}$ ) should be high and the standard variation ( $\mathbf{B}_{std}$ ) of ( $\mathbf{B}_{y1} \dots \mathbf{B}_{yN}$ ), as, should be small.

$$\mathbf{B} = \frac{\mu_0}{4\pi} \oint \frac{I d\mathbf{s} \times \mathbf{r}}{r^3} \quad (2.8)$$

$$\mathbf{B}_y = \mathbf{B} \cdot (0, 1, 0) \quad (2.9)$$

$$B_{avg} = \frac{1}{N} \sum_{i=1}^N |\mathbf{B}_{yi}|, B_{std} = \sqrt{\frac{1}{N-1} \sum_{i=1}^N (|\mathbf{B}_{yi}| - B_{avg})^2} \quad (2.10)$$

In the optimization problem, the position of  $A_1, B_1, C_1, D_1$  is not critical to field distribution at the target zone since these four points are far away from the target zone. Therefore, only the positions of  $A, B, C, D$  are optimized to achieve a strong and uniform  $y$  direction magnetic field in the target zone. As previously mentioned, the positions of points ( $A, B, C, D$ ) are described by their  $y$  coordinates ( $y_1, y_2, y_3, y_4$ ). The design optimization problem is formulated as (12-13):

$$\text{Design objective: Maximize } B_{avg} = f_1(y_1, y_2, y_3, y_4) \text{ and} \quad (2.11)$$

$$\text{minimize } B_{std} = f_2(y_1, y_2, y_3, y_4)$$

$$\begin{aligned} \text{Design constraints: } & -R_b < y_1, y_2, y_3, y_4 < R_b \\ (\text{R}_b: \text{radius of the base plane, defined in Fig. 2-8}) \end{aligned} \quad (2.12)$$

Given the nature of this optimization problem, a genetic algorithm is applied to locate the global or near-to-global optimal solution with reasonable computation cost [57]. The parameter optimization is implemented in MATLAB with a genetic algorithm function. At first, the coil geometry with different sets of  $(y_1, y_2, y_3, y_4)$ , within the design constraints is generated as candidates. Then, the magnetic field at 100 sampling points is calculated by the numerical model. Thereafter, the standard deviation and average value of  $\mathbf{B}_y$  at 100 sampling points is calculated, and the Pareto front of  $B_{\text{std}}$  and  $B_{\text{avg}}$  is plotted by the genetic algorithm [58]. Finally, an appropriate design parameter set  $(y_1, y_2, y_3, y_4)$  is selected, based on the tradeoff of  $B_{\text{avg}}$  and  $B_{\text{std}}$ .

In the design, the coordinates of A<sub>1</sub>-D<sub>1</sub> are set as A<sub>1</sub>(0, -99.9, -2 mm); B<sub>1</sub>(0, -99.7, -7 mm); C<sub>1</sub>(0, -99.3, -12 mm); D<sub>1</sub>(0, -98.5, -17 mm). These data is based on the coil optimization result reported in [56]. The  $B_{\text{avg}} - B_{\text{std}}$  Pareto front obtained by the genetic algorithm is demonstrated in Fig. 2-9. In Fig. 2-9, the turning point of the Pareto front is selected to achieve good tradeoff between field strength and uniformity. At the right side of the selected point, the side coil is more concentrated on the base plane, and field uniformity is scarified. At the left side, field strength is scarified by more distributed coil at the base. The selected design parameter set  $(y_1, y_2, y_3, y_4 = -4.5, -15.5, -27.4, -44.3 \text{ mm})$  can achieve a strong field distribution with good uniformity. The coils spacing between different turns of the selected design increases gradually. In this way, the field distribution is uniform.

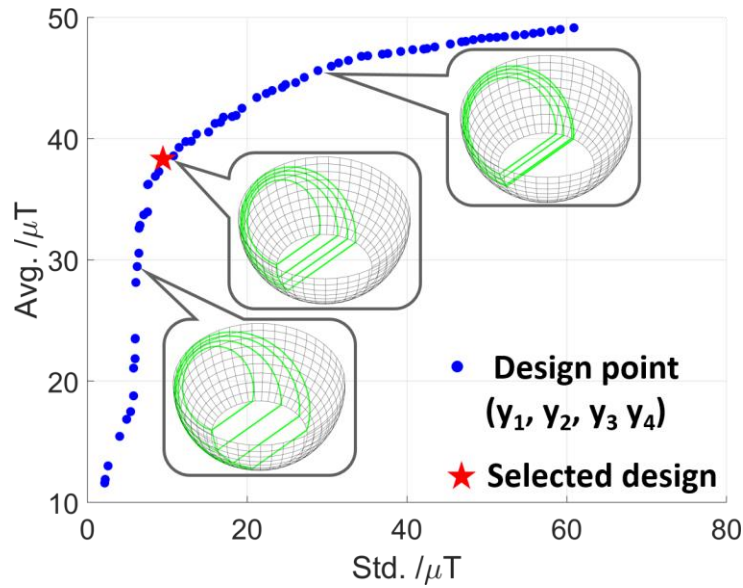


**Fig. 2-9.  $B_{avg}$  -  $B_{std}$  Pareto Frontier result for the side coil 1 optimization.**

The magnetic field distribution at the base plane ( $z=-85$  mm) with the optimized coil 1 and coil 2 is shown in Fig. 2-10. When comparing with a non-optimized case in Fig. 2-4(b), the magnetic field is more uniform. The magnitude of  $B_y$  distribution at the base plane, before and after the optimization, is provided in Fig. 2-11. The field distribution is much more uniform with the proposed coil design methodology.

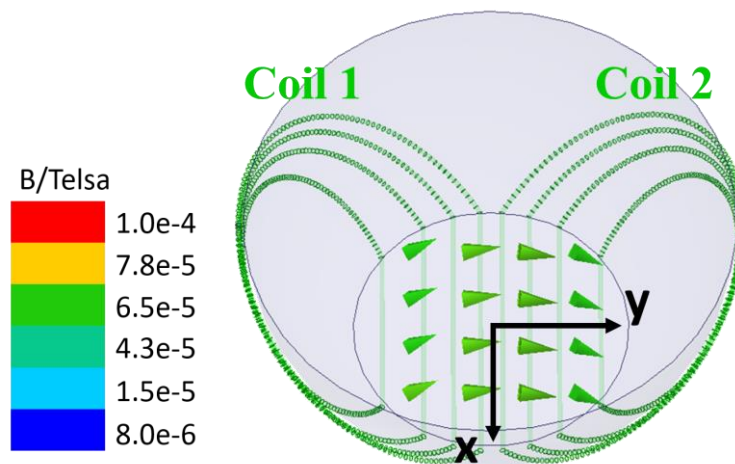


**Fig. 2-10. Field distribution at the base plane after the optimization.**

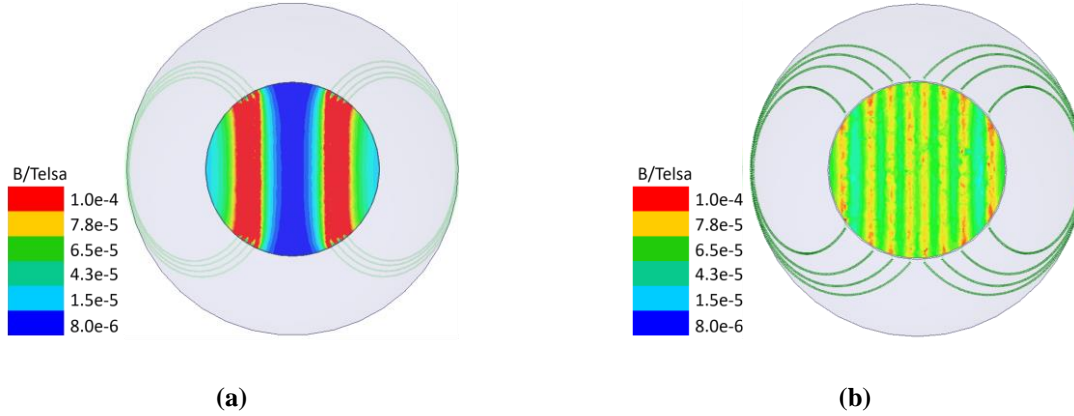


**Fig. 2-11.  $|B_y|$  distribution at the base plane. (a) Before the coil optimization. (b) After the coil optimization.**

After addressing side coil design, the bottom coil 5 (defined in Fig. 2-3) design is evaluated. The design methodology is almost the same: select proper geometry parameter of the transmitter coil to achieve strong and uniform field distribution at the base area. Different from the side coil, coil radius ( $R_1, R_2, R_3, R_4$ ) is adopted to describe the bottom coil geometry as illustrated in Fig. 2-12. Similarly to side coil design, genetic algorithm is applied to obtain the  $\mu$ - $\sigma$  Pareto front and the result is shown in Fig. 2-13. Then the turning point in the Pareto front is chosen to achieve tradeoff between field uniformity and strength. The final optimized coil geometry is shown in Fig. 2-14 and the magnetic field distribution at the base with the bottom coil excited is shown in Fig. 2-15. As illustrated in Fig. 2-15, uniform z direction magnetic field distribution is achieved.

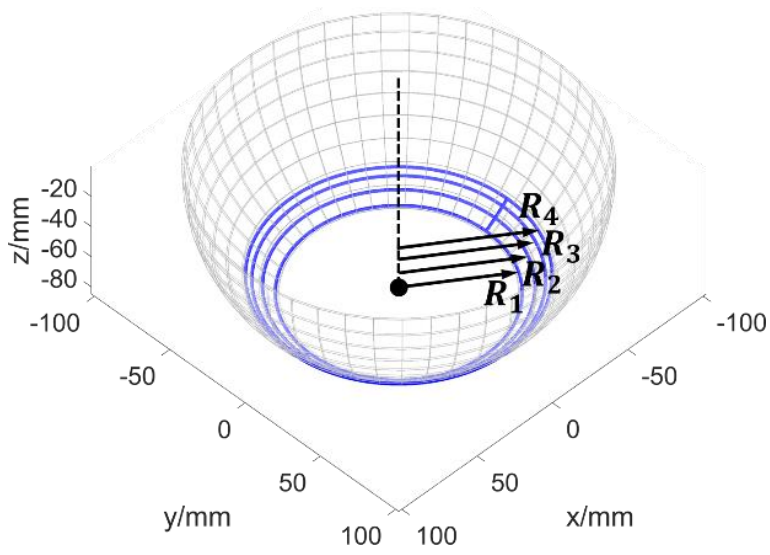


Fig. 2-12. Geometry of the bottom coil 5 in the charging bowl.

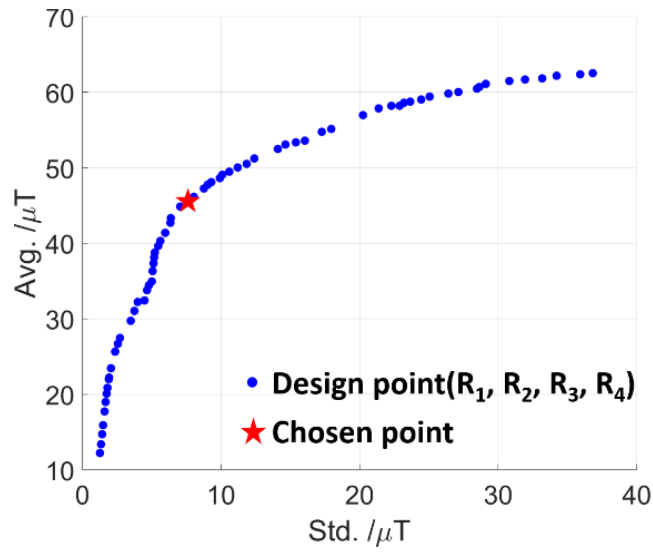


Fig. 2-13.  $\mu$ -  $\sigma$  Pareto Frontier of the bottom coil optimization

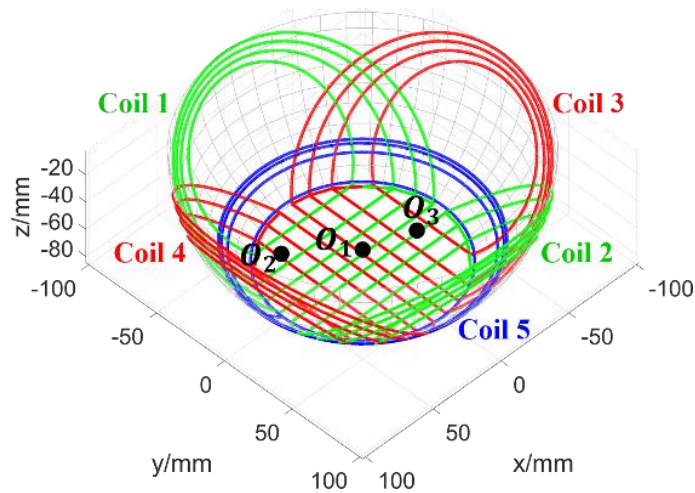


Fig. 2-14. The transmitter coils structure after the optimization.

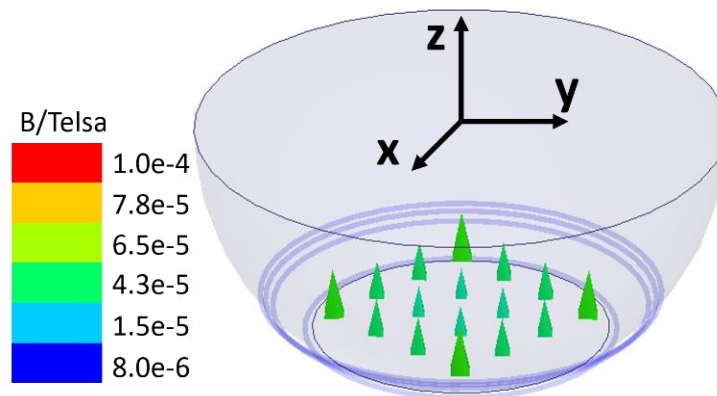


Fig. 2-15. Field distribution at the base with the optimized coil 5.

After the coil optimization, the magnetic field distribution of each transmitter coil is uniform in the target area. With a uniformly distributed  $x$ ,  $y$ ,  $z$  direction field, the 3D uniform rotating field can be achieved with modulated excitation current  $i_1(t)$ ,  $i_2(t)$ ,  $i_3(t)$ , defined in (2)-(4) in section 2.1. The magnetic field distribution at a different time instant at base is shown in Fig. 2-16. Compared with the non-optimized case in Fig. 2-5, the field distribution at a different time instant is more uniform. Similarly to the previous case, the 3D field trajectory at two example points  $O_1(-5, 5, -82$  mm),  $O_2(30, -30, -78$  mm) is obtained in Fig. 2-17. Compared to the non-optimized case in Fig. 2-6, the magnetic field trajectory after optimization is much more uniform. Therefore, free positioning

characteristics of the receiver unit with arbitrary orientation is achieved at the base of the bowl. With this characteristic, a small portable device can be charged flexibly at the base.

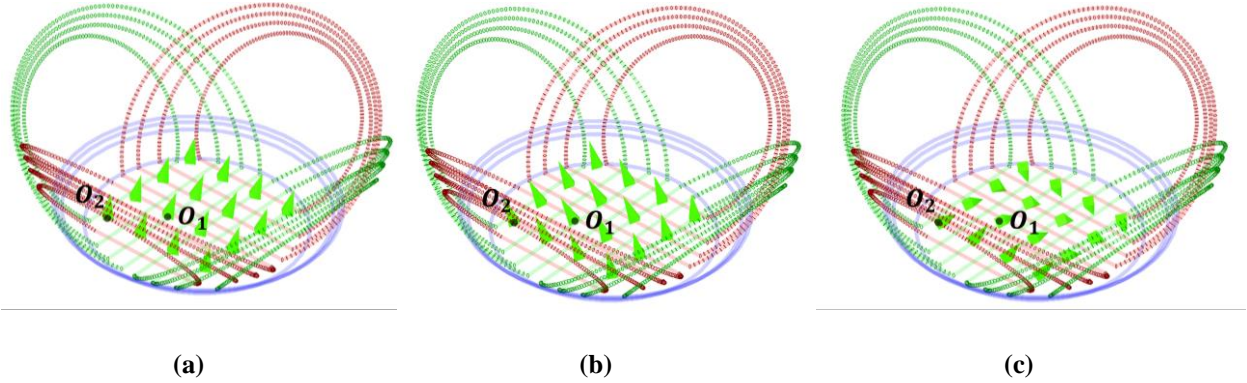


Fig. 2-16. Magnetic field distribution at different time instant with optimized coils structure. (a)  $\omega_1 t = \pi/10, \omega_0 t = \pi/4$ . (b)  $\omega_1 t = \pi/8, \omega_0 t = 7\pi/4$ . (c)  $\omega_1 t = 5\pi/4, \omega_0 t = 15\pi/8$ .

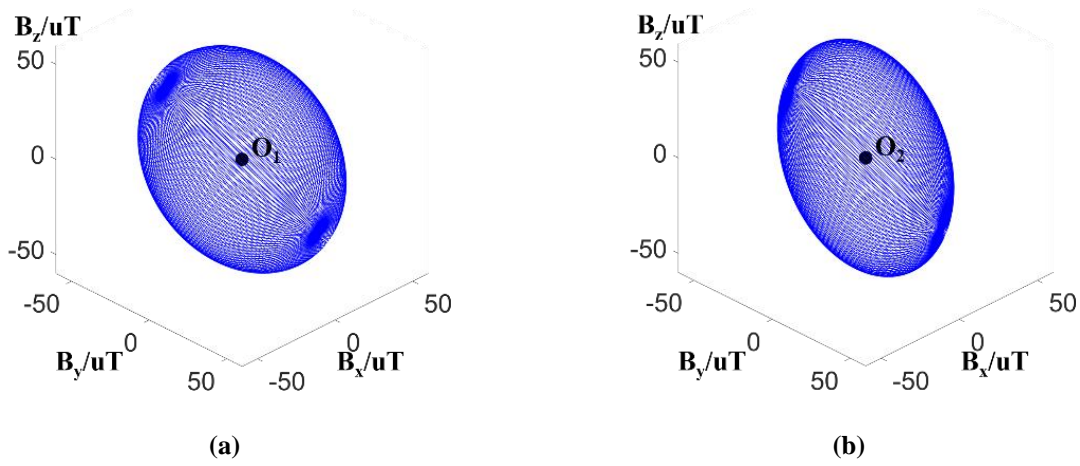
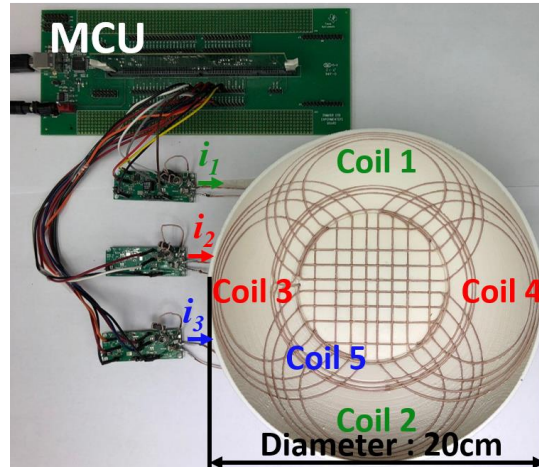


Fig. 2-17. Magnetic field trajectory at two example points after the coil optimization. (a) At  $O_1$ . (b) At  $O_2$ .

## 2.4 Experiment Verification

To validate the previous analysis, a 3D omnidirectional WPT system is built, as shown in Fig. 2-18. To precisely control the geometry of the coils, an Ultimaker 2 Go 3D printer is utilized to print the bowl fixture with grooves cut in the inner surface of the bowl fixture. Litz wire is adopted to fabricate the coils, and it consists of 450 strands of AWG 48 wires. The litz wire is manually placed in the groove.



**Fig. 2-18. Experiment setup of proposed omnidirectional WPT system.**

In the hardware, three sets of circuits are built to drive three sets of coils with modulated excitation current. The detailed implementation of the modulation will be discussed in Chapter 6. Coil 1 and coil 2 are connected in series and the experiment excitation current waveform is  $i_1$ , as shown in Fig. 2-19. Coil 3 and coil 4 are connected in series and experiment excitation current waveform is  $i_2$ . The current waveform of bottom coil 5 is  $i_3$ . Here, the carrier frequency of the excitation current is 6.78 MHz and the modulation frequency is 450 Hz.

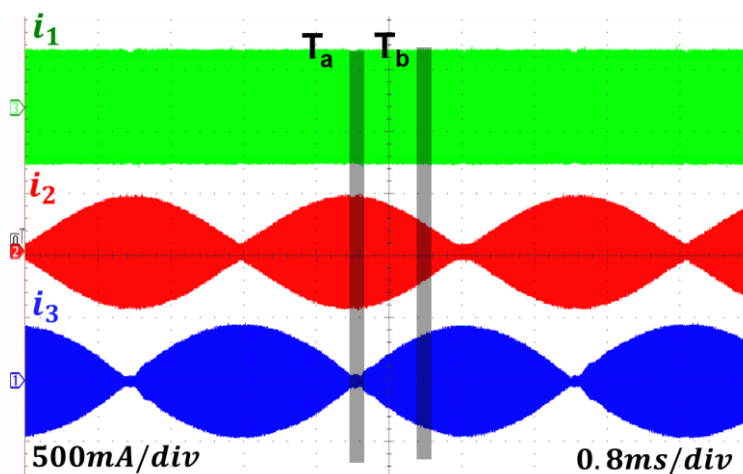


**Fig. 2-19. Experiment waveform of modulated transmitter coils excitation current in proposed omnidirectional WPT system.**

## A. Magnetic Field Measurement

When the modulated excitation current flows through the transmitter coils, the magnetic field inside the bowl is measured by a near field probe. In the experiment, a Langer EMV near field probe is utilized to measure the magnetic field trajectory. The magnetic field trajectory at point  $O_1$  (defined in Fig. 2-16) during two small periods ( $T_a$  and  $T_b$ ) is shown in Fig. 2-20. The blue line is the magnetic field trajectory calculated by the analytical model. The red line is the measured magnetic field trajectory. As demonstrated by Fig. 2-20 (a) and (b), there is little difference between calculation and measurement result. Therefore, the analytical model to calculate magnetic field, built in this paper, is verified. As demonstrated in Fig. 2-20, the magnetic field trajectory is in a ring shape during  $T_a$  and  $T_b$ . In one modulation period, the ring shape magnetic field trajectory forms a surface on an ellipsoid, as shown in Fig. 2-21. Therefore, an omnidirectional magnetic field is achieved at point  $O_1$  with the proposed coil structure. The magnetic field trajectory at  $O_2$  is also measured and is shown in Fig. 2-21. With the measurement result, uniform omnidirectional magnetic field distribution at base is verified.

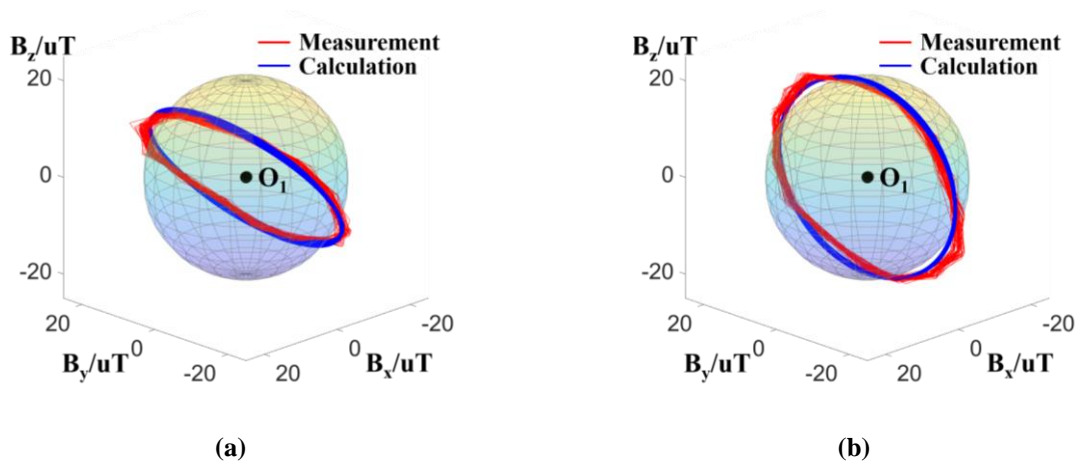
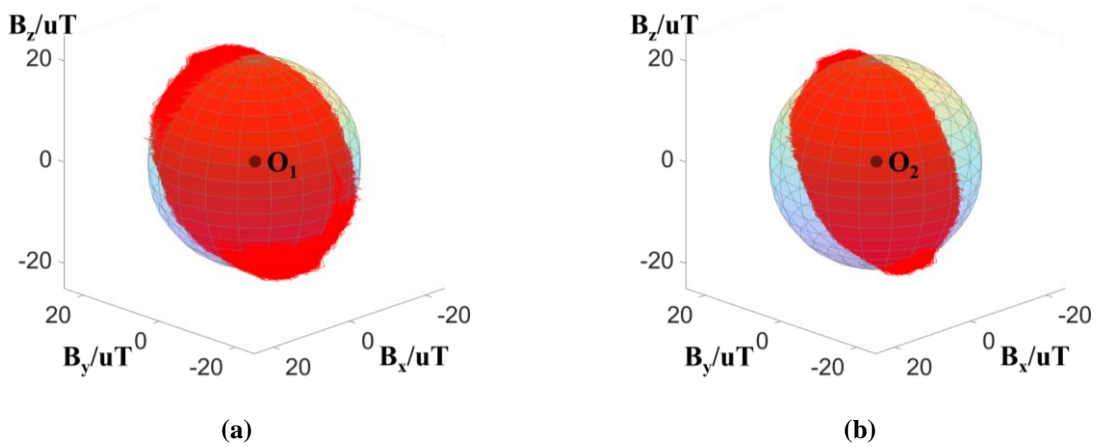


Fig. 2-20. The magnetic field trajectory at point  $O_1$ . (a) During  $T_a$ . (b) During  $T_b$ .



**Fig. 2-21. The magnetic field trajectory measurement result. (a) At  $O_1$ . (b) At  $O_2$ .**

### B. Testing Result for Charging Wearable Device Receiver

A 35 x 35mm square receiver coil (3.7  $\mu\text{H}$ , 0.7  $\Omega$ ) for an Apple Watch is fabricated to verify free positioning and omnidirectional powering characteristics. The turns number of the receiver coil is designed to satisfy the output voltage requirement of the receiving device. The receiver coil can either lay on the base (receiver in horizontal plane) or stand on the base of the bowl (receiver in vertical plane), as shown in Fig. 2-22. When the receiver coil lays on the base, the orientation is fixed, and the position is characterized by the coordinate  $(x, y, z)$  of the center point O. The output voltage test results for different positions shown in Fig. 2-23(a). Due to the symmetry of the transmitter coils structure, only the test result in one quarter of the base area is plotted. When the receiver coil stands on the base, the orientation is flexible and is characterized by yaw rotation angle  $\theta$ , as defined in Fig. 2-22. The output voltage test results for different orientations for two positions (30, 10, -65 mm) and (5, 5, -65 mm) are shown in Fig. 2-23(b).

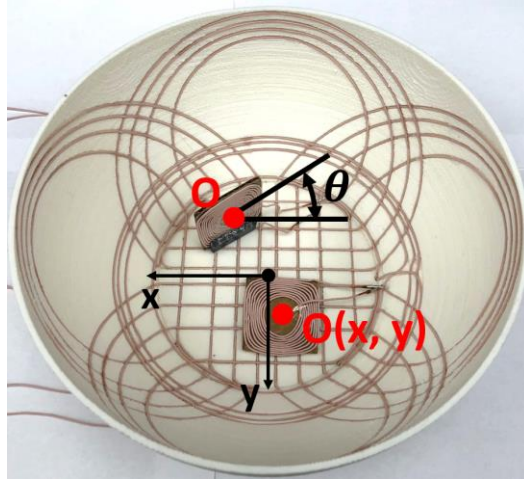
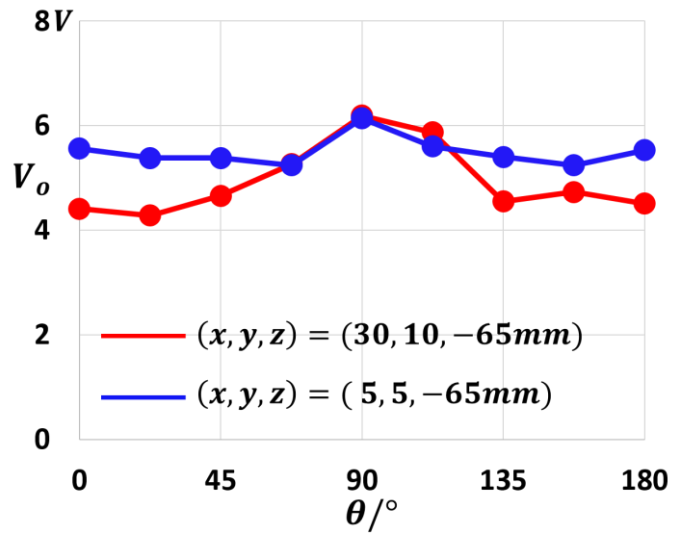
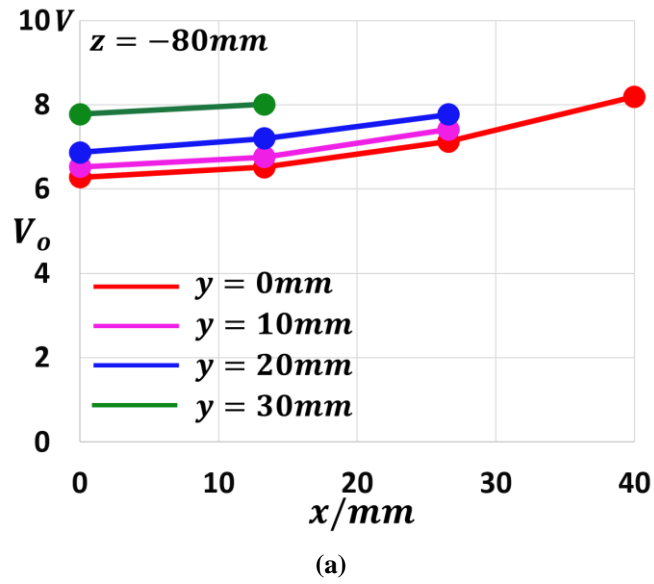


Fig. 2-22. Possible positioning of a receiver coil for wearable devices.



(b)

**Fig. 2-23. Output voltage measurement results for an apple watch receiver. (a) When laying on the base. (b) When standing on the base.**

According to the measurement results, the output voltage is 4.2 ~8V for all possible positioning and orientations of a smart watch receiver in the setup. Free positioning and omnidirectional powering characteristics are verified. There is no longer a need to align a small portable device receiver unit with the transmitter coils, making it more convenient for customer use. The power transfer efficiency is related to the number of excited transmitter coils. For example, when a receiver coil lays on the base of the bowl, only the bottom coil should be excited to charge the device. In this case, the system efficiency is around 60 % at 2.5 W output. When the receiver coil stands on the base of the charging bowl, two side coils are excited, the system efficiency is around 50 % at 2.5 W output.

### C. Testing Result for Charging Smart Phone Receiver

A 65 x 50 mm rectangular receiver coil (4.7 uH, 0.6  $\Omega$ ) for a typical smart phone is fabricated. The turns number of the receiver coil is designed to satisfy the output voltage requirement of the receiving device. To describe the receiver coil positioning in the charging bowl,  $\theta_1$  and  $\theta_2$  are adopted as shown in Fig. 2-24. Here,  $\theta_1$  is the angle between the receiver center line and transmitter center line, and  $\theta_2$  is the vertical slope of the receiver coil plane. With  $(\theta_1, \theta_2)$ , the smart phone receiver position in the bowl is determined.

In the charging test, only the side coil which is near the receiver coil is selectively excited, and other transmitter coils are not excited. The output voltage, system efficiency, as well as coil to coil efficiency for different receiver positioning, is shown in Fig. 2-25. The system efficiency accounts for the loss in the transmitter circuit, coil conduction loss, and rectifier loss. The coil to

coil efficiency only accounts for coil conduction loss. Due to the symmetry of the transmitter coils structure, test results in only one quarter of the charging bowl are plotted. As shown in Fig. 2-25, the system efficiency is 68~80 % and coil to coil efficiency is 85~95 % at 5 W output for all possible receiver positioning.

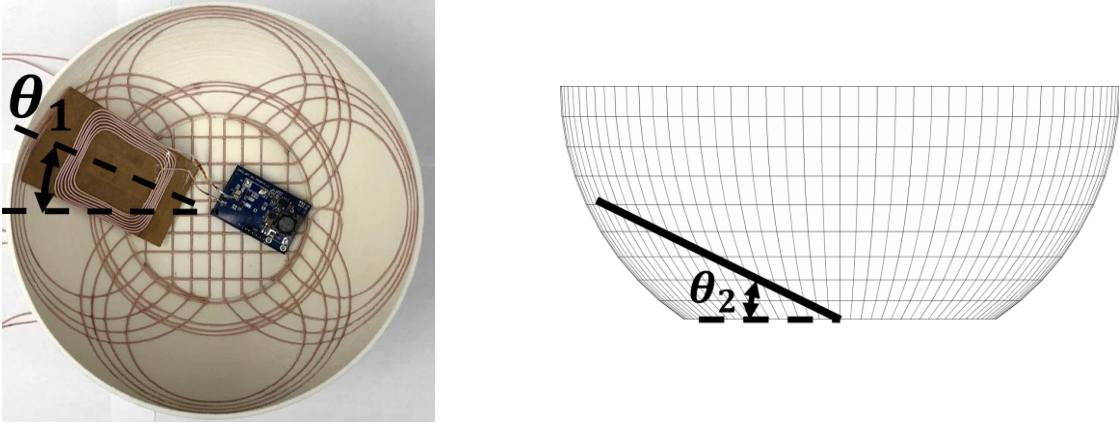
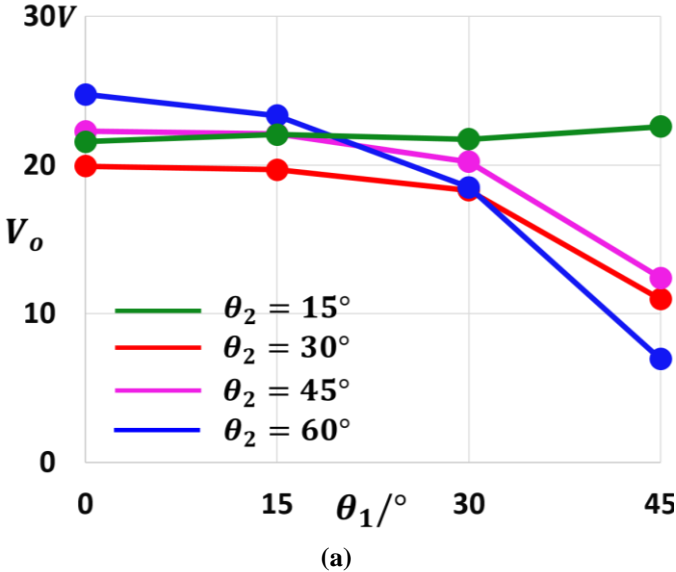


Fig. 2-24. Smart phone receiver positioning description parameter ( $\theta_1, \theta_2$ ).



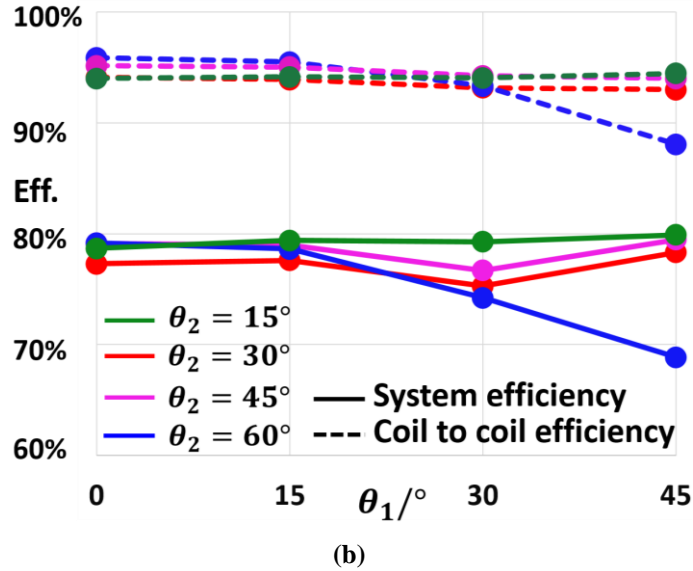


Fig. 2-25. Output voltage and efficiency measurement result for smart phone receiver with different positioning. (a). Output voltage; (b). Efficiency.

In summary, a planar smart phone device is charged efficiently with free positioning characteristics in the proposed charging receptacle. For a small portable device, which is inclined to stay on bottom of charging bowl due to gravity, uniform omnidirectional magnetic field distribution is utilized to charge it. This is regardless of arbitrary positioning or orientation.

## 2.5 Conclusion

In this chapter, omnidirectional WPT systems reported in current literature are reviewed and compared, and a novel bowl-shaped transmitter coils structure is proposed. An analytical model to calculate magnetic field distribution of a 3D transmitter coils structure is built and verified by measurement result. The design methodology for the transmitter coils is also proposed. With the design methodology, strong uniform omnidirectional magnetic field distribution is achieved, and free positioning of a receiver device with arbitrary orientation is enabled. A 6.78MHz omnidirectional WPT system is built. Both free positioning and omnidirectional power transfer

capability are verified by the magnetic field measurement result. The system efficiency for a smart phone dimension receiver is 68~80 % at 5 W output. The maximum system efficiency for a wearable device dimension receiver is 60 % at 2.5 W output. The proposed wireless charging bowl offers both spatial freedom and good efficiency, making it a promising charging solution for mobile devices [90].

# Chapter 3     6.78MHz Resonant Converter for Omnidirectional WPT System

## 3.1 Introduction

Compensation networks are normally used to improve the power transfer capability of a wireless power transfer system with loosely coupled coils. The requirements of the compensation networks in an omnidirectional wireless power transfer system are identified as follows: 1). coupling independent resonant frequency; 2). load independent output voltage; 3). load independent transmitter coil current; 4). maximum efficiency power transfer; 5). soft switching of active devices.

The series-series (SS) compensation scheme, shown in Fig. 3-1, is widely adopted for a WPT system due to the simplicity and its coupling-independent resonance characteristics [53]. Herein,  $L_p$  and  $L_s$  are the self-inductances of the transmitter coil and receiver coil.  $k$  is the coupling coefficient between the transmitter coil and receiver coil.  $C_p$  and  $C_s$  are the compensation capacitors in primary side and secondary side and they are designed to resonate with  $L_p$  and  $L_s$  respectively at the same frequency:

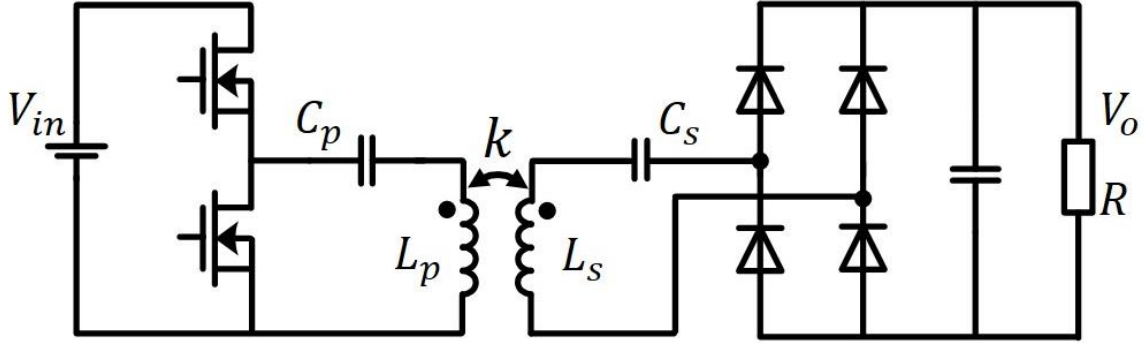


Fig. 3-1. The series – series compensated converter.

$$\frac{1}{\sqrt{L_p C_p}} = \frac{1}{\sqrt{L_s C_s}} \quad (3.1)$$

The frequency characteristics of the input to output voltage gain of a SS compensated converter is analyzed with only fundamental component of the input voltage source considered. Herein, the resistance of switching devices, the coupled coils and the rectifier bridge is neglected for simplicity. Two typical voltage gain curves with different load conditions under different coupling coefficients are shown in Fig. 3-2.

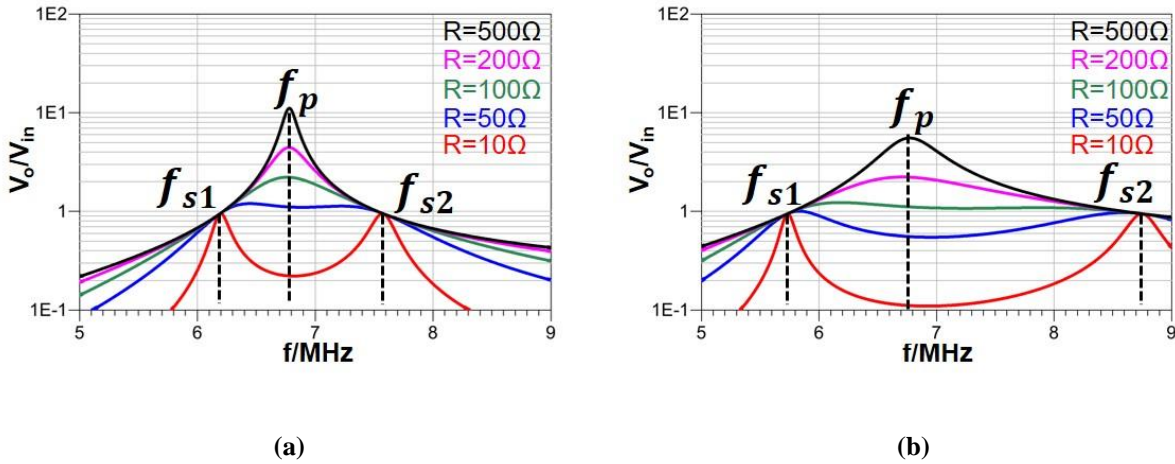


Fig. 3-2. Voltage gain curves of a SS compensated converter under different coupling condition. (a)  $k = 0.4$ . (b)  $k = 0.2$ .

As demonstrated by Fig. 3-2, there are three resonant frequencies in the SS compensated converter: one parallel resonant frequency  $f_p$ , and two series resonant frequencies  $f_{s1}$ ,  $f_{s2}$ . At the

parallel resonant frequency  $f_p$ , the output voltage is proportional to the load resistance. In other words, the output current is irrelevant to the load condition. The load-independent output current characteristic at  $f_p$  is achieved by the parallel resonant tank ( $L_p, C_p$ ) and  $f_p$  is determined by

$$f = \frac{1}{2\pi\sqrt{L_p C_p}} \quad (3.2)$$

As illustrated by (3.2), the requirement I (coupling independent resonant frequency) is satisfied when operated at  $f_p$ . However, the output voltage has a significant fluctuation at  $f_p$  and the requirement II (load independent output voltage) is not satisfied, which leads to too much burden for the voltage regulation circuit. Therefore, it's not desired to operate at the parallel resonant frequency  $f_p$ .

At two series resonant frequencies  $f_{s1}$  and  $f_{s2}$ , the output voltage is independent of load condition. The load independent output voltage characteristic is achieved by the series resonance between leakage inductances and the compensation capacitor. Assuming the transmitter coil is identical with the receiver coil, the equations for  $f_{s1}$  and  $f_{s2}$  are simplified as

$$f_{s1} = \frac{1}{2\pi\sqrt{(1+k)L_p C_p}} \quad (3.3)$$

$$f_{s2} = \frac{1}{2\pi\sqrt{(1-k)L_p C_p}} \quad (3.4)$$

Here, two series resonant frequencies are related to the coupling coefficient and cannot satisfy the requirement I. In summary, the SS compensated converter cannot even satisfy requirement I and II at the same time.

Other than series-series resonant converter, LLC resonant converter, which is very popular in power electronics society, is also evaluated in this section [60]. The coupled coil is represented by cantilever model in LLC circuit diagram as shown in Fig. 3-3 [61]. LLC voltage gain characteristics

in different coupling condition with variable load resistance is shown in Fig. 3-4, with only fundamental component of input voltage source considered.

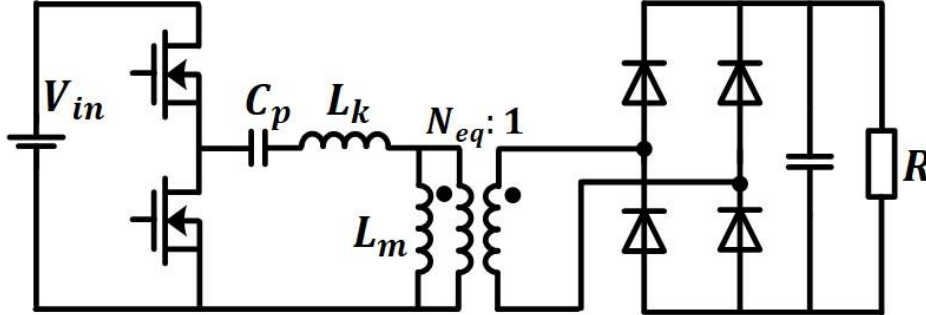


Fig. 3-3. The LLC resonant converter.

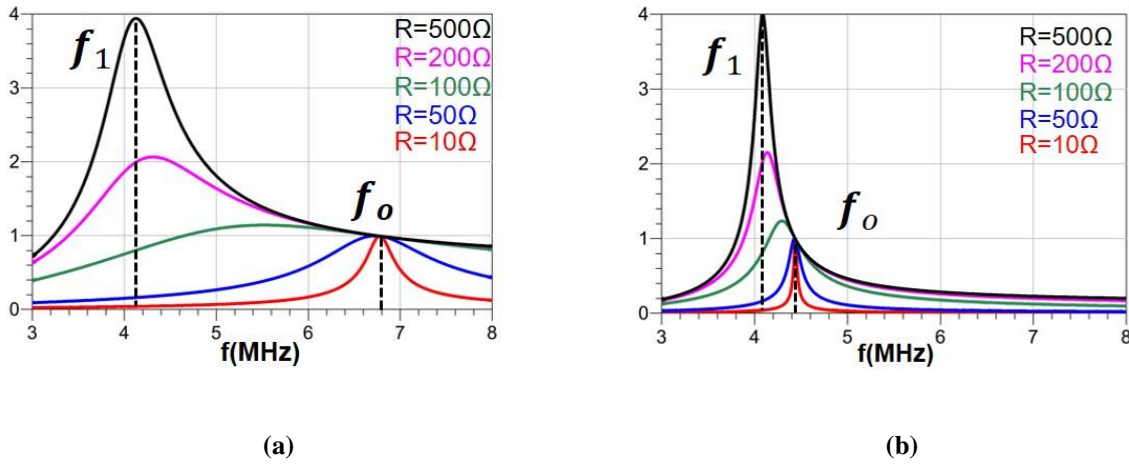


Fig. 3-4. Voltage gain curves of a LLC converter under different coupling condition. (a)  $k = 0.4$ . (b)  $k = 0.2$ .

There is two resonant frequency  $f_o, f_1$  in the LLC gain characteristics as shown in Fig. 3-4:

$$f_o = \frac{1}{2\pi\sqrt{L_k C_p}} \quad (3.5)$$

$$f_1 = \frac{1}{2\pi\sqrt{(L_p + L_m)C_p}} \quad (3.6)$$

In LLC resonant converter, resonant frequency  $f_o$  is the most efficient operation point with zero voltage switching in wide load range [60]. In WPT application, this optimal point is sensitive to coupling change because it's determined by leakage inductance. And leakage inductance is subject

to coupling change. Therefore, it's difficult to operate at this point in variable coupling case. As for resonant frequency  $f_l$ , there is no constant voltage output characteristics although it is independent of coupling. It's difficult to control the output voltage in such large fluctuation to charge the battery. Therefore, LLC resonant converter cannot satisfy all the requirement either.

As for series-series resonant converter and LLC resonant converter, the resonant frequency with good voltage controllability is dependent of coupling. Therefore new resonant converter topology, which has coupling independent resonant frequency with voltage source output characteristics, is studied in next section.

### 3.2 Synthesis of Multiple Element Resonant Converter

The general ac circuit model of a wireless power transfer system, with only the fundamental component considered, is shown in Fig. 3-5. The coupled coils are represented by the mutual inductance model. Herein,  $L_p$  and  $L_s$  are the self-inductances of the transmitter coil and receiver coil;  $M$  is the mutual inductance of the coupled coils.  $I_p$  and  $I_s$  are the transmitter coil current and receiver coil current in phasor domain. The transmitter coil is driven by an ac voltage source ( $v_{ac}$ ) with a primary compensation network. The receiver coil is followed by a compensation network and the loading circuit. Here,  $R_e$  is the fundamental equivalent ac loading resistance of the system.

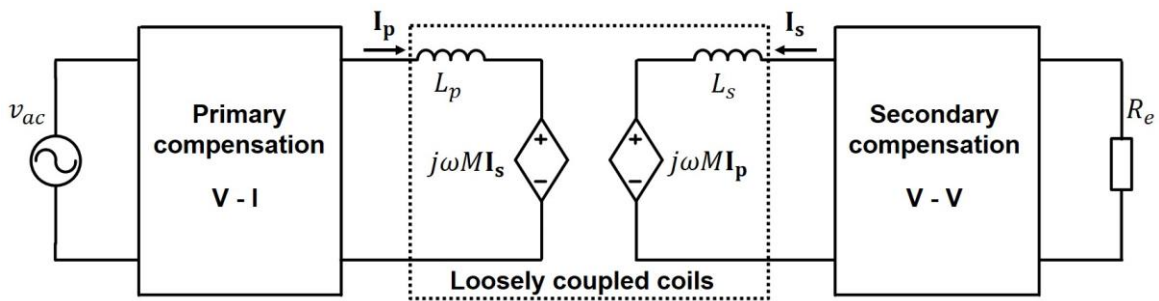


Fig. 3-5. The general ac circuit model of a wireless power transfer system.

To satisfy the third criteria listed above (load independent transmitter coil current  $I_p$ ), the primary compensation network should change the input voltage source to a current source. The parallel resonant tanks, shown in Fig. 3-6, are the simplest network to achieve this goal [59]. The Norton's equivalent circuit of one parallel resonant tank, as an example, is illustrated in Fig. 3-6(b). A voltage source in series with the inductor  $L_r$  is equivalent to a current source in parallel with the inductor  $L_r$ . The phasor ( $I_{ac}$ ) of the equivalent current source is calculated by the Norton's Theorem:

$$I_{ac} = \frac{V_{ac}}{j\omega L_r} \quad (3.7)$$

At the resonant frequency of  $L_r$  and  $C_r$ , the parallel resonant tank has an infinity impedance, and the equivalent current source is directly connected to the transmitter coil; therefore, the primary coil current  $I_p$  equals  $I_{ac}$ , which is irrelevant to the load and coupling condition at the resonant frequency of  $L_r$  and  $C_r$ . Moreover, the resonant frequency is also independent of the coupling condition. Therefore, the first and third criterion are satisfied when parallel resonant tanks are adopted as the primary compensation network.

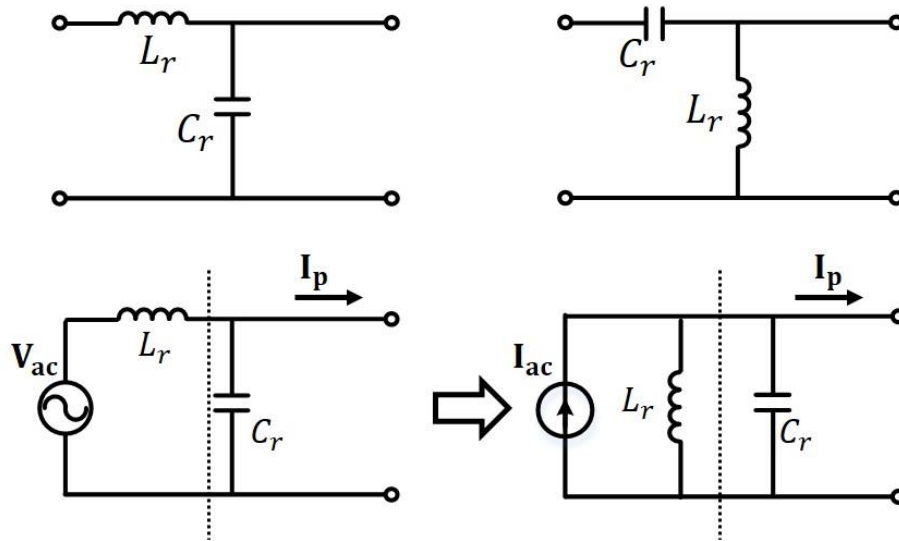


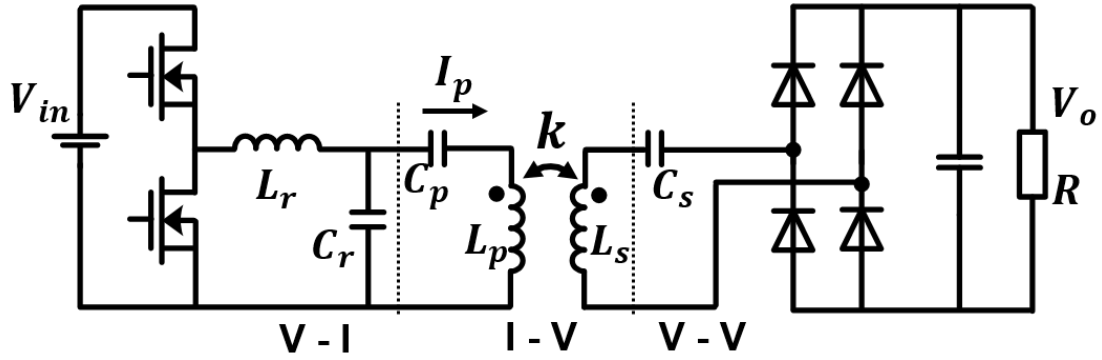
Fig. 3-6. Parallel resonant tank and its equivalent circuit with the Norton's equivalent circuit.

With load independent primary coil current  $\mathbf{I}_p$ , the voltage ( $j\omega M I_p$ ) induced within the receiver coil is also irrelevant to the load condition. If the secondary compensation network canceled the reactance of  $L_s$ , the voltage source would be directly applied on the equivalent resistance  $R_e$ . The simplest compensation network to achieve this goal is a capacitor ( $C_s$ ) which is in series with the receiver coil. Meanwhile, the coil to coil efficiency is also maximized by cancelling the reactance in the receiver loop [53].

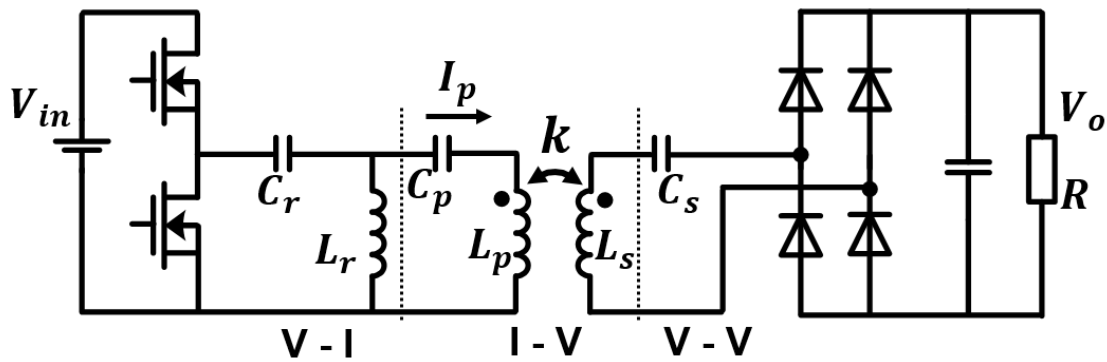
In a MHz converter, the ZVS operation for switching devices is essential to reduce the switching loss and switching related EMI problem. The necessary condition for ZVS of primary side devices is the input impedance must be inductive, which means the input current lags the input voltage, and ZVS is naturally achievable [54]. However, the inductive input impedance results in some reactive power flowing in the system and the associated circulating power losses. Therefore, the input impedance must be controlled precisely to minimize the circulating energy. To allow more design freedom, a capacitor ( $C_p$ ) is added in the converter to tune the angle of the input impedance [62]. Due to the current source characteristic of the transmitter coil current,  $C_p$  does not impact the system operation if it is in series with the transmitter coil.

Considering these requirements, two resonant converters, named as the LCCL-LC resonant converter and the CLCL-LC resonant converter, are derived in Fig. 3-7. It is worth noting that the proposed synthesis methodology is a systematic way to generate different compensation topologies and these two converters are the simplest. Compared with the CLCL-LC resonant converter, the resonant capacitor  $C_r$  in the LCCL-LC converter can bypass the high frequency harmonics of the input voltage source. Therefore, the transmitter coil current contains the lower harmonics component in the LCCL-LC resonant converter. The harmonics component decreases the load independency of the transmitter coil current and may interfere with the communication chips in

the receiver device. Considering this, the LCCL-LC resonant converter is desired and evaluated in detail in this work.

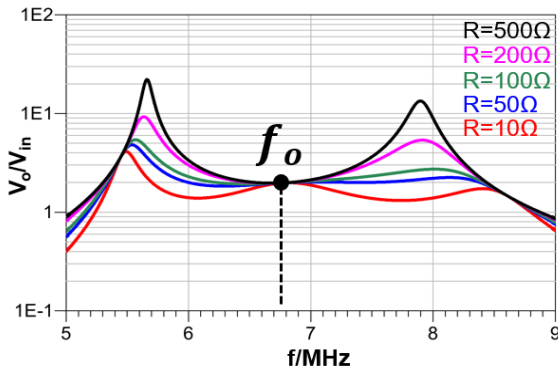


(a)

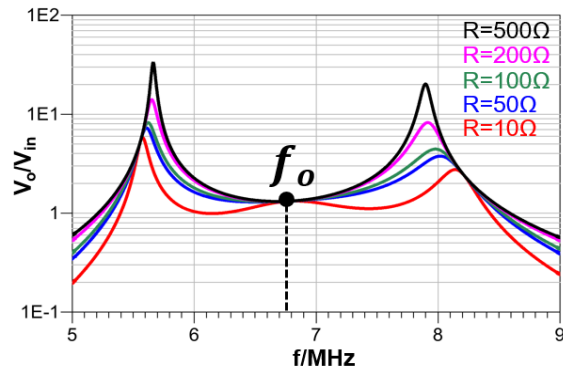


(b)

Fig. 3-7. Two resonant converter candidates. (a) LCCL-LC resonant converter. (b) CLCL-LC resonant converter.



(a)



(b)

**Fig. 3-8. Voltage gain curves of the LCCL-LC converter under different coupling coefficient. (a)  $k = 0.4$ . (b)  $k = 0.2$ .**

The voltage gain characteristics of the LCCL-LC resonant converter under different coupling conditions are shown in Fig. 3-8. Herein, the resistance of the switching devices, the coupled coils, and the rectifier bridge in the converter are neglected for simplicity. The resonant frequency  $f_o$  is determined by:

$$f_o = \frac{1}{2\pi\sqrt{L_r C_r}} = \frac{1}{2\pi\sqrt{L_s C_s}} = 6.78\text{MHz} . \quad (3.8)$$

As illustrated by (3.8) and Fig. 3-8, the resonant frequency  $f_o$  is irrelevant to the coupling condition, i.e. the system can operate at the optimal point with a variable coupling coefficient. Therefore, the first criterion is satisfied with this topology. The output voltage is independent of load condition at this resonant frequency, satisfying the second criterion. By the resonance of  $L_r$  and  $C_r$ , the primary coil current is constant, making the third criterion satisfied. Furthermore, the efficiency is maximized by the resonance of  $L_s$  and  $C_s$ , which is the fourth criterion. Lastly, the ZVS operation of primary devices can be achieved with proper tuning of  $C_p$ , fulfilling the fifth criterion. The design methodology to achieve the ZVS operation of the LCCL-LC resonant converter is proposed in Chapter 4. Therefore, all five criteria are met with the LCCL-LC resonant converter.

### 3.3 Experiment Verification

A 6.78 MHz LCCL-LC resonant converter for the one transmitter and one receiver case is built to verify the previous analysis. The specifications of the system for a smart phone receiver are shown in Table 3.1.

TABLE 3.1 SPECTIFICATIONS OF THE WPT SYSTEM

Specifications	Symbol	Practical Value
Input voltage	$V_{in}$	24V
Output voltage range	$V_o$	10~20V
Output power	$P_o$	5W
Switching frequency	$f_o$	6.78MHz
Transmitter coil self-inductance	$L_p$	3.09uH
Transmitter coil resistance	$R_p$	0.6 $\Omega$
Receiver coil self-inductance	$L_s$	4.7uH
Receiver coil resistance	$R_s$	0.6 $\Omega$
Coupling coefficient range	$k$	0.12~0.25
Compensation inductor	$L_r$	560nH
Compensation capacitor	$C_r$	980pF
Compensation capacitor	$C_p$	160pF
Compensation capacitor	$C_s$	118pF

The toroid core with Fair-Rite material 67 (Part number: 5967000201), which has very low loss in MHz, is adopted to build the inductor  $L_r$ . To reduce the winding ac resistance, 450/AWG48 Litz wire is utilized to wind around the toroid core. To operate at 6.78MHz, the low voltage GaN device (EPC8004) is used for primary devices. According to the circuit parameters in Table I, the experimental setup is built as Fig. 3-9. In the receiver circuit, four discrete DFLS130 diodes are adopted for the rectification due to their small conduction voltage drop. A simple resistor after the rectifier bridge is manually adjusted to emulate the function of the battery charging chip. In the experimental setup, the TI microcontroller TMS320C28346 demo board is used to give the PWM signals to the half bridge of the LCCL-LC circuit and the system is powered by an Agilent E3631A DC power source. The experimental input voltage and current waveform with only one transmitter coil (coil 1), excited to power the receiver coil, is first shown in Fig. 3-10. In the test, the coupling coefficient between coil 1 and the receiver coil is 0.12, and the load resistor is 20  $\Omega$ . As illustrated by Fig. 3-10, ZVS of the primary device is well achieved, and the waveform is clean at 6.78 MHz.

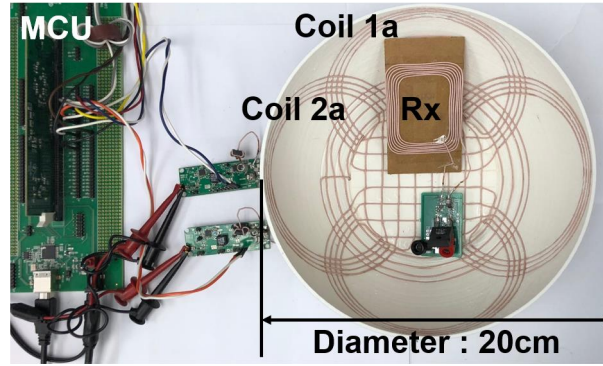


Fig. 3-9. The physical setup of the omnidirectional IPT system.

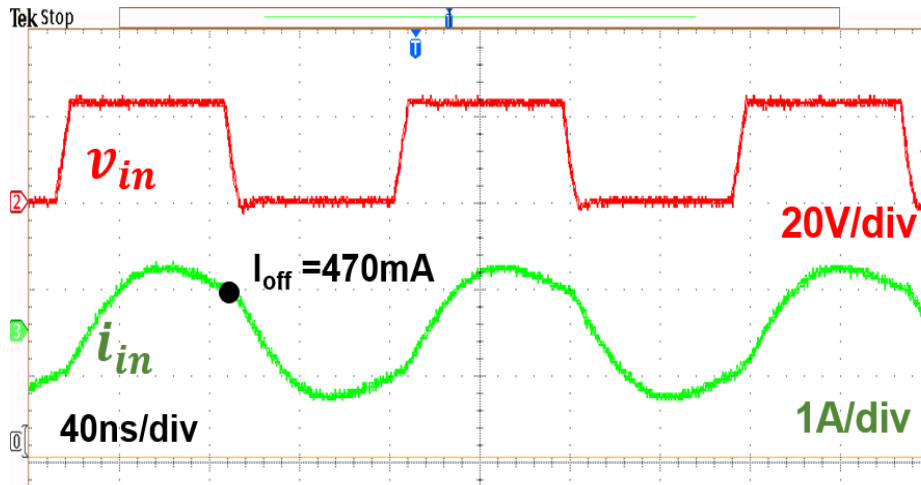


Fig. 3-10. Experimental waveform of switching node voltage and current.

Fig. 3-11 shows the comparison of the experimental and calculated  $rms$  value of the coil 1a excitation current ( $I_{p\_rms}$ ) as a function of the load resistance under  $k = 0.12$  and  $k = 0.2$ . The load resistance range for two coupling conditions is adjusted to make sure that the output power is 5 W. The calculated results for  $I_{p\_rms}$  fit well with the experimental results, validating the load and coupling independence of the transmitter coil current. The measured output voltage ( $V_o$ ) of the LCCL-LC circuit is also plotted in Fig. 3-11 with another vertical axis. There is some mismatch between the calculated results and experimental results since the loss of the converter and the reactance of the rectifier bridge are not considered in the theoretical analysis. This mismatch becomes smaller when load resistance increases, since the voltage drop on each component

reduces with a lower current level. As illustrated by the experimental results, the output voltage is independent of the load condition, and good voltage controllability is achieved with the LCCL-LC resonant converter.

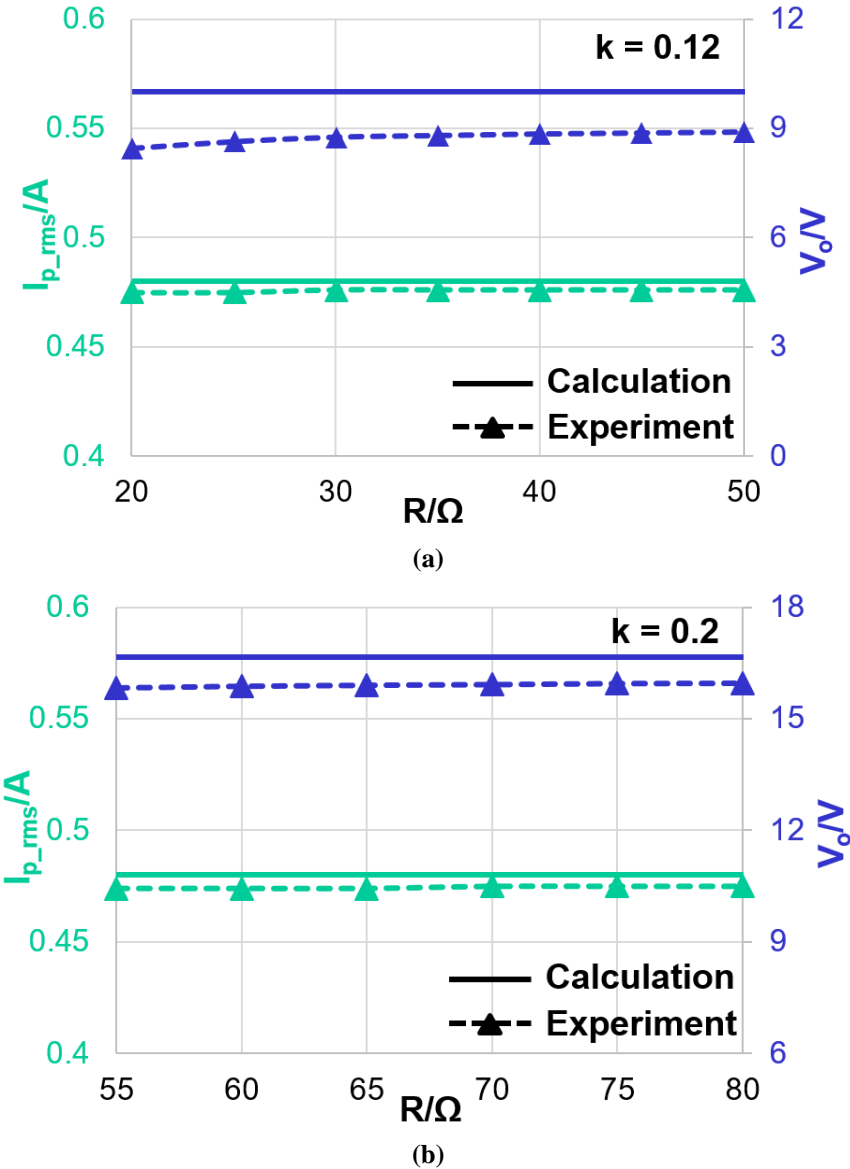


Fig. 3-11. Experimental and calculated results of the *rms* current of transmitter coil and the output voltage. (a)  $k = 0.12$ . (b)  $k = 0.2$ .

### **3.4 Conclusion**

The special challenges in resonant converter for omnidirectional WPT system are identified. A systematic synthesis strategy to find suitable resonant converter topology is proposed. The LCCL-LC and CLCL-LC resonant converters are derived to satisfy all the requirements with lowest compensation components. Due to the low harmonics content, the LCCL-LC converter is promising in consumer electronics applications because of strict EMI regulation. A 6.78MHz LCCL-LC converter is built to validate all the benefit of the LCCL-LC converter in omnidirectional WPT system.

# Chapter 4      **Soft-switching Realization of the 6.78MHz**

## **LCCL-LC Converter**

### **4.1 Introduction**

In consumer electronics applications, MHz WPT systems are used to improve the charging spatial freedom [63]. 6.78 MHz is selected as the system operation frequency, according to the AirFuel standard, a wireless charging standard for commercial electronics [64]. The zero voltage switching (ZVS) operation of the switching devices is essential in reducing the switching loss and the switching related electromagnetic interference (EMI) issue. In omnidirectional WPT systems, the LCCL-LC resonant converter topology is selected due to its benefits as mentioned in Chapter 3. In [65], ZVS analysis in an LCCL-LC circuit is conducted without considering the rectifier reactance and the dead-time period. In a MHz system, the rectifier reactance caused from junction capacitance of the diode can no longer be neglected [66], [67]. However, an analytical model of the full bridge rectifier reactance is lacked and the impact of the rectifier reactance on the ZVS operation of the LCCL-LC converter is not evaluated [66], [67]. Therefore, a comprehensive design methodology of a 6.78MHz LCCL-LC resonant converter to achieve ZVS operation, with considering the rectifier reactance and dead-time period, is proposed in this chapter.

In omnidirectional WPT systems, there is multiple transmitter coils and ZVS analysis is much more complicated. It has never been conducted in the existing literature. Therefore, in this chapter, the ZVS analysis is extended to the case of multiple transmitter coils. Besides, there are different

excitation current control for the transmitter coil to achieve omnidirectional power transfer capability [68]. Based on the analytical model, the ZVS condition is evaluated with different excitation current control methods for the first time in the literature.

## 4.2 Reactance of Full Bridge Rectifier at 6.78MHz

The LCCL-LC resonant converter, composed of a half bridge, resonant tank and a full bridge Schottky rectifier is shown in Fig. 4-1. At 6.78MHz, the impact of the diode junction capacitance ( $C_j$ ) can no longer be neglected [66], [67]. The voltage and current waveform at the input port of the full bridge rectifier is shown in Fig. 4-2. When the current flowing through  $D_1$  and  $D_4$  goes to zero,  $D_1$  and  $D_4$  are not turning off immediately. The negative current continues to flow through the junction capacitances of  $D_1$  and  $D_4$  and build a reverse voltage across the diodes. Therefore, the rectifier voltage  $v_{rec}$  lags the current  $i_s$ , due to the commutation of diodes, which leads to capacitive loading effect. Regarding this, an equivalent capacitance  $C_{eq}$  is added in the ac equivalent circuit of the LCCL-LC converter with the fundamental approximation, as shown in Fig. 4-3. In Fig. 4-3,  $U_{in}$  is the fundamental component of the switching node voltage;  $R_{eq}$ ,  $C_{eq}$  are utilized to model the rectifier impedance at the fundamental frequency. During the diode commutation period, the rectifier current ( $i_s$ ) needs to remove the output junction charge ( $2Q_j$ ) stored in diodes. The charge balance equation is

$$\int_0^{2\theta/\omega_o} I_s \sin(\omega_o t) dt = 2Q_j . \quad (4.1)$$

where  $I_s$  is the amplitude of the current flowing through the receiver loop.

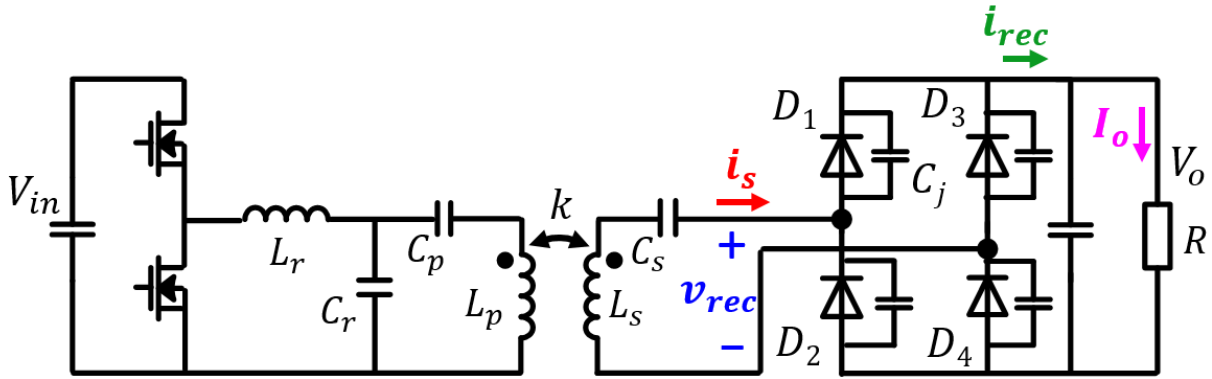


Fig. 4-1. The LCCL-LC resonant converter.

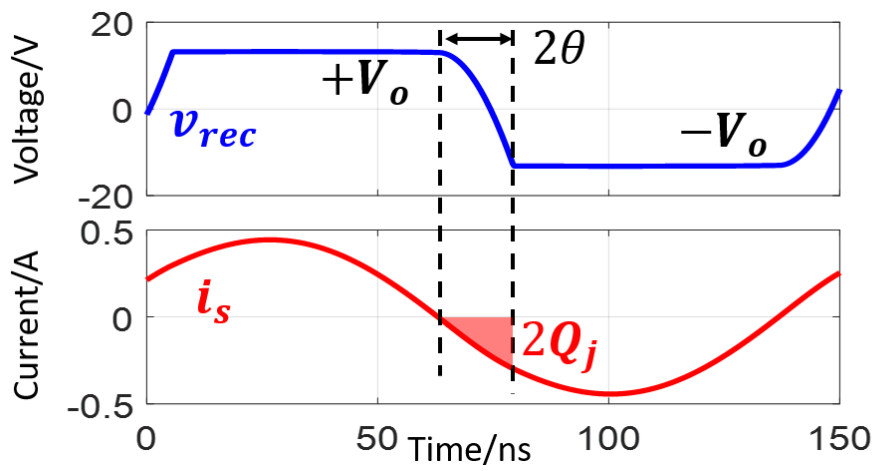


Fig. 4-2. Voltage and current waveform at the input port of the rectifier.

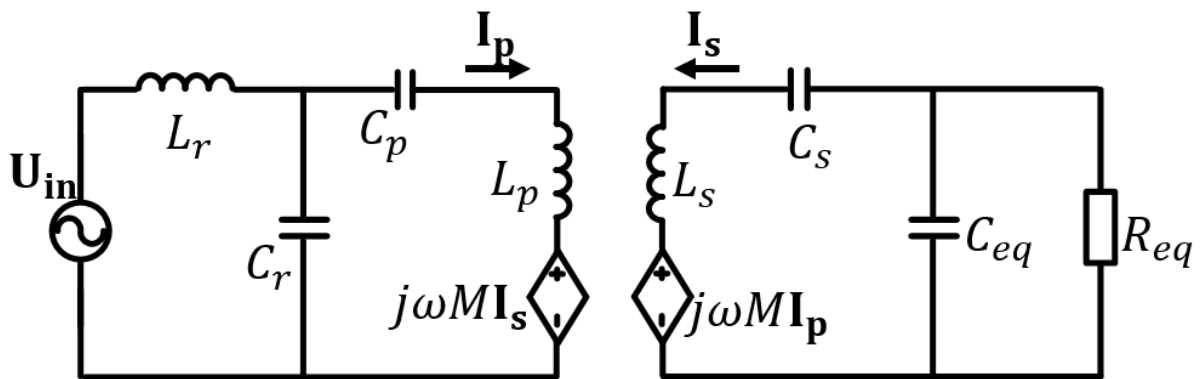


Fig. 4-3. Equivalent circuit of the LCCL-LC converter with fundamental approximation.

With fundamental approximation, the voltage and current waveform of the rectifier bridge is shown in Fig. 4-4. The phase angle between the voltage and current waveform is  $\theta$ . The real and imaginary part of the admittance seen from the rectifier input terminal is calculated as

$$\frac{I_s}{V_{rec}} \cos \theta = \frac{1}{R_{eq}}, \quad (4.2)$$

$$\frac{I_s}{V_{rec}} \sin \theta = \omega_o C_{eq}. \quad (4.3)$$

where  $V_{rec}$  is the amplitude of the fundamental component of the rectifier voltage

$$V_{rec} \approx \frac{4 \sin(2\theta)}{\pi} V_o.$$

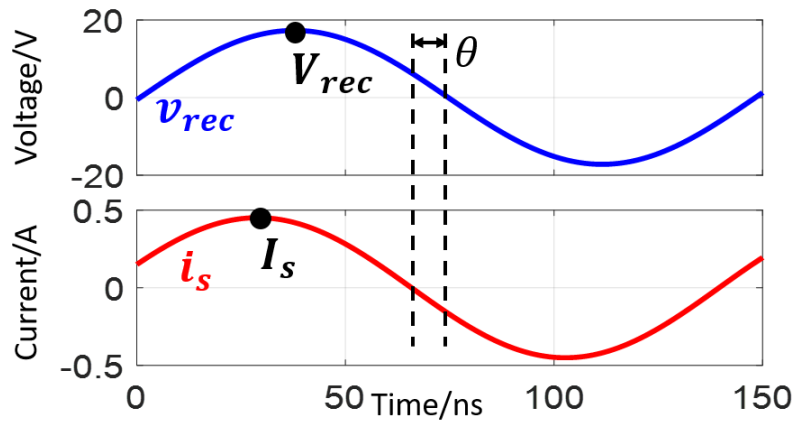


**Fig. 4-4. The voltage and current waveform of the rectifier with the fundamental approximation.**

According to (4.3),  $V_o$  and  $I_s$  are needed to solve the equivalent capacitance  $C_{eq}$ . In steady state, the average current flowing through the output capacitor would be zero. Therefore, the average current flowing after the rectifier ( $i_{rec}$ ) equals the load current ( $I_o$ ) as defined in Fig. 4-1.

$$\left[ \int_0^{T/2} I_s \sin(\omega_o t) dt - 2Q_j \right] / \left( \frac{T}{2} \right) = I_o = \frac{V_o}{R}. \quad (4.4)$$

Combing (4.1)-(4.4), there is no simple analytical solution for  $C_{eq}$ . When the discharging period ( $2\theta$ ) is less than 15% of the whole charge period, some approximation is made:

$$\frac{\sin(2\theta)}{2\theta} \approx 1. \quad (4.5)$$

The approximation error is below 10% according to Fig. 4-5. With the approximation, the analytical solution of  $C_{eq}$  and  $R_{eq}$  is obtained as

$$C_{eq} = \frac{\pi^2 \sin \theta}{4\omega_o R(\cos(2\theta) + 1)}, R_{eq} = \frac{4R(\cos(2\theta) + 1)}{\pi^2 \cos \theta}. \quad (4.6)$$

where:  $\theta = \sqrt{\frac{4RQ_j}{4RQ_j + V_o T}}$ ,  $Q_j$  is the junction charge stored at the diode junction cap.

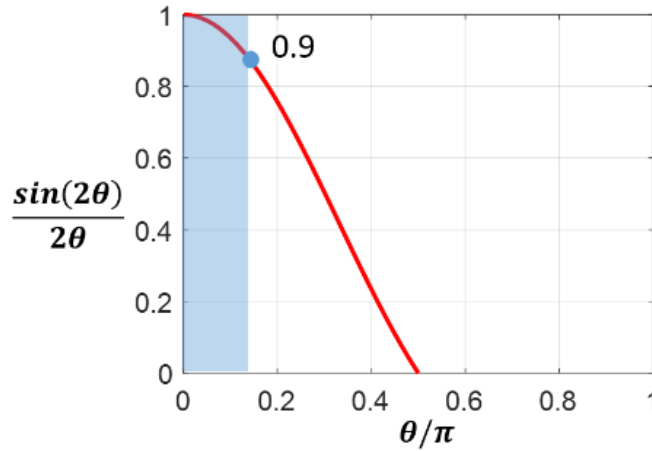


Fig. 4-5. The relationship of  $\sin(2\theta)/(2\theta)$  versus  $\theta/\pi$ .

### 4.3 ZVS Achievement in One Transmitter Coil Case

#### 4.3.1 Parameter Design for ZVS Operation

The resonant frequency of the LCCL-LC converter is designed at the system frequency (6.78 MHz) as follows:

$$f_o = \frac{1}{2\pi\sqrt{L_r C_r}} = \frac{1}{2\pi\sqrt{L_s C_s}} = 6.78\text{MHz}. \quad (4.7)$$

At the resonant frequency of  $L_r$  and  $C_r$ , the equation of the transmitter coil current  $\mathbf{I}_p$  in phasor diagram is shown in (4.8), which is independent of the coupling and load conditions [62].

$$\mathbf{I}_p = \frac{\mathbf{U}_{in}}{j\omega_o L_r}. \quad (4.8)$$

According to the Faraday's Law, the transmitter coil current induces a controlled voltage source in the receiver loop, as shown in Fig. 4-3. With the resonance of  $L_s$  and  $C_s$ , the voltage source directly applies to the input port of the rectifier. The amplitude of the fundamental component of the rectifier voltage at the resonant frequency ( $f_o$ ) is derived as

$$V_{rec} = |j\omega_o M \mathbf{I}_p| = \left| j\omega_o M \frac{2/\pi V_{in}}{j\omega_o L_r} \right| = \frac{2k\sqrt{L_p L_s}}{\pi L_r}. \quad (4.9)$$

As shown in Fig. 4-2, the rectifier voltage waveform is trapezoidal in approximation, and the value of the upper plateau is the DC output voltage  $V_o$ . The phase angle of the diode commutation period is  $2\theta$ . According to the Fourier series expansion of a trapezoidal signal, the amplitude of the fundamental component of the rectifier voltage is

$$V_{rec} = \frac{4}{\pi} \frac{\sin(2\theta)}{2\theta} V_o \approx \frac{4}{\pi} V_o. \quad (4.10)$$

The diode commutation period is less than 15% of the whole switching period in a practical system ( $\theta < 0.15\pi$ ); therefore, some approximation is made in (4.10). Combing (4.9) and (4.10), the output voltage of the converter is solved as

$$V_o = \frac{k\sqrt{L_p L_s}}{2L_r} V_{in}. \quad (4.11)$$

Here,  $k$ ,  $L_p$ , and  $L_s$  are determined by the coil design; therefore,  $L_r$  is designed to satisfy the output voltage requirement. After  $L_r$  is determined,  $C_r$  can be determined according to (3). Meanwhile, the compensation capacitor  $C_s$  is designed to resonate with  $L_s$  at 6.78 MHz. Therefore,  $L_r$ ,  $C_r$ ,  $L_p$ ,  $L_s$ , and  $C_s$  are determined, and there is only  $C_p$  left in the parameter design for the resonant tank in the LCCL-LC converter.

As for  $C_p$ , it is tuned to achieve ZVS with minimum circulating energy in the system. The typical input voltage, input current, and capacitor  $C_r$  voltage waveforms in the LCCL-LC resonant converter are shown in Fig. 4-6. To achieve ZVS, the turn off current must be high enough to fully discharge the junction capacitor of the switching devices during a predetermined dead-time period ( $t_d$ ). Herein,  $I_{off}$  is defined as the instant value of the input current at the middle point of the dead-time period ( $t = T/2 = 1/2f_o$ ).

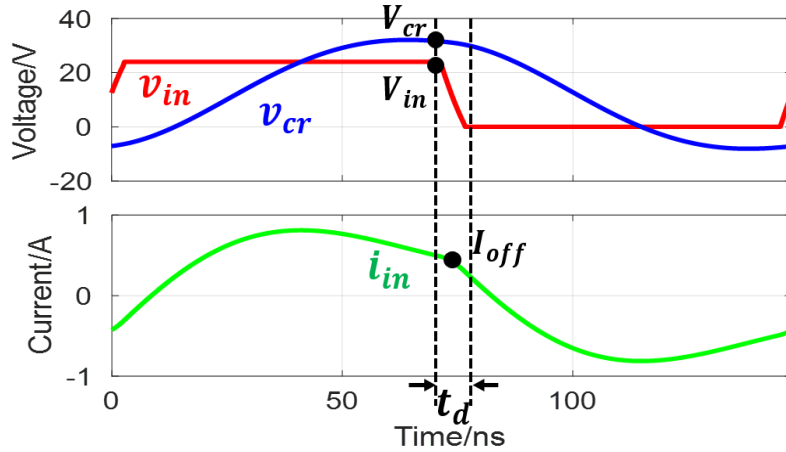


Fig. 4-6. The voltage and current waveform of the rectifier with the fundamental approximation.

#### 4.3.2 Turn-off current Calculation

To calculate  $I_{off}$ , the equivalent circuit of the converter referred to the primary side is shown in Fig. 7, where  $Z_{ref}$  is the reflected frequency-dependent impedance of the receiver side circuit.

In the equivalent circuit,  $v_{in}$  is a trapezoidal-wave voltage signal and is decomposed to different frequency components by Fourier series as

$$v_{in}(t) = \frac{V_{in}}{2} + \sum_{n=1,3,5\dots}^{+\infty} \frac{\sin(n\pi f_o t_d)}{n\pi f_o t_d} \frac{2V_{in}}{n\pi} \sin(2n\pi f_o t). \quad (4.12)$$

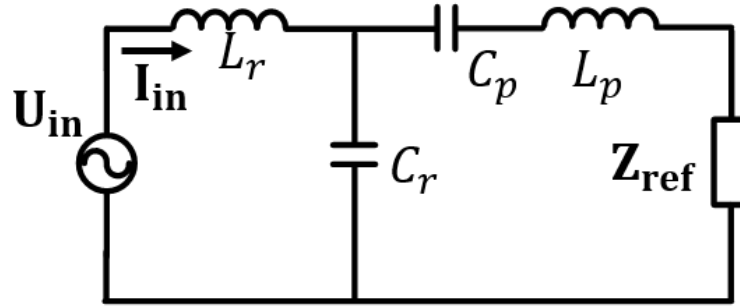


**Fig. 4-7. Equivalent circuit of the LCCL-LC converter with secondary side circuit reflected to primary side.**

If the input current component at each frequency is calculated correspondingly,  $I_{off}$  is the sum of the instant value of each component at  $t = T/2$ . To better visualize this process, the decomposition of the input current is shown in Fig. 4-8. The input current ( $i_{in}$ ) is decomposed to its fundamental component ( $i_f$ ) and harmonics component ( $i_h$ ). Furthermore, the fundamental component is decomposed to two parts: sine ( $i_{f\_sin}$ ) and cosine ( $i_{f\_cos}$ ). The sine part is in phase with the input voltage and impacts the active power transfer of the system. On the contrary, the cosine part has a  $90^\circ$  phase difference with the input voltage and impacts the reactive power flowing in the system. As illustrated by Fig. 4-8,  $i_{f\_sin}$  equals zero at  $t = T/2$  and does not contribute to  $I_{off}$ , however,  $i_{f\_cos}$  equals its amplitude at that time instant and contributes to  $I_{off}$  when the input impedance is inductive. Also, the harmonics component of the input current contributes to  $I_{off}$  and must be considered carefully.

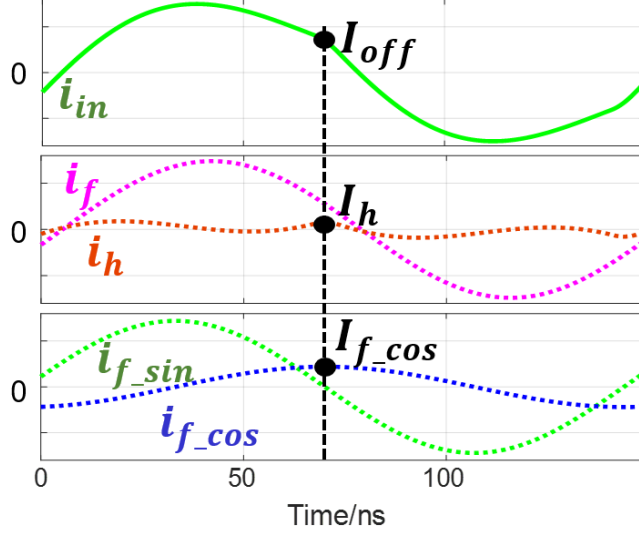


**Fig. 4-8. Decomposition of the input current waveform in time domain.**

With the equivalent circuit in Fig. 4-3, the KVL equation in the receiver loop is derived as

$$j\omega_o M \mathbf{I}_p + \mathbf{I}_s \left[ j\omega_o L_s + \frac{1}{j\omega_o C_s} + (R_{eq} // \frac{1}{j\omega_o C_{eq}}) \right] = 0. \quad (4.13)$$

Then, the reflected impedance of the receiver circuit  $\mathbf{Z}_{ref}$  at the fundamental frequency is calculated as

$$\mathbf{Z}_{ref} = \frac{j\omega_o M \mathbf{I}_s}{\mathbf{I}_p} = \frac{\omega_o^2 M^2}{R_{eq}} (1 + j\omega_o C_{eq} R_{eq}). \quad (4.14)$$

According to the equivalent circuit in Fig. 4-7, the complex input impedance at the fundamental frequency is derived as

$$\mathbf{Z}_f = \frac{L_r}{C_r} / \left[ \mathbf{Z}_{ref} + j(\omega_o L_p - \frac{1}{\omega_o C_p} - \frac{1}{\omega_o C_r}) \right]. \quad (4.15)$$

The fundamental component of the input current in phasor domain ( $\mathbf{I}_f$ ) is then calculated by the fundamental component input voltage ( $\mathbf{V}_f$ ) divided by the input impedance

$$\mathbf{I}_f = \frac{\mathbf{V}_f}{\mathbf{Z}_f} = \frac{\mathbf{V}_f}{L_r / C_r} \frac{\omega_o^2 M^2}{R_{eq}} - j \frac{\mathbf{V}_f}{L_r / C_r} \left( \frac{1}{\omega_o C_p} + \frac{1}{\omega_o C_r} - \omega_o L_p - \omega_o^3 M^2 C_{eq} \right), \quad (4.16)$$

where  $\mathbf{V}_f = \frac{\sin(\pi f_o t_d)}{\pi f_o t_d} \frac{2V_{in}}{\pi} \angle 0^\circ$ . In (4.16), there are two terms: the first term represents  $i_{f\_sin}$ ,

which is in phase with  $\mathbf{V}_f$ , and the second term represents  $i_{f\_cos}$ . As previously mentioned, only  $i_{f\_cos}$  contributes  $I_{off}$ , and its amplitude is derived as

$$I_{f\_cos} = \frac{\sin(\pi f_o t_d)}{\pi f_o t_d} \frac{2V_{in}}{\pi} \frac{1}{\omega_o L_r} \left( 1 - \frac{\omega_o L_p - 1 / \omega_o C_p + \omega_o^3 M^2 C_{eq}}{\omega_o L_r} \right). \quad (4.17)$$

The high order harmonics of input current in the LCCL-LC converter are actually trapped in the  $L_r, C_r$  loop, due to the low pass filter characteristics of the LC filter comprising of  $L_r$  and  $C_r$ . Similar to the fundamental component, the high order harmonics in phasor domain ( $\mathbf{I}_h$ ) are calculated as

$$\mathbf{I}_h = \sum_{n=3,5,\dots}^{+\infty} \frac{\mathbf{V}_{h\_n}}{\mathbf{Z}_h} = \sum_{n=3,5,\dots}^{+\infty} \frac{\mathbf{V}_{h\_n}}{jn\omega_o L_r + 1 / jn\omega_o C_r}. \quad (4.18)$$

where  $\mathbf{V}_{h\_n} = \frac{\sin(n\pi f_o t_d)}{n\pi f_o t_d} \frac{2V_{in}}{n\pi} \angle 0^\circ$ .

At  $t = T/2$ , the harmonics components are at its peak value due to the  $90^\circ$  phase delay with the input voltage, and the instant value ( $I_h$ ) is derived as

$$I_h = \sum_{n=3,5,7,\dots}^{+\infty} \frac{\sin(n\pi f_o t_d)}{n\pi f_o t_d} \frac{2V_{in}}{n\pi} \frac{1}{\omega_o L_r (n-1/n)}. \quad (4.19)$$

There is no direct closed form analytical solution for (4.19). Therefore, MATLAB software is utilized to calculate the harmonics up to 101<sup>st</sup> component. With a reasonable dead-time range (2~15ns) in 6.78 MHz system, the total high order harmonics can be approximated as

$$I_h \approx 0.2 \times \frac{\sin(\pi f_o t_d)}{\pi f_o t_d} \frac{2V_{in}}{\pi} \frac{1}{\omega_o L_r}. \quad (4.20)$$

Then, the total turn off current  $I_{off}$ , is the sum of  $I_{f\_cos}$  and  $I_h$ :

$$I_{off} = I_{f\_cos} + I_h \approx \frac{\sin(\pi f_o t_d)}{\pi f_o t_d} \frac{2V_{in}}{\pi} \frac{1}{\omega_o L_r} \left( 1.2 - \frac{\omega_o L_p - 1/\omega_o C_p + \omega_o^3 M^2 C_{eq}}{\omega_o L_r} \right). \quad (4.21)$$

In (4.21), the turn off current is not only related to the value of  $C_p$ , but also the equivalent capacitance ( $C_{eq}$ ) caused by the rectifier bridge. As illustrated by (4.6),  $C_{eq}$  is a function of the coupling and load condition, which makes the ZVS condition complicated. To demonstrate the quantitative impact of  $C_p$  and  $C_{eq}$  on the turnoff current, an example 6.78MHz LCCL-LC converter for charging a smartphone device is designed. The specification of the example system is shown in Table 4.1.

TABLE 4.1 SPECIFICATIONS OF THE WPT SYSTEM

Specifications	Symbol	Practical Value
Input voltage	$V_{in}$	24V
Output voltage range	$V_o$	10~20V
Output power	$P_o$	5W
Switching frequency	$f_o$	6.78MHz
Transmitter coil self-inductance	$L_p$	3.09uH
Transmitter coil resistance	$R_p$	0.6Ω
Receiver coil self-inductance	$L_s$	4.7uH
Receiver coil resistance	$R_s$	0.6Ω
Coupling coefficient range	$k$	0.12~0.25

According to (4.11), the output voltage of the LCCL-LC circuit at  $f_o$  is proportional to  $k$ . A commercial Li-Ion battery charging chip, such as the TI BQ25703, can be cascaded after the resonant converter to charge the battery with a certain profile [69]. The typical input voltage range of the charging chip is 4~24V. To reduce the conduction loss of the rectifier, a higher output voltage and lower current are preferred; therefore, the output voltage of the LCCL-LC converter is designed as 10~20V. The value of  $L_r$  is designed to output 10V at the worst coupling case ( $k = 0.12$ ):

$$L_r = \frac{k_{\min} \sqrt{L_p L_s} V_{in}}{2V_{o\min}} = 549nH . \quad (4.22)$$

With  $L_r$  determined, the values of  $C_r$  and  $C_s$  are calculated according to (4.7). In summary, the designed values for the passive components in the LCCL-LC converter are listed in Table III. In the receiver circuit, four discrete DFSL130 diodes are adopted for the rectification, due to their small conduction voltage drop. After the rectifier bridge, a simple resistor is manually adjusted to maintain the output power.

TABLE 4.2 PASSIVE COMPONENT VALUES IN THE LCCL-LC CONVERTER

Component	$L_r$	$C_r$	$C_s$
Practical value	549nH	980pF	118pF

With the specifications in Table II and Table III, the turn off current in different coupling coefficient and output power conditions under  $C_p = 160pF$ , is shown in Fig. 4-9. As shown in Fig. 4-9,  $I_{off}$  reduces when the coupling coefficient ( $k$ ) increases. An increase of coupling coefficient leads to large reflected impedance, so the impact of  $C_{eq}$  increases and the turn off current reduces, according to (4.21). On the other hand,  $C_{eq}$  decreases as the output power decreases, due to the increase of the load resistance, according to (4.6). Regarding this, the turn off current increases as the output power decreases, according to (4.21). In summary, the worst case for the turn off current is the strong coupling and heavy load case. Therefore,  $C_p$  should be designed to achieve enough turn off current to achieve ZVS at the worst case.

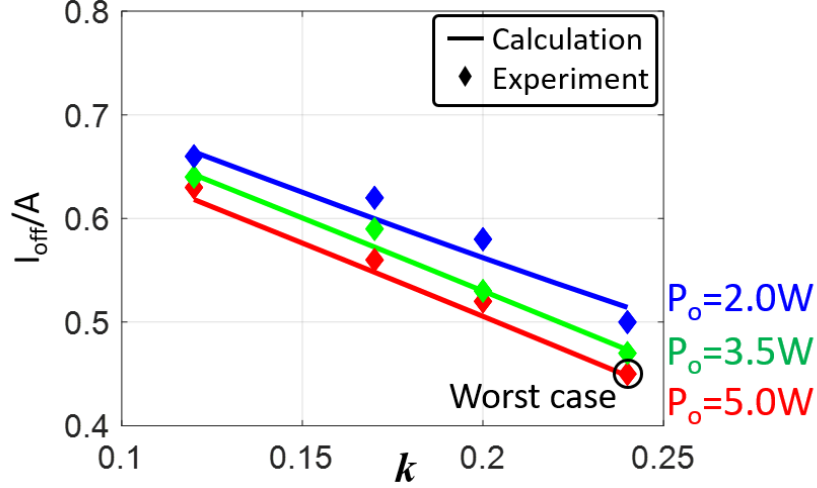


Fig. 4-9. Turn off current of the designed system under different coupling coefficient and output power information.

### 4.3.3 Considering effect of the dead-time period

To realize ZVS, the turn off current must be able to fully discharge the equivalent junction capacitor ( $C_{oss}$ ) of the switching devices during the dead-time period ( $t_d$ ):

$$Q = \int_{(T-t_d)/2}^{(T+t_d)/2} i_{off}(t) dt \geq 2C_{oss} V_{in}. \quad (4.23)$$

The turn off current changes during  $t_d$ , and the previously calculated  $I_{off}$  is the instant value at  $t = T/2$ . To calculate  $i_{off}(t)$ , the simplified equivalent circuit during  $t_d$  is derived in . Since the voltage of  $C_r$  does not change much during  $t_d$ , as shown in Fig. 6,  $C_r$  is replaced by a voltage source  $V_{cr}$ . The fundamental component of the voltage of  $C_r$  in phasor domain is calculated as

$$\mathbf{V}_{cr} = \frac{\mathbf{V}_f}{j\omega_o L_r} \left( j\omega_o L_p + \frac{1}{j\omega_o C_p} + \frac{\pi^2 \omega_o^2 M^2}{8R} \right). \quad (4.24)$$

Then, the instant value of  $v_{cr}$  at  $t = T/2$  is approximated by

$$V_{cr} \approx \left( \frac{1}{2} + \frac{\pi \omega_o M^2}{4RL_r} \right) V_{in}. \quad (4.25)$$

The second order differential KVL equations in the equivalent circuit shown in Fig. 4-10, with the initial conditions, are derived as the following:

$$\begin{aligned}
 2L_r C_{oss} \frac{d^2 u(t)}{dt} - u(t) - V_{cr} &= 0; \\
 2C_{oss} \frac{du(t)}{dt} &= -i_{off}(t); \\
 u(0) = V_{in}; \quad 2C_{oss} \frac{du(t_d/2)}{dt} &= -I_{off}.
 \end{aligned}
 \tag{4.26}$$

Therefore,  $i_{off}(t)$  is solved, and the discharge during  $t_d$  is calculated as

$$i_{off}(t) = I_1 \sin(\omega_1 t + \varphi), \tag{4.27}$$

$$Q = 2C_{oss} (V_{in} - V_{cr}) - \frac{I_1}{\omega_1} \cos(\omega_1 t_d + \varphi). \tag{4.28}$$

where 
$$I_1 = \frac{[I_{off} - \sin(\omega_1 t_d / 2)(V_{in} - V_{cr})\omega_1 C_{oss}]^2}{\cos^2(\omega_2 t_d / 2)} + (V_{in} - V_{cr})^2 \omega_1^2 C_{oss}^2, \quad \varphi = \arccos \frac{V_{in} - V_{cr}}{I_1} \omega_1 C_{oss},$$

$$\omega_1 = \frac{1}{\sqrt{2L_r C_{oss}}}.$$

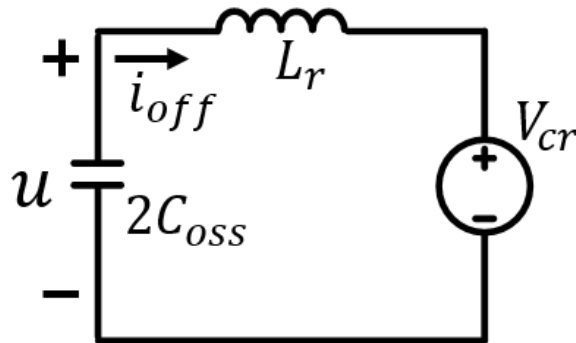


**Fig. 4-10. Simplified equivalent circuit for the discharging of the junction cap of the switching devices during the dead-time period.**

To realize ZVS with minimum circulating energy,  $C_p$  is tuned so that the discharge ( $Q$ ) during  $t_d$  is the same as the charge stored in the output junction capacitor ( $C_{oss}$ ) of the primary devices for

the worst case. Due to the complicity of the model, an iterative program to solve  $C_p$  is built in MATLAB.

#### 4.4 ZVS Analysis in Multiple Transmitter Coils Case

In a multiple transmitter coils system, the ZVS condition is more complicated, due to the uncertain circulating energy incurred by different coils. To simplify the analysis, the ZVS condition with two transmitter coils is first evaluated in this paper. As shown in Fig. 4-11, when a wearable device receiver stands on the base of the charging bowl, coil 1a and coil 2a should be excited to provide the energy. It's worth noting the orientation and position of the receiver coil in Fig. 4-11 is just an example and different transmitter coils should be excited according to positioning of the receiver coil.

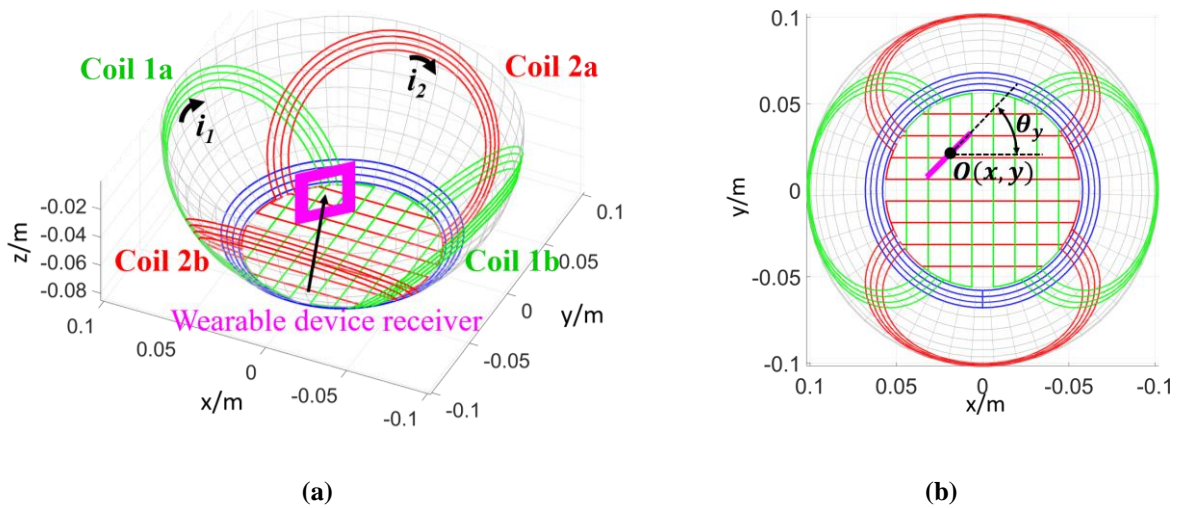


**Fig. 4-11. Transmitter coils and a receiver coil in an omnidirectional WPT system. (a). 3D view. (b). Top View.**

The LCCL-LC circuit diagram with two transmitter coils is shown in Fig. 4-12. Herein,  $L_{p1}$ ,  $L_{p2}$ , and  $L_s$  are the self-inductances of the two transmitter coils and receiver coil respectively.  $M_1$

and  $M_2$ , are the mutual inductance between the receiver coil and two transmitter coils;  $M_3$  is the mutual inductance between the two transmitter coils. The decoupled circuit model at the fundamental frequency is shown in Fig. 4-13.

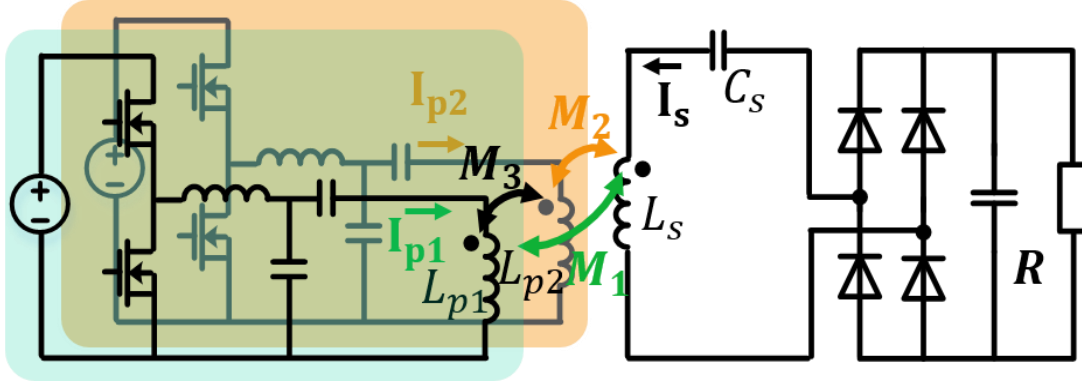


Fig. 4-12. Two phase LCCL-LC circuit diagram with two transmitter coils.

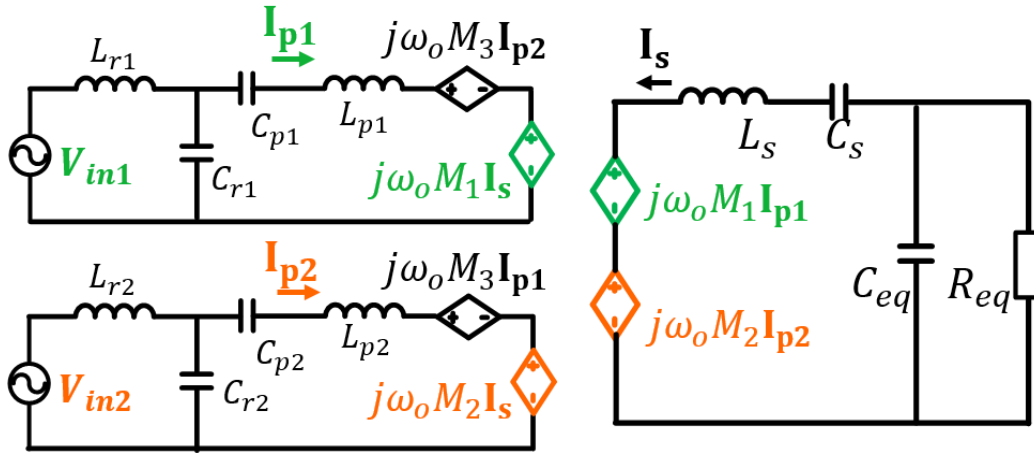


Fig. 4-13. Equivalent decoupled circuit at fundamental frequency.

The input voltage of each channel ( $V_{in1}$ ,  $V_{in2}$ ) is controlled by the front buck stages to implement transmitter coil excitation current amplitude modulation. The KVL equation of the receiver circuit in phasor domain is derived as

$$j\omega_o M_1 \mathbf{I}_{p1} + j\omega_o M_2 \mathbf{I}_{p2} + (j\omega_o L_s + \frac{1}{j\omega_o C_s} + R_{eq} // \frac{1}{j\omega_o C_{eq}}) \mathbf{I}_s = 0. \quad (4.29)$$

At the resonant frequency of  $L_s$  and  $C_s$ , the receiver coil current is solved as follows:

$$\mathbf{I}_s = \frac{-(j\omega_o M_1 \mathbf{I}_{p1} + j\omega_o M_2 \mathbf{I}_{p2})(1 + j\omega_o R_{eq} C_{eq})}{R_{eq}}. \quad (4.30)$$

The complex reflected impedance in each transmitter circuit is derived as follows:

$$\mathbf{Z}_{\text{ref1}} = \frac{j\omega_o M_1 \mathbf{I}_s + j\omega_o M_3 \mathbf{I}_{p2}}{\mathbf{I}_{p1}}, \quad (4.31)$$

$$\mathbf{Z}_{\text{ref2}} = \frac{j\omega_o M_2 \mathbf{I}_s + j\omega_o M_3 \mathbf{I}_{p1}}{\mathbf{I}_{p2}}. \quad (4.32)$$

Substituting (4.30) in (4.31) and (4.32), the reflected impedance in each transmitter circuit is solved as follows:

$$\mathbf{Z}_{\text{ref1}} = \left( \frac{\omega_o^2 M_1^2}{R_{eq}} + \frac{\omega_o^2 M_1 M_2}{R_{eq}} \frac{\mathbf{I}_{p2}}{\mathbf{I}_{p1}} \right) (1 + j\omega_o R_{eq} C_{eq}) + j\omega_o M_3 \frac{\mathbf{I}_{p2}}{\mathbf{I}_{p1}}, \quad (4.33)$$

$$\mathbf{Z}_{\text{ref2}} = \left( \frac{\omega_o^2 M_2^2}{R_{eq}} + \frac{\omega_o^2 M_1 M_2}{R_{eq}} \frac{\mathbf{I}_{p1}}{\mathbf{I}_{p2}} \right) (1 + j\omega_o R_{eq} C_{eq}) + j\omega_o M_3 \frac{\mathbf{I}_{p1}}{\mathbf{I}_{p2}}. \quad (4.34)$$

After obtaining the reflected impedance for each transmitter circuit, the transmitter circuits are decoupled from one another. Then, the process to calculate the turn off current for the one transmitter and one receiver case can be applied for the two transmitter case. The final turn-off current equations for each transmitter circuit are derived as

$$I_{\text{off1}} \approx \frac{\sin(\pi f_o t_d)}{\pi f_o t_d} \frac{2V_{in1}}{\pi} \frac{1}{\omega_o L_{r1}} \left( 1.2 - \frac{\omega_o L_{p1} - 1/\omega_o C_{p1} + \text{Im}(\mathbf{Z}_{\text{ref1}})}{\omega_o L_{r1}} \right), \quad (4.35)$$

$$I_{\text{off2}} \approx \frac{\sin(\pi f_o t_d)}{\pi f_o t_d} \frac{2V_{in2}}{\pi} \frac{1}{\omega_o L_{r2}} \left( 1.2 - \frac{\omega_o L_{p2} - 1/\omega_o C_{p2} + \text{Im}(\mathbf{Z}_{\text{ref2}})}{\omega_o L_{r2}} \right). \quad (4.36)$$

where:  $\text{Im}(\mathbf{Z}_{\text{ref1,2}})$  are the imaginary part of the complex reflected impedance for two transmitter circuits:

$$\text{Im}(\mathbf{Z}_{\text{ref1}}) = C_{eq} \omega_o^3 M_1^2 + \text{Im} \left[ \left( \frac{\omega_o^2 M_1 M_2}{R_{eq}} + jC_{eq} \omega_o^3 M_1 M_2 + j\omega_o M_3 \right) \frac{\mathbf{I}_{p2}}{\mathbf{I}_{p1}} \right],$$

$$\text{Im}(\mathbf{Z}_{\text{ref2}}) = C_{eq} \omega_o^3 M_2^2 + \text{Im}\left[\left(\frac{\omega_o^2 M_1 M_2}{R_{eq}} + jC_{eq} \omega_o^3 M_1 M_2 + j\omega_o M_3\right) \frac{\mathbf{I}_{p1}}{\mathbf{I}_{p2}}\right].$$

It is worth noting, that the turn off current equation becomes much more complicated compared to the one transmitter coil case. The excitation current of two transmitter coils has a significant impact on the turn off current. In [44] and [45], the coil excitation current control methods are divided into two categories: there is phase difference among ( $i_1, i_2$ ); there is no phase difference among ( $i_1, i_2$ ).

$$\text{Method I: } \mathbf{I}_{p1} = I_m \angle 0^\circ, \mathbf{I}_{p2} = I_m \angle 90^\circ \quad (4.37)$$

$$\text{Method II: } \mathbf{I}_{p1} = m_1 I_m \angle 0^\circ, \mathbf{I}_{p2} = m_2 I_m \angle 0^\circ. \quad (4.38)$$

where  $m_1, m_2$  are variables to control field direction.

Substituting (4.37) and (4.38) in (4.33) and (4.34), the imaginary part of the complex reflected impedance is derived as follows:

Method I:

$$\text{Im}(\mathbf{Z}_{\text{ref1}}) = C_{eq} \omega_o^3 M_1^2 + \frac{\omega_o^2 M_1 M_2}{R_{eq}} \quad (4.39)$$

$$\text{Im}(\mathbf{Z}_{\text{ref1}}) = C_{eq} \omega_o^3 M_1^2 + \frac{\omega_o^2 M_1 M_2}{R_{eq}} \quad (4.40)$$

Method II:

$$\text{Im}(\mathbf{Z}_{\text{ref1}}) = C_{eq} \omega_o^3 M_1^2 + (C_{eq} \omega_o^3 M_1 M_2 + \omega_o M_3) \frac{m_2}{m_1} \quad (4.41)$$

$$\text{Im}(\mathbf{Z}_{\text{ref2}}) = C_{eq} \omega_o^3 M_2^2 + (C_{eq} \omega_o^3 M_1 M_2 + \omega_o M_3) \frac{m_1}{m_2} \quad (4.42)$$

Therefore, the turn off current for each channel is different for two current control methods. To achieve the ZVS operation in the operation range, the worst case for designing  $C_p$  is identified

as follows.

#### 4.4.1 Identify the worst case for method I

The key advantage of an omnidirectional WPT system is that it can deal with angular misalignment of the receiver. The top view of a receiver device standing on the base of the bowl is shown in Fig. 4-11(b). Herein, the yaw rotation angle is defined as  $\theta_y$ . The mutual inductance between the receiver coil and two transmitter coils coil 1 set and coil 2 set for different  $\theta_y$  is shown in Fig. 4-14.

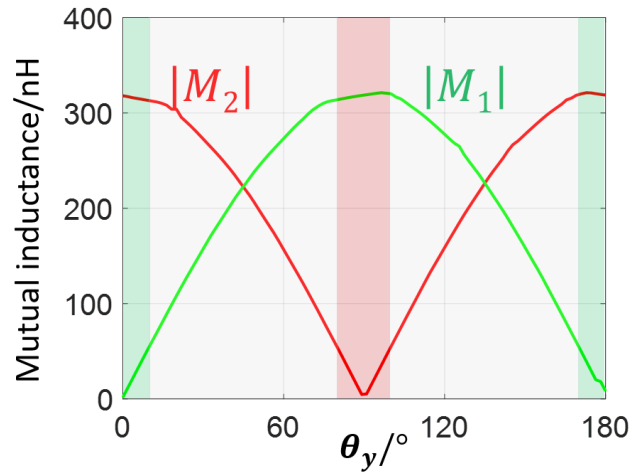


**Fig. 4-14. Mutual inductance between receiver coil and transmitter coils 1a, coil 2a ( $M_1$ ,  $M_2$ ) versus under different yaw angle  $\theta_y$  of the receiver.**

With the mutual inductance curve in , the turn-off current for the two transmitter coils circuit versus the different yaw rotating angles for modulation method I is shown in Fig. 4-15. There is large fluctuation in the turn-off current curve, and the turn off current is smallest when  $\text{Im}(Z_{\text{ref}1,2})$  is at the maximum value, based on (4.35) and (4.36). Similar to the one transmitter coil case, the worst case is the strong coupling and heavy load case, according to (4.39), (4.40). The coupling condition refers to the product of  $M_1$  and  $M_2$  in the two transmitter coils case.

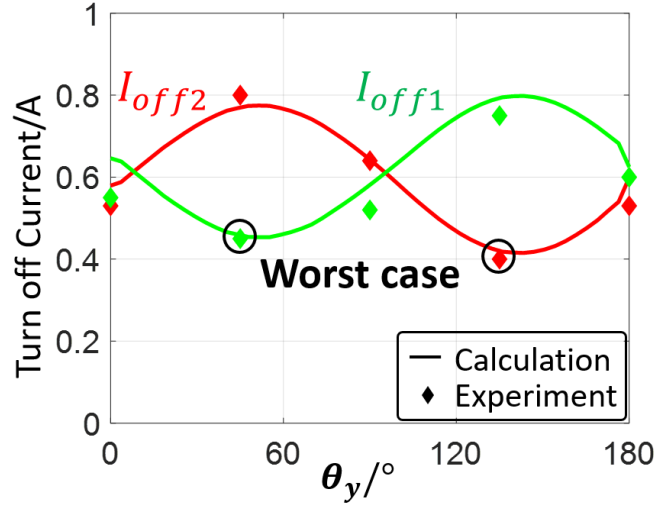


Fig. 4-15. Turn off current of two transmitter circuits versus different yaw angle  $\theta_y$  of the wearable receiver for modulation method I.

#### 4.4.2 Identify the worst case for method II

As for the current control method II, a buck stage is added before the LCCL-LC converter, to modulate the input voltage of the LCCL-LC converter and control the amplitude of the excitation current. According to [70]-[72], the best ratio between the amplitude of two transmitter coils current under the assumption that two coils' equivalent resistance is the same is

$$\frac{m_1}{m_2} = \frac{M_1}{M_2}. \quad (4.43)$$

Therefore, the input voltage of each channel in our system is controlled by the front buck as

$$V_{in1} = \frac{M_1}{M_1 + M_2} \cdot V_{in}; \quad (4.44)$$

$$V_{in2} = \frac{M_2}{M_1 + M_2} V_{in}. \quad (4.45)$$

Substituting (4.43) in (4.44) and (4.45), the reflected impedance for ( $Z_{ref1,2}$ ) method II is simplified as follows:

$$\text{Im}(\mathbf{Z}_{\text{ref1}}) = C_{eq} \omega_o^3 (M_1^2 + M_2^2) + \omega_o M_3 \frac{M_2}{M_1} \quad (4.46)$$

$$\text{Im}(\mathbf{Z}_{\text{ref2}}) = C_{eq} \omega_o^3 (M_1^2 + M_2^2) + \omega_o M_3 \frac{M_1}{M_2} \quad (4.47)$$

As shown in (4.46) and (4.47), the mutual inductance between two transmitter coils ( $M_3$ ) also impacts the reflected impedance and influences the turn off current for each channel. In a multiple coils system, it is desired to reduce the circulating energy between different transmitter coils as much as possible. In other words, the mutual inductance between different transmitter coils should be minimized in the coil design stage. In this sense, the mutual inductance  $M_3 = 0$  case is first studied. With the mutual inductance curve in Fig. 4-14, the turn off current of the two channel circuit is shown in Fig. 4-16.

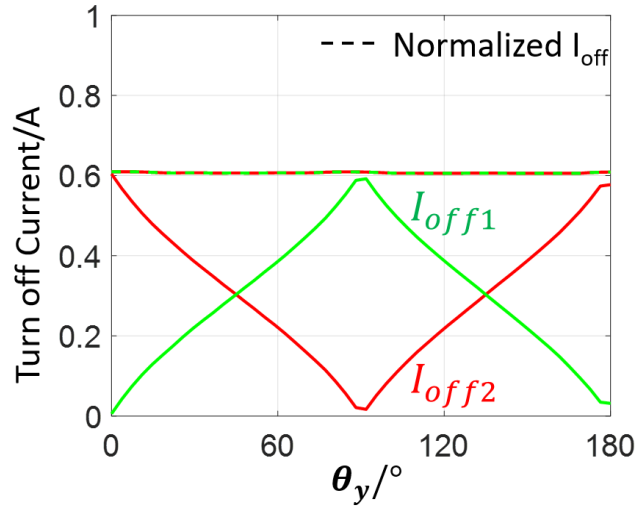


**Fig. 4-16. Turn off current of two transmitter circuits versus different yaw angle  $\theta_y$  of the receiver for modulation method II when  $M_3 = 0$ .**

As shown in Fig. 4-16, turn off current  $I_{off1}$  reduces as  $M_1$  decreases. Meanwhile, the input voltage  $V_{in1}$  also reduces according to (4.44). With a smaller  $V_{in1}$ , the required turn off current to achieve ZVS operation also reduced proportionally. To better compare the turn off current between

the two modulation methods, the turn off current for each channel in method II is normalized to full input voltage level. The normalization algorithm is as follows:

$$I_{off1\_N} = I_{off1} \cdot \frac{V_{in}}{V_{in1}}, \quad I_{off2\_N} = I_{off2} \cdot \frac{V_{in}}{V_{in2}}. \quad (4.48)$$

The normalized turn off current curve versus  $\theta_y$  for each channel in method II for the  $M_3 = 0$  case is shown as a dashed line in Fig. 4-16. Compared with method I, the turn off current does not significantly change, which is beneficial for the ZVS operation. The physical reason behind this is the reflected impedance  $Z_{ref1,2}$  in method II is determined by  $M_1^2 + M_2^2$  according to (40) and (41). In a general omnidirectional WPT system,  $M_1^2 + M_2^2$  does not significantly change as the angle misalignment changes. Therefore, the normalized turn off current does not change much in method II. However, the reflected impedance  $Z_{ref1,2}$  in method I is related to  $M_1M_2$ , which has large fluctuation for different angle misalignment.

The transmitter coils in an omnidirectional WPT system are normally symmetric structure, as reported in [44]-[47]. The mutual inductance between different transmitter coils in such a system is zero theoretically. However, there might be some weak crossing coupling due to the coil fabrication and terminations. Beside, in some multiple transmitter coils systems, such as systems reported in [56], [70], [73], the cross-coupling between different transmitter coils also exists. Therefore, the impact of the cross-coupling on the turn-off current is evaluated as follows.

The normalized turn off current curve for each channel is shown in Fig. 4-17 when the cross-coupling coefficient between two transmitter coils is 0.05. Here, there is a large glitch in the turn off current curve for channel 2. The glitch exists at the red shaded zone, as plotted in Fig. 4-17. At

the red zone,  $M_2$  is small, and the cross-coupling term  $\omega_o M_3 \frac{M_1}{M_2}$  will dominate the reflected

impedance  $Z_{ref2}$ , according to (4.47). This results in large fluctuation in the turn off current curve. The ZVS operation can no longer be achieved when the turnoff current is negative. A similar phenomenon is also observed for the channel 1 case when  $M_1$  is very small. In summary, the cross-coupling between different transmitter coils deteriorates the ZVS condition when the ratio  $M_2/M_1$  or  $M_1/M_2$  is very large.

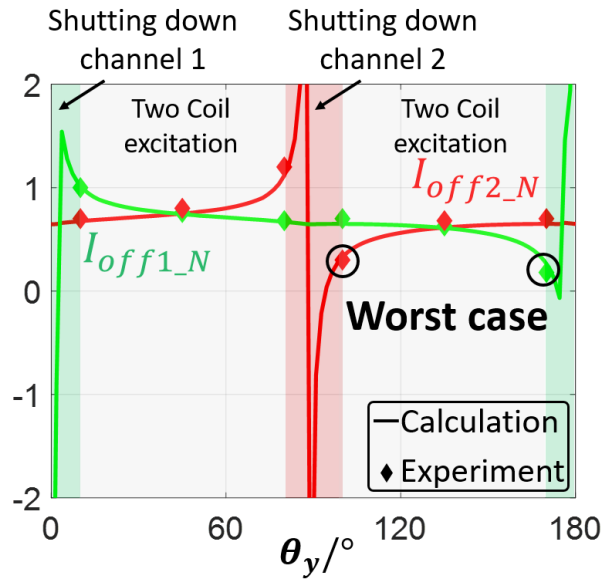


Fig. 4-17. Normalized turn off current of two transmitter circuits versus different yaw angle  $\theta_y$  of the receiver for modulation method II when  $M_3 \neq 0$  ( $k_3 = 0.05$ ).

To solve this issue, channel 2 can be shut down in the glitch zone. The energy provided by channel 2 in the glitch zone is much smaller compared to channel 1, since  $M_2$  is much smaller than  $M_1$ . Meanwhile, the operation efficiency also improves by shutting down one channel. As an example, the boundary condition to shut down channel 2 is  $M_1/M_2 > 5$ . Similarly, the boundary condition to shut down channel 1 is  $M_2/M_1 > 5$ . With this channel shading mechanism, the worst case for the turn off current is at the boundary condition, as shown in Fig. 4-17. Therefore,  $C_{p1}$  should be designed to achieve enough turn off current to achieve ZVS for channel 1 when  $M_2/M_1$

= 5. Similarly,  $C_{p2}$  should be designed to achieve enough turn off current to achieve ZVS for channel 2 when  $M_1/M_2 = 5$ .

## 4.5 Experiment Verification

In this section, an omnidirectional wireless charging bowl is built, as shown in Fig. 4-18. In the experimental setup, there are two channel LCCL-LC circuits to drive the transmitter coils (coil 1a and coil 2a), separately. The TI microcontroller TMS320C28346 demo board is used to give the PWM signals to the half bridge of the LCCL-LC circuit, and the system is powered by an Agilent E3631A DC power source.

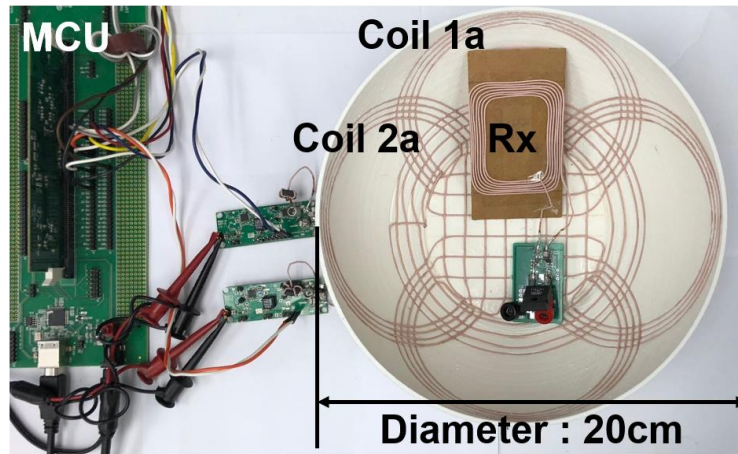


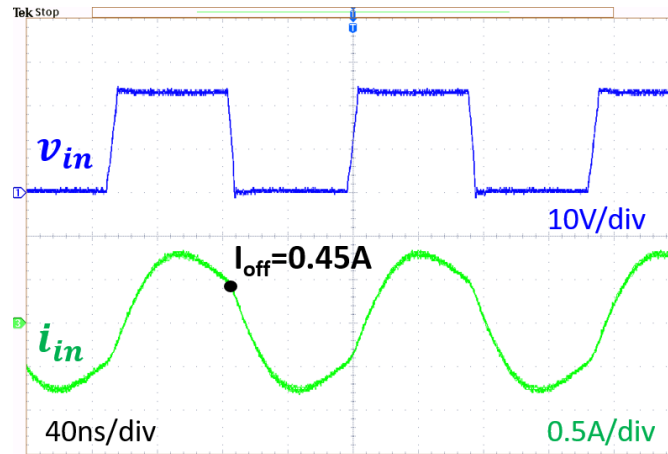
Fig. 4-18. The physical setup of the omnidirectional WPT system.

### 4.5.1 One transmitter coil case

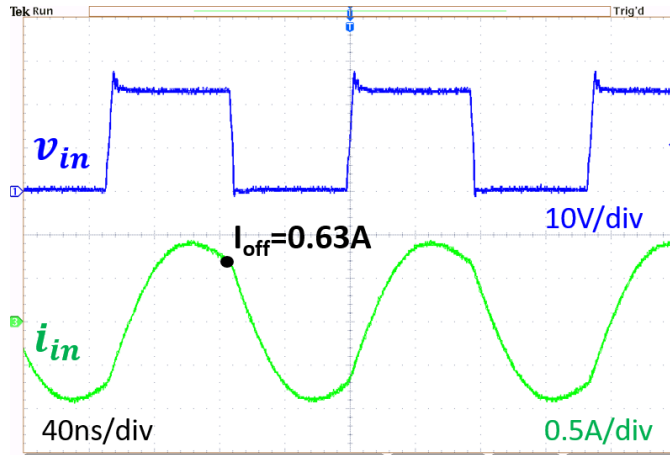
As shown in Fig. 4-18, when a smart phone receiver device rests on the side face, coil 1a should be enabled to charge the receiver. The system is simplified to the case of one transmitter and one receiver, and the specifications for this case are shown in Table II and Table III. In the transmitter side, the EPC8004 is adopted to operate at 6.78 MHz. The dead-time period is set as 5

ns. In the receiver circuit, four discrete DFSL130 diodes are adopted for the rectification due to their small conduction voltage drop. After the rectifier bridge, a simple resistor is manually adjusted to emulate the function of the battery charging chip.

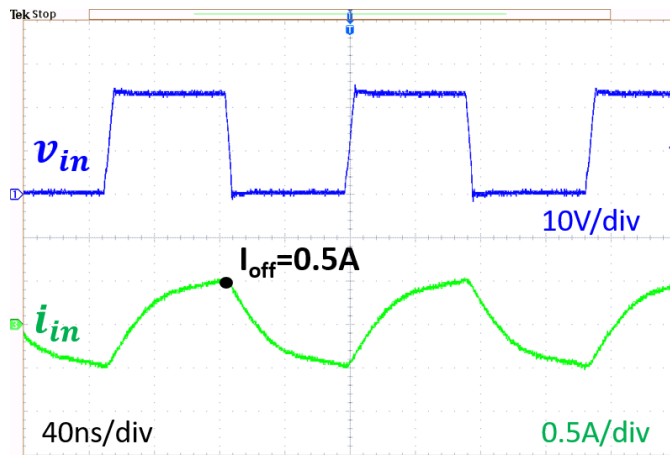
To realize ZVS operation at the worst case (strong coupling and heavy load),  $C_p$  is calculated as 160pF, based on the analytical model in section 4.3. The turn off current measurement results under different conditions are shown in Fig. 4-9. The measurement result matches very well with the analytical model. The switching node voltage and current waveform under three example conditions are shown in Fig. 4-19. The turn off current is smallest at the strong coupling and heavy load case, which verifies the worst-case analysis. With the proposed designed methodology, the turn off current is high enough for different conditions, and ZVS operation is guaranteed, as illustrated by Fig. 4-19. The efficiency of the LCCL-LC circuit under different conditions is shown in Fig. 4-20.



(a)



(b)



(c)

Fig. 4-19. Experimental switching node voltage and current waveform for one transmitter (coil 1a excited) and one receiver case (smart phone receiver Rx). (a).  $k = 0.24$ ,  $P_o = 5W$  (Worst case). (b).  $k = 0.12$ ,  $P_o = 5W$ . (c).  $k = 0.24$ ,  $P_o = 2W$ .

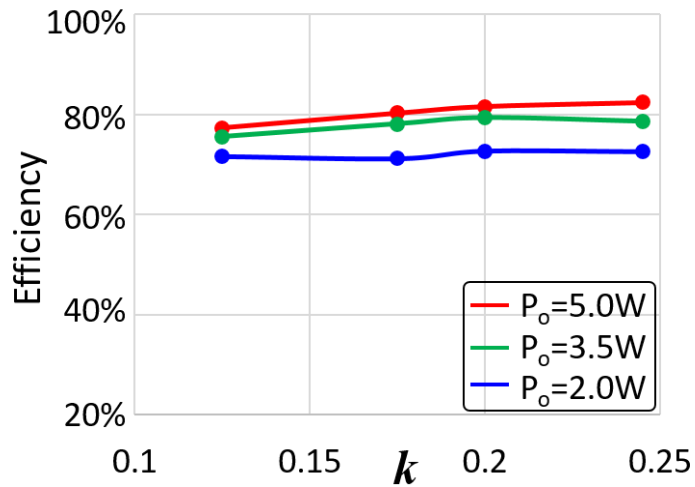


Fig. 4-20. Efficiency of the LCCL-LC converter in one transmitter case.

To evaluate the impact of ZVS operation on the system efficiency, two experimental cases are conducted under one transmitter coil case. Herein, the coupling coefficient between transmitter coil 1a and receiver coil is 0.2. The output power is 5W. In the first case,  $C_p$  in the LCCL-LC circuit is designed to achieve enough turn off current to achieve ZVS operation at the worst case as demonstrated in the manuscript. The switching node voltage and current waveforms under this case are shown in Fig. 4-21(a). Then  $C_p$  in the LCCL-LC circuit is purposely increase to 180pF so that the input impedance of the LCCL-LC circuit is resistive. And the turn off current reduces to zero and ZVS operation cannot be achieved any more. The switching node voltage and current waveforms under this case are shown in Fig. 4-21(b). The system efficiency under ZVS case and non-ZVS case are 80.5% and 77.2% separately. Regarding this, the ZVS operation can improve the converter system efficiency. The loss breakdown under these two cases is provided in Fig. 4-22.

As demonstrated by Fig. 4-22, the device switching loss reduces a lot with the ZVS operation. On the other hand, the device conduction loss and inductor loss increases a little bit in ZVS case since there is extra circulation energy to realize ZVS. As for coil conduction loss and rectifier, there is no difference between two cases. The transmitter coil current in the LCCL-LC circuit is determined by the input voltage and the impedance of  $L_r$ . Therefore, the transmitter coil current is the same for two cases. The secondary coil loss and rectifier loss is determined by the output voltage and output power level, which is the same for both cases. Therefore, the ZVS operation increases the system efficiency by 3.2% by reducing the switching loss with a small sacrifice of the device conduction loss and compensation inductor loss.

Other than improving system efficiency, the ZVS operation also reduces the circuit noise level. As demonstrated in Fig. 4-21, the  $dv/dt$  during switching transient for non-ZVS case is much larger

than the ZVS case. This high  $dv/dt$  will induce high noise in the circuit, causing large interference to other circuit.

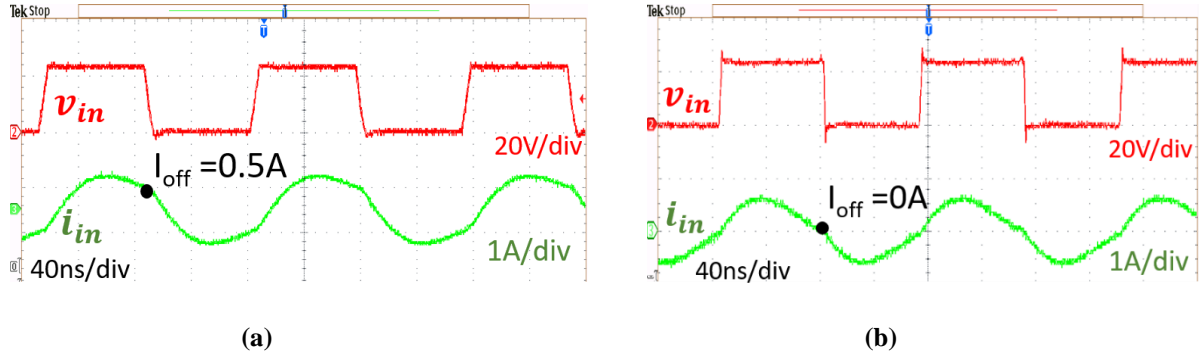


Fig. 4-21. Experimental switching node voltage and current waveforms under  $k = 0.2$ ,  $P_o = 5W$ . (a) ZVS case. (b). Non ZVS case.

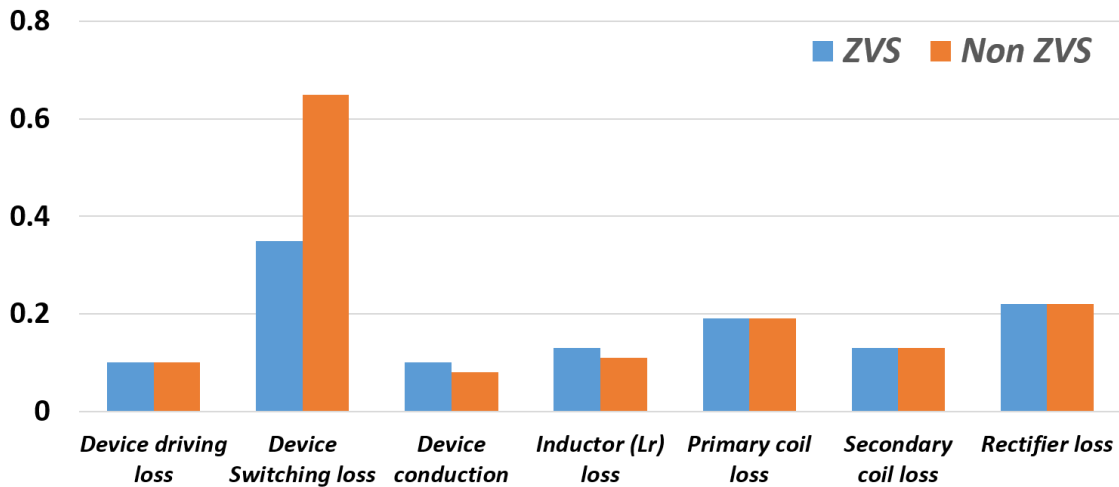


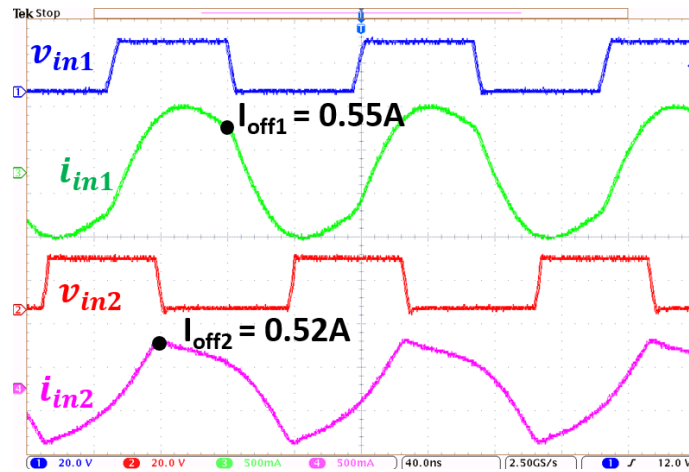
Fig. 4-22. Loss breakdown of the converter for ZVS and non-ZVS case. (Unit: W)

#### 4.5.2 Two transmitter coil case

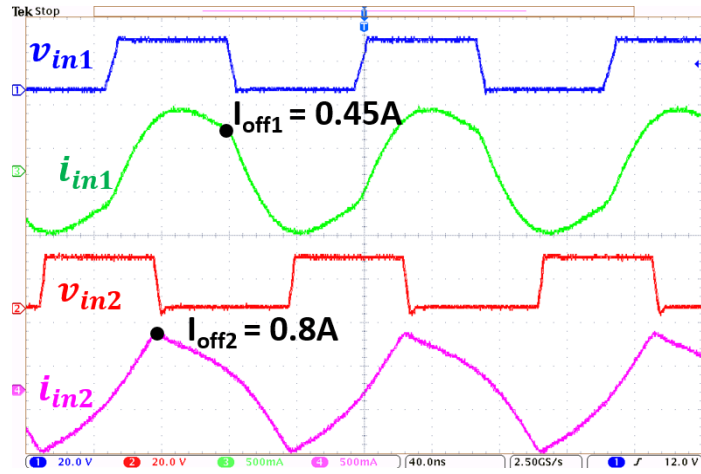
As shown in Fig. 4-11, when a wearable device like smart watch device stands on the base of the charging bowl, coil 1a and coil 2a should be excited to provide the energy. In the test, a  $35 \times 35$  mm square receiver coil ( $7.5 \mu H$ ,  $1.1 \Omega$ ), which is different from previous smart phone receiver coil, is fabricated to emulate an Apple watch receiver in the charging bowl. The two transmitter

circuits to drive coil 1a and coil 2a are exactly the same, and the circuit specifications are shown in Table II and Table III.

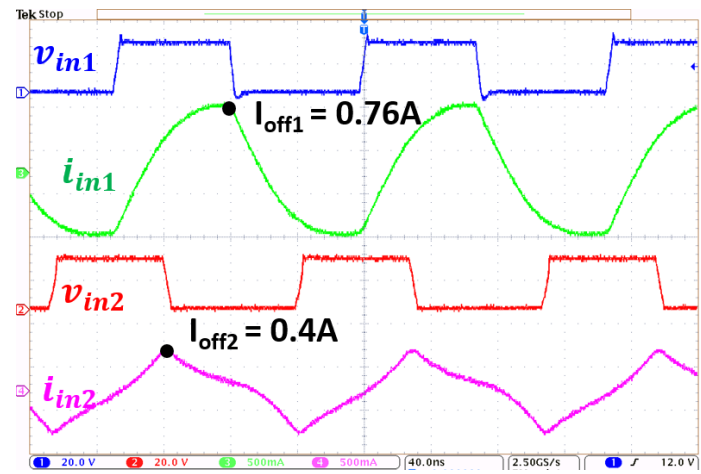
As mentioned by Section 4.4, the turn off current is related to the transmitter coil excitation current. As for current control method I,  $C_{p1}$  and  $C_{p2}$  are calculated as 155 pF to achieve ZVS operation at the worst case based on (4.23) and (4.36). The turn off current measurement results under different yaw angles of the receiver are shown in Fig. 4-15. The measurement results match with the calculation results very well. The experimental switching node voltage and current waveform for two channel LCCL-LC circuits, under three example receiver angles, are shown in Fig. 4-23. As demonstrated by Fig. 4-23, the turn off current is high enough to achieve ZVS operation for different orientations of the receiver devices.



(a)



(b)

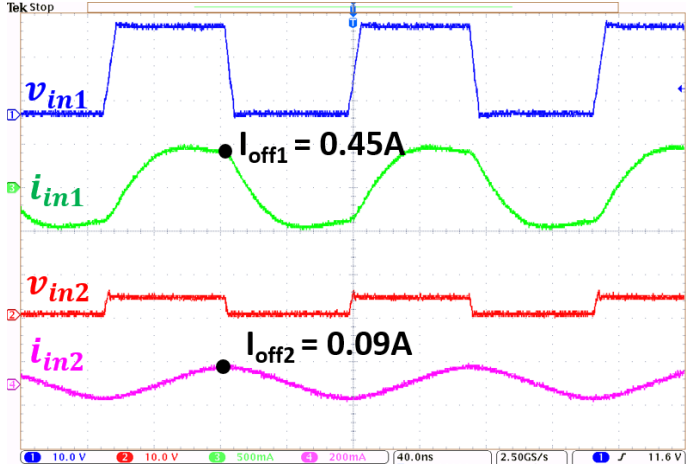


(c)

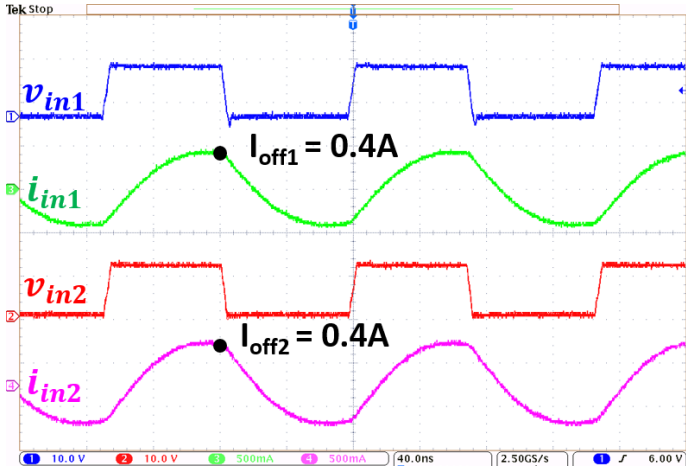
Fig. 4-23. Experimental switching node voltage and current waveform for two transmitter and one receiver case with excitation current method I. (a).  $\theta_\gamma = 0^\circ$ ,  $P_o = 2.5W$ . (b).  $\theta_\gamma = 45^\circ$ ,  $P_o = 2.5W$  (worst case for channel I). (c).  $\theta_\gamma = 135^\circ$ ,  $P_o = 2.5W$  (worst case for channel II).

As for excitation current method II,  $C_{p1}$  and  $C_{p2}$  are calculated as 162 pF to achieve ZVS operation at the worst case based on (4.23) and (4.36). Then, the normalized turn off current measurement results under different yaw angles of the receiver are shown in Fig. 4-17. The measurement results match with the calculation results very well. The experimental switching node voltage and current waveform for two channel LCCL-LC circuits, under three example receiver

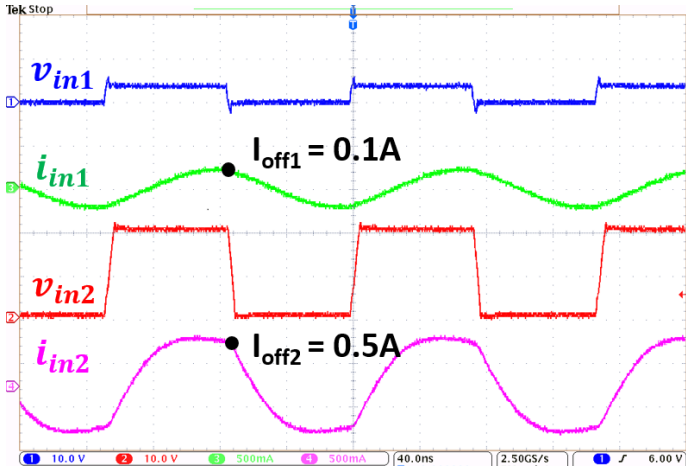
angles, are shown in Fig. 4-24. As demonstrated by Fig. 4-24, the turn off current is high enough to achieve ZVS operation for the different cases.



(a)



(b)



(c)

**Fig. 4-24. Experimental switching node voltage and current waveform for two transmitter and one receiver case with excitation current method II. (a).  $\theta_y = 100^\circ$ ,  $P_o = 2.5W$  ( $M_1/M_2 = 5$ , worst case for channel II). (b).  $\theta_y = 135^\circ$ ,  $P_o = 2.5W$ . (c).  $\theta_y = 170^\circ$ ,  $P_o = 2.5W$  ( $M_2/M_1 = 5$ , worst case for channel I).**

With the proposed design methodology, ZVS operation is well achieved under different conditions. The system efficiency at 2.5 W, (defined as the load power divided by the input power of the dc input source), for two current control methods are shown in Fig. 4-25. The system efficiency in method II is better than method I. In method I, the input voltage of two channel LCCL-LC circuits is always 24 V and the rotating field is achieved by the phase difference between the two channels. However, the input voltage is adaptive according to the receiver's angle in method II. With lower input voltage, the switching loss and coil conduction loss in the transmitter side are smaller. Therefore, the system efficiency for method II is better.

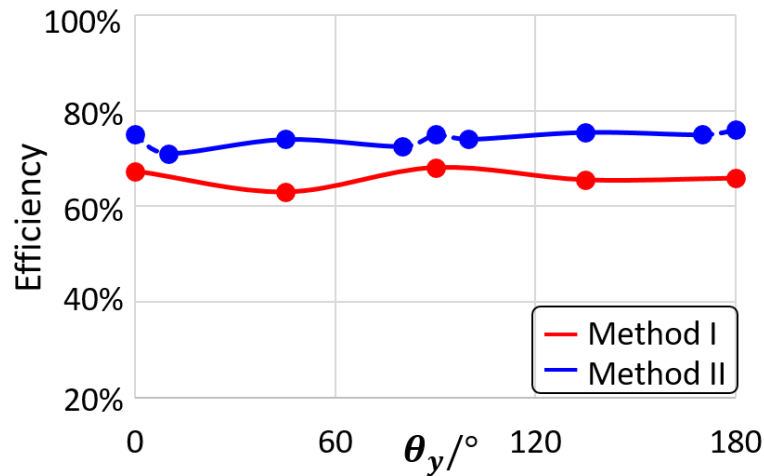


**Fig. 4-25. System efficiency versus different yaw angle of the receiver for two transmitter and one receiver case.**

## 4.6 Conclusion

In this chapter, an analytical model of the full bridge rectifier input impedance including the effect of diode junction charge, is built in a MHz system. After considering the rectifier reactance,

input impedance of the LCCL-LC circuit is dependent on the loading and coupling condition. The strong coupling, heavy load case is identified as the worst case for ZVS achievement. A passive component parameter design methodology is proposed to achieve ZVS operation at the worst case. Then, the ZVS analysis is extended to a two transmitter coils case. The worst case for different excitation current control methods is identified in the two transmitter coils case, and ZVS operation is guaranteed in different scenarios with the proposed design methodology. With the ZVS operation for primary switching devices, the total system efficiency of our system is in 62 % – 82 % [79].

# Chapter 5 Stray Field Reduction for Human Health

## 5.1 Introduction

Nowadays, there are two major wireless charging standards for consumer electronics applications, including the Qi standard and the AirFuel Standard [64], [81]. The Qi standard defines the system operation frequency from 100 ~ 205 kHz; however, the operation frequency of the AirFuel standard is selected at 6.78MHz. Herein, the proposed system is designed to operate at 6.78 MHz to have better spatial charging freedom based on the study in section 1.4. An important design issue of a wireless charging system with inductive coupling is the safety issue related to human exposure of electromagnetic fields (EMF). In a Qi charging system, the human exposure problems can be mitigated by a magnetic shield [64]. However, the effectiveness of a magnetic shield is not evaluated in a 6.78 MHz system in the existing literature.

In an omnidirectional wireless charging system, 3-dimensional transmitter coils structure is normally adopted [38]-[46]. The omnidirectional wireless charging bowl concept is proposed and implemented in previous chapter. However, it is very difficult to apply a shield layer to a curved surface with a half-sphere bowl structure. Regarding this, a square-shaped charging bowl concept is explored in this chapter. With square-shaped bowl fixture, it is much easier to attach the commercial shielding sheet in terms of the manufacturability. Other than that, it is also found that the coupling between a smart phone receiver device and transmitter coil can be enhanced with square-shaped bowl.

The impact of the available 6.78MHz magnetic shield on the field distribution of the square-shaped charging bowl is evaluated by the Finite Element Analysis (FEA) simulation in this chapter. Due to the available material technology, the permeability of the magnetic material at 6.78 MHz

is much lower than low frequency case. It is found that the stray field cannot comply with the human exposure regulations due to low permeability of the magnetic material. To further reduce the stray field, a double-layer shield structure is first utilized in a 3D charging setup. The shield consists of a magnetic layer and a conductive layer, and it was first proposed for a PCB transformer in [82]. However, the impact of different thickness and permeability/conductivity of each layer has not been discussed yet [83], [84]. In this paper, a comprehensive parametric analysis of the double layer shield is first disclosed.

In section 5.2, a square-shaped wireless charging bowl is introduced. Then the shielding study to reduce the stray field is conducted in section 5.3. Finally, a hardware is built with some commercial available double layer shield sheets to verify the effectiveness of the shield structure in section 5.4 and the power transfer efficiency with and without the double layer shield is compared.

## **5.2 A Square-shaped Wireless Charging Bowl**

To achieve the omnidirectional power transfer capability, a novel wireless charging bowl is proposed in chapter 2. The transmitter coils structure is shown Fig. 5-1. There are five coils: coils 1-4 are wound from the bottom to the side face of the bowl, and coil 5 is placed around the bottom of the bowl. In most situations, a planar device, such as a smart phone, is likely to lay on the side face of the bowl. To describe the positioning of the receiver device precisely,  $\theta_1$  and  $\theta_2$  are introduced in the top view and side view in Fig. 5-2. A typical receiver coil for a smart phone is adopted and the dimension of the receiver coil is 55 x 65 mm. The receiver coil's turns number is 6.  $\theta_1$  is defined as the angle between the center line of the receiver coil and the center line of transmitter coil 1 and  $\theta_2$  is defined as the angle between the receiver plane and the horizontal plane. Due to the symmetry among coils 1-4, coil 1 is selected to excite for charging the receiver device

when  $-45^\circ < \theta < 45^\circ$ ; coil 3 is selected to excite when  $45^\circ < \theta < 135^\circ$  and etc. The coupling coefficient ( $k$ ) between transmitter coil 1 and the receiver coil in different positioning is shown Fig. 5-3 ( $\theta < 0^\circ$  part is neglected due to the symmetry of coil 1). As illustrated in Fig. 5-3,  $k$  decreases a lot when  $\theta$  increases from  $0^\circ$  to  $45^\circ$ , which leads to small transfer energy and bad efficiency.

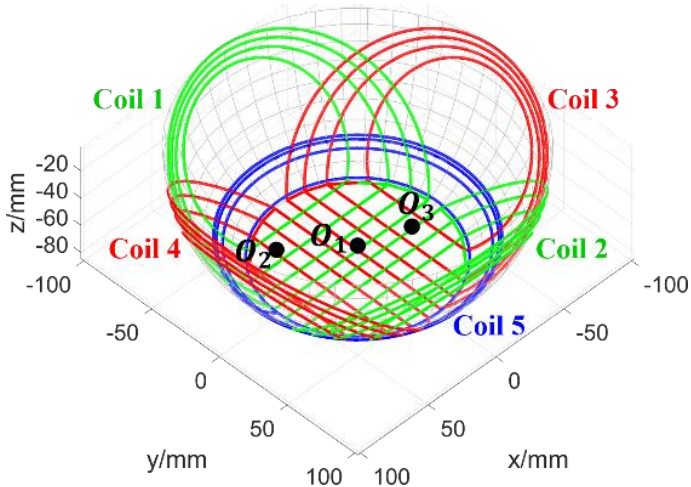


Fig. 5-1. The transmitter coils structure.

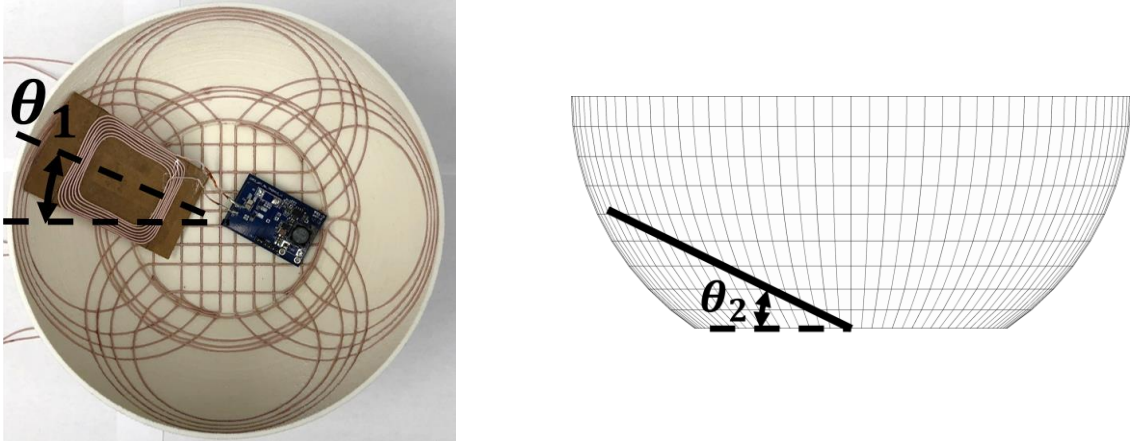
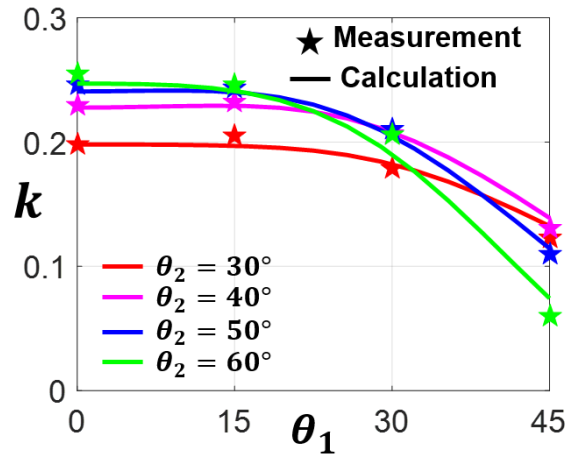
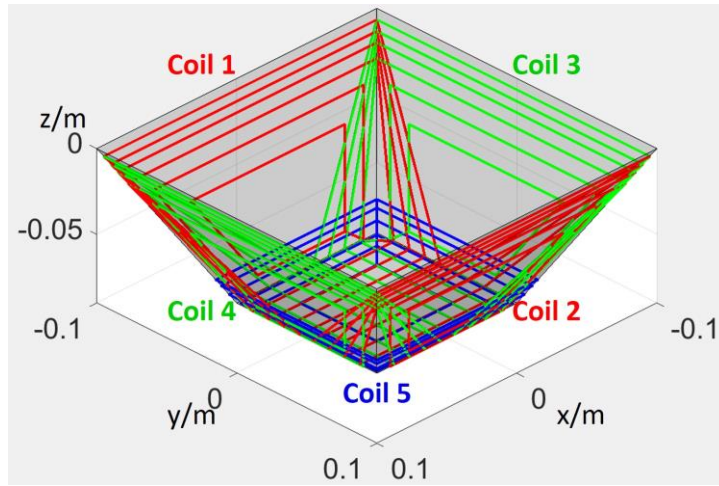


Fig. 5-2. Smart phone receiver positioning description parameter ( $\theta_1, \theta_2$ ).



**Fig. 5-3. Coupling coefficient ( $k$ ) between transmitter coil 1 and the receiver coil under different positioning of the receiver coil.**

To apply the shielding sheet to the charging bowl, a square-shaped charging bowl is proposed. The structure is shown in Fig. 5-4 and the operation principle is the same as previous sphere-shaped charging bowl. When a smart phone lay on the side face inside the bowl, side coil should be excited to provide the energy. The 3D sketch of side coil 1 and a typical receiver coil is shown in Fig. 5-5. The red line represents transmitter coil 1; the blue rectangle (55 x 65 mm) line represents a typical receiver coil for a smart phone, and the black rectangle (60 x 120 mm) represents the profile of the phone. Herein, the distance ( $d$ ) between the center line of receiver coil and the center line of transmitter coil 1 is used to describe the misalignment. The maximum misalignment between transmitter coil 1 and receiver coil is defined as  $d_{\max}$ . The coupling coefficient between transmitter coil 1 and the receiver coil in different positioning in the setup is shown in Fig. 5-6. As illustrated in Fig. 6,  $k$  is high even with some misalignment; therefore, a square-shaped transmitter coils structure can uniformly charge a planar device in the side face. Compared with the sphere charging bowl, the proposed square-shaped charging bowl is better in terms of charging smart phone device in the side face.



**Fig. 5-4. The proposed coils structure in a square-shaped charging bowl.**

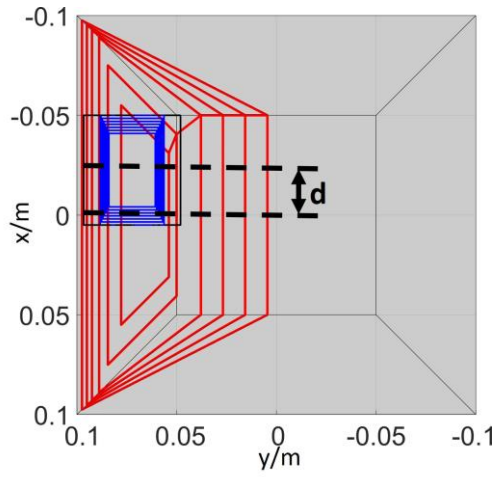


**Fig. 5-5. Receiver positioning index  $d$  definition.**

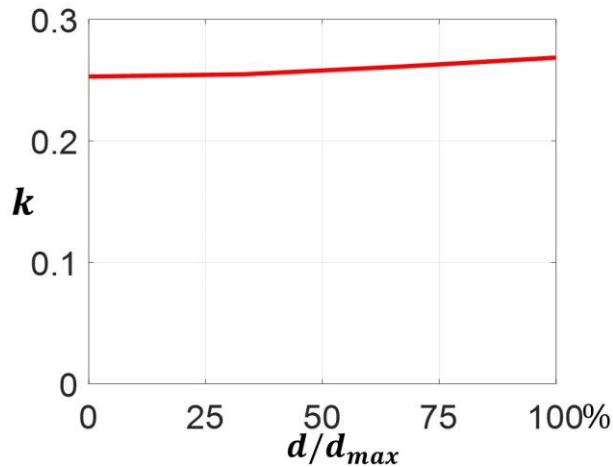


**Fig. 5-6. Coupling coefficient ( $k$ ) between transmitter coil 1 and the receiver coil under different positioning of the receiver coil.**

### 5.3 Shielding Study of the Wireless Charging Bowl

One big concern of an IPT system is the safety issue related to human exposure of electromagnetic fields (EMF). There are several guiding regulation documents to prevent established adverse health effects due to the EMF: 1). the ICNIRP Guidelines [85]; 2). IEEE standard C95.1-2005 [86]; 3). FCC part 1 [87]. The limits for maximum permissible exposure in FCC part 1 is shown in Table 5.1. In an IPT system, the magnetic field is the dominate EMF and the limits at 6.78MHz is  $H = 0.32$  A/m (or  $B = 0.4$  uT for the magnetic flux density in air) according to Table 5.1.

**TABLE 5.1 FCC PART 1 FIELD LIMINTATION**

Frequency range f (MHz)	Electric field strength(V/m)	Magnetic field strength (A/m)	Power Density(mW/cm <sup>2</sup> )
0.3-1.34	614	1.63	100
1.34-30	824/f	2.19/f	180/f <sup>2</sup>
30-300	27.5	0.073	0.2

A 3D FEA simulation software, ANSYS MAXWELL, is utilized to evaluate the magnetic field distribution of the charging bowl. The simulated field distribution in YZ plane (referring Fig. 5-4) is shown in Fig. 5-7 when coils 1-5 are excited with 0.6A 6.78MHz ac sinusoidal current. In Fig. 5-7, the amplitude of the magnetic field outside the charging bowl is stronger than 0.4uT. Therefore, stray field must be attenuated to comply with the FCC part 1.

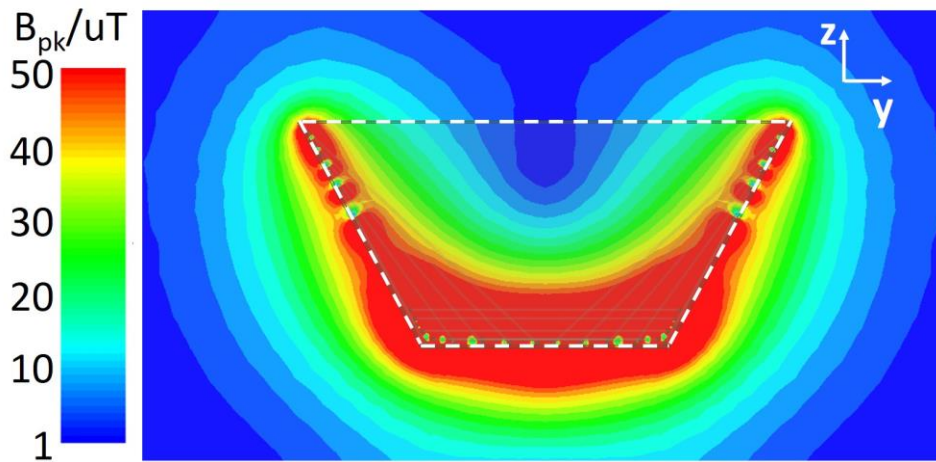


Fig. 5-7. Field distribution in YZ plane in the square-shaped charging bowl.

### 5.3.1 Single Layer Magnetic Shield

A ferromagnetic shield is widely used in a low frequency planar Qi charging system to reduce the stray field level and increase the coupling coefficient. However, this shield technique is not yet studied in a 6.78 MHz omnidirectional WPT system; therefore, it's evaluated carefully in this section. In the proposed 3D charging setup, the shield layer is wrapped around the charging bowl to confine the magnetic field. And the top shield cover is removable to allow receiver devices being dropped in the bowl by users.

The field distribution in YZ plane with a 0.3mm  $\mu_r = 100$  magnetic shield layer is shown in Fig. 5-8. To evaluate the impact of the shield layer quantitatively, the magnetic field strength along

$z = -0.05$  m line in YZ plane is demonstrated in Fig. 5-9. Herein, the magnetic field strength inside the bowl increases after applying the shield, but the stray field outside the bowl decreases. The field attenuation outside the bowl is related to the permeability of the shield layer. In Fig. 5-9, the field attenuation is not sensitive to the  $y$  coordinate since the field distribution curves for different permeability are almost in parallel with each other. In this sense, the field strength at one observation point  $(0, 0.12$  m,  $-0.05$  m) is plotted in Fig. 5-10 with different permeability and thicknesses of the shield layer.

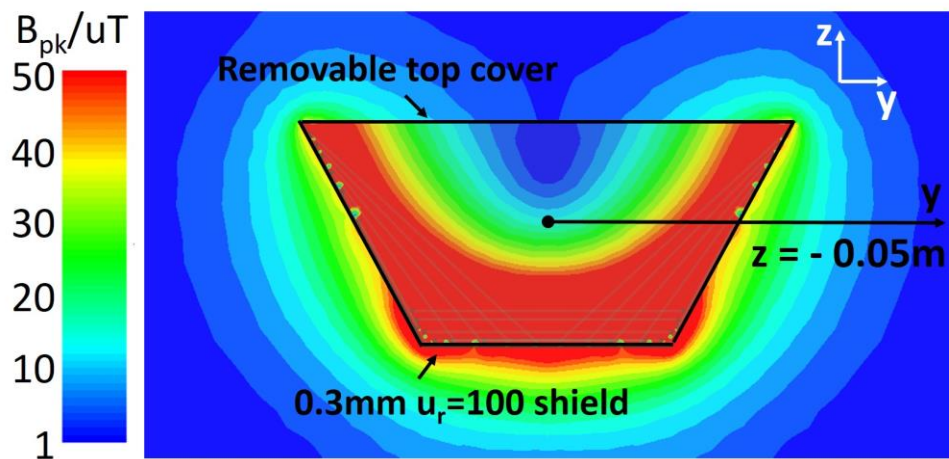


Fig. 5-8. Field distribution in YZ plane with single layer ferromagnetic shield.

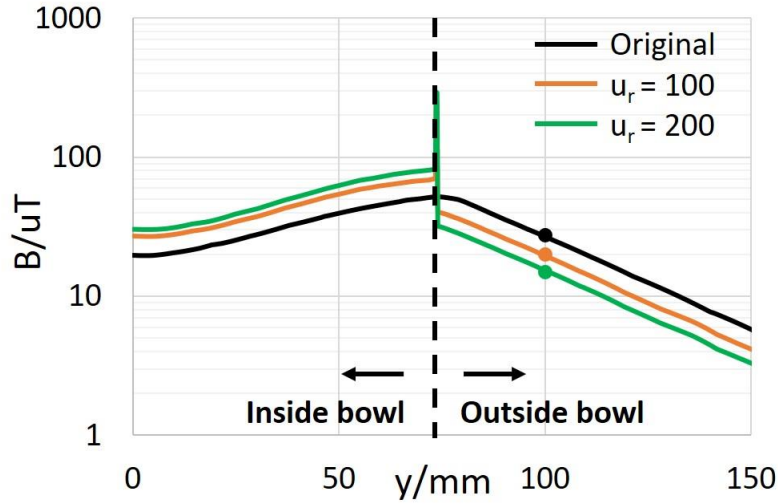


Fig. 5-9. Field distribution along  $z = -0.05\text{m}$  for different  $u_r$ .

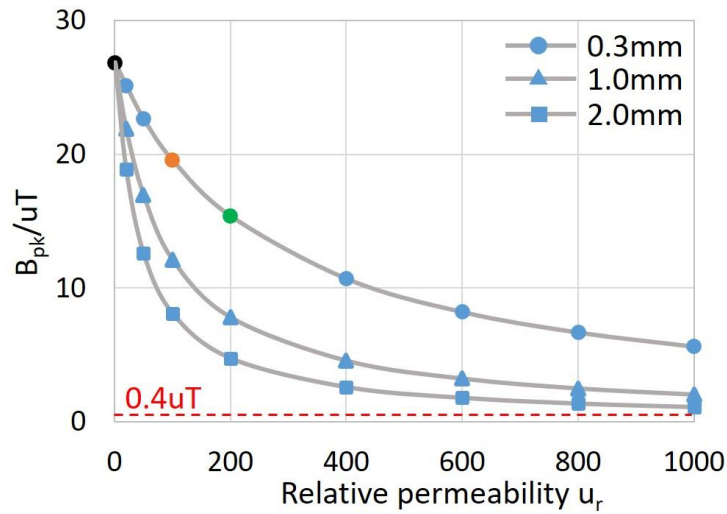


Fig. 5-10.  $B_{pk}$  at  $(0, 0.12\text{m}, -0.05\text{m})$  v.s. different  $u_r$  and thickness.

In Fig. 5-10, the magnetic field strength at the example point decreases when the relative permeability increases. However, there is diminishing return effect when permeability is high enough. This phenomenon is also valid when the thickness of the shield increases from 0.3mm to 2mm. Due to the diminishing returning effect, the stray field strength after applying the shield cannot comply with the FCC part 1. Meanwhile, the maximum  $u_r$  at 6.78MHz of the current ferrite

material with small core loss is around 180 (TDK FJ7 material), to the best of author's knowledge [88]. And the maximum thickness of the shield sheet available in the market is around 1mm. Regarding the limitations of current material technology, the stray field outside bowl cannot comply with the safe limits with this single layer magnetic shield.

### **5.3.2 Double Layer Shield Structure**

To further reduce the stray field outside the charging bowl, a conductive layer is added outside the magnetic layer. The field distribution in YZ plane with a 0.3mm  $\mu_r = 180$  ferrite layer and a 0.1mm copper layer is shown in Fig. 5-11. Herein, the stray field is greatly reduced outside the charging bowl and it is below the safe limit (0.4uT). According to the simulation, the conduction loss in the copper layer is only 1mW. The magnetic field at the boundary of the ferrite layer and the copper layer would come back to coils through the ferrite layer since it cannot penetrate a good conductor. The conductor layer behaves like a wall to the magnetic field; however the ferrite layer is like a highway to the magnetic field. When the magnetic field traverse to the boundary of the conductive layer and ferrite layer, the magnetic field tends to go through ferrite layer due to low reluctance. This leads to very small residual field in the conductive layer and therefore the eddy current loss is small. Regarding this, the double layer shield structure is promising for a 6.78MHz omnidirectional charging system. Thus far, the parametric study and the impact of the each layer is lacked in current literature; therefore, it is discussed in detail in this section.

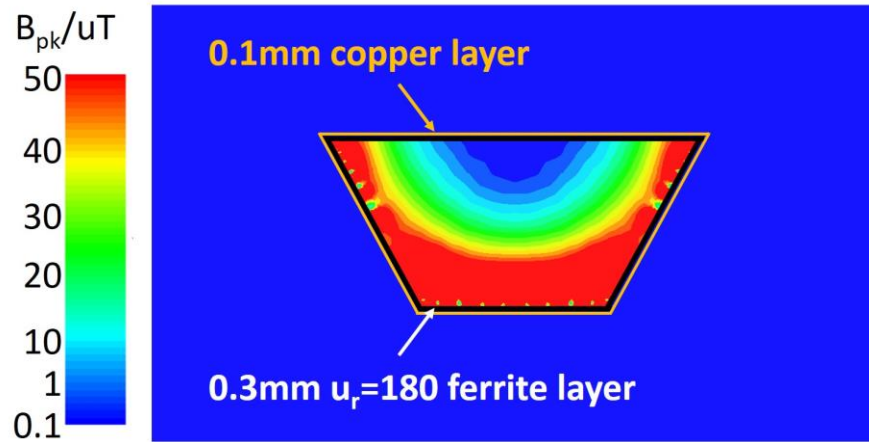


**Fig. 5-11. Field distribution in YZ plane with a double layer shield.**

At first, the impact of material types and thickness of the conductive layer on the field distribution is studied. The field  $s$  along  $z = -0.05\text{m}$  line for different cases is shown in Fig. 5-12. Herein, the green curve represents field distribution with only one ferrite layer shield; the other four curves represents field distribution after adding a conductive layer. By adding a conductive layer, the stray field outside the bowl decreases dramatically while the field inside the bowl only drops a little bit. This is important to the power transfer capability since the magnetic field inside the bowl is used to transfer energy. In Fig. 5-12, the field distribution with the copper and aluminum layer are almost the same. The conductivity of copper is  $5.8 \times 10^7 \text{S/m}$  while that of aluminum is  $3.8 \times 10^7 \text{S/m}$ . Both of them are considered as good conductor and therefore the attenuation are similar. Meanwhile, the effectiveness of the conductive layer on the field distribution is also not sensitive to the thickness as demonstrated in Fig. 5-12. The stray field outside the bowl is well below  $0.4\text{uT}$  for  $0.1\text{mm}$  case and  $0.3\text{mm}$  case.

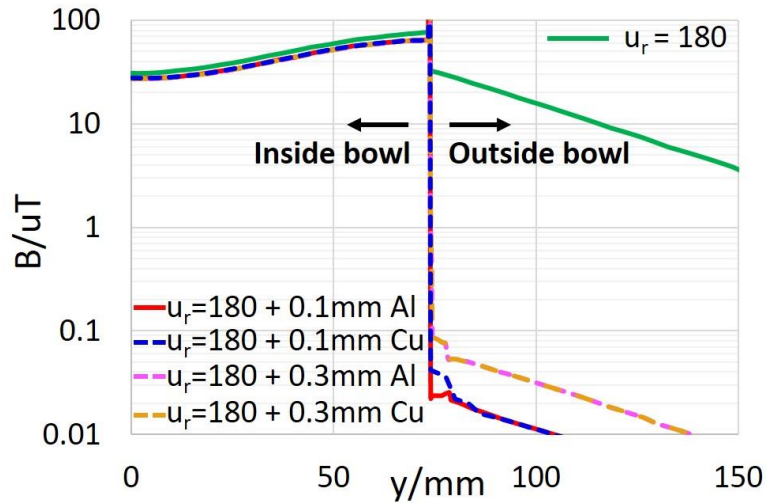


**Fig. 5-12. The impact of conductive layer on field distribution.**

Secondly, the impact of  $u_r$  and thickness of the ferrite layer on the field distribution is evaluated. The field strength along  $z = -0.05\text{m}$  line for the 0.3mm ferrite layer with different  $u_r$  is shown in Fig. 5-13. Herein, the black curve is the original case without any shield; the orange curve represents field distribution with only one aluminum layer. If there is no ferrite layer, the magnetic field inside and outside bowl both decreases dramatically and the power transfer capability suffers a lot. By adding a ferrite layer, the field inside the bowl is improved significantly while the stray field outside the bowl decreases slightly. And the field enhancement inside is dependent on  $u_r$  and is not sensitive to the  $y$  coordinate since the field distribution curves for different  $u_r$  are almost in parallel with each other. In this sense, the field strength at an example point  $(0, 0.05\text{ m}, -0.05\text{ m})$  versus  $u_r$  and thickness of the ferrite layer is plotted in Fig. 5-14. As shown in Fig. 5-14,  $u_r$  must be higher than a certain value to guarantee the field inside the bowl doesn't decrease and this critical value is related to the thickness of the ferrite layer. Therefore, the

permeability and thickness of the ferrite layer in the double layer must be selected carefully to make sure the field inside the bowl doesn't decrease.

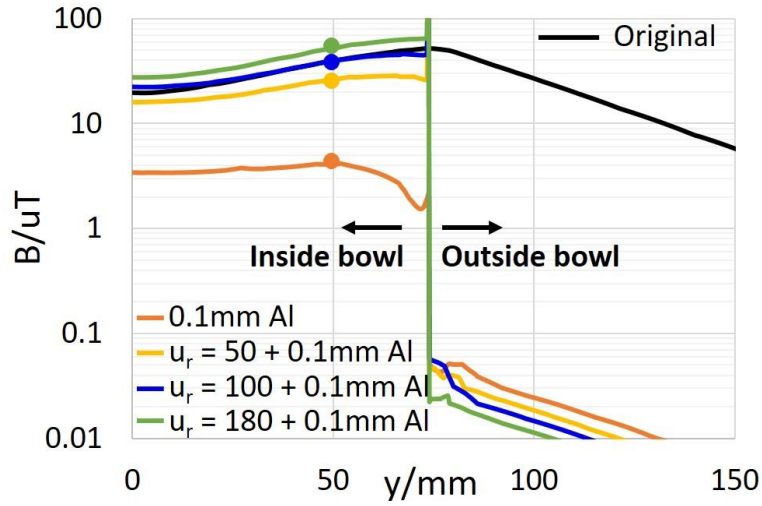


Fig. 5-13. The impact of the ferrite layer on field distribution.

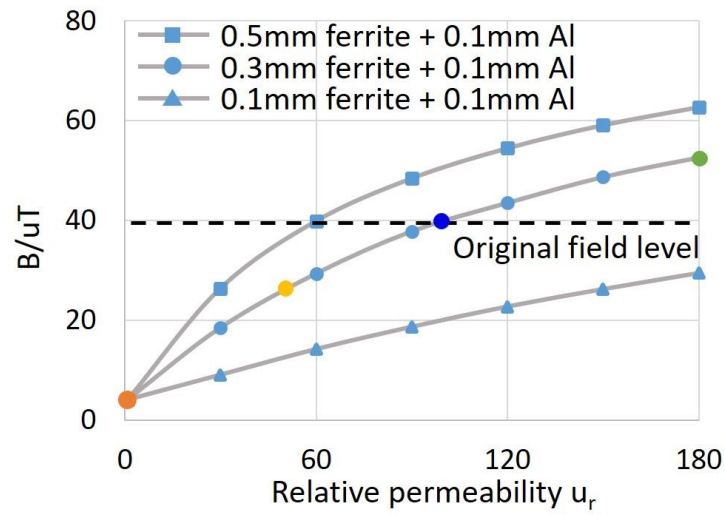
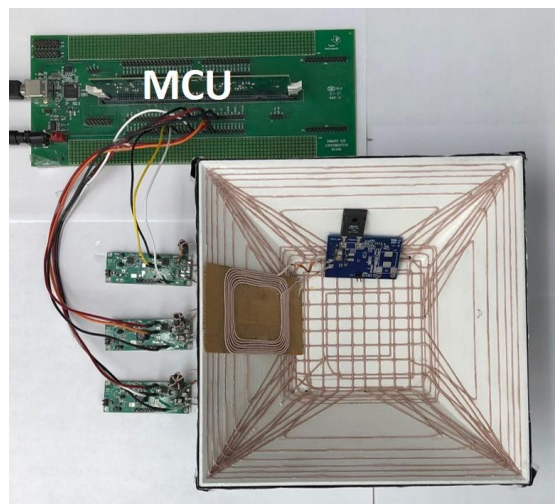


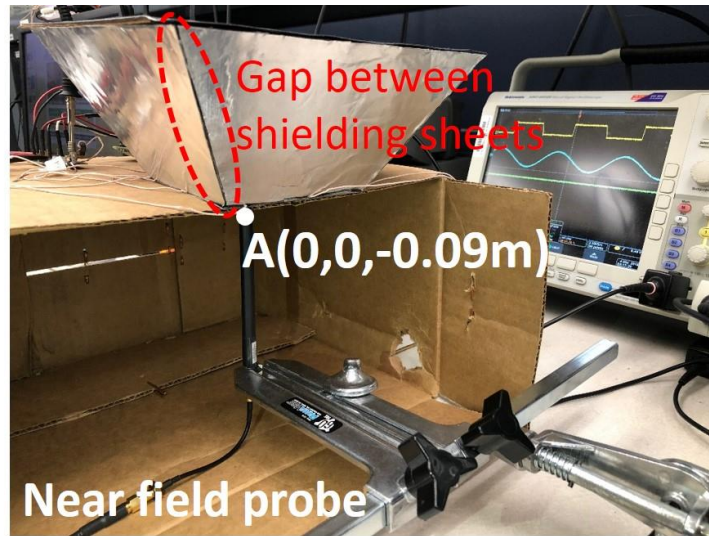
Fig. 5-14.  $B_{pk}$  at (0, 0.05m, -0.05m) v.s. different  $u_r$  and thickness.

## 5.4 Experimental Verification

To verify the effectiveness of the double layer shield, an experiment setup is built, as shown in Fig. 5-15(a). A 3D printer is utilized to print the square bowl with grooves for transmitter coils cut in the inner surface. Litz wire is manually placed in the groove. Several double layer shield sheets from TDK are attached on the outer surface of the charging bowl and the top cover shield is not shown in Fig. 5-15(a). The double layer sheet consists of a 0.3mm FJ7 ( $\mu_r = 110$ ) layer and a 0.1mm aluminum layer. The transmitter coils are driven by three 6.78MHz LCCL-LC resonant converters. The detail of this converter and design can be referred in Chapter 5. The parameter of the transmitter and receiver coils with and without the double layer shield is provided in Table 5.2. To measure the magnetic field, a near field probe from LANGER EMV-Technik is utilized [89]. The picture of the measurement setup is shown in Fig. 5-15(b) and the field probe is placed under the center point A (0, 0, -0.09 m) of the bottom plane of the charging bowl.



(a)



(b)

Fig. 5-15. The picture of the measurement setup. (a). Top view; (b). Side view with near field probe.

TABLE 5.2 THE PARAMETER OF THE COUPLED COILS IN THE SYSTEM

	Without shield	With shield
Transmitter coil 1 self-inductance	6.0uH	6.4uH
Receiver coil inductance	4.7uH	5.5uH
Coupling coefficient	0.23	0.2

The measurement field strength at point A for with and without the double layer shield cases is shown in Table 5.3. With the double layer shield, the magnetic field at point A is attenuated effectively. In Table 5.3, the measurement result matches with the simulation result well for without shield case. However, there is some mismatch for with shield case. The mismatch is caused by the gaps between different shield sheets in the measurement setup as shown in Fig. 5-15(b). The magnetic field can leak through these gaps, and the stray field level increases. But in the simulation, the charging bowl is seamlessly covered by the double layer shield. To reduce the mismatch, these gaps are covered by some small shield patches. The field strength at point A reduces to 1uT afterwards, but it is still larger than the simulation result. One possible reason is

that the termination wire, which connects the transmitter coils to the driver board, would lead to some leakage field. To further reduce the stray field of the termination wire, the double layer shield is wrapped around these wire. And the field strength at point A reduces to 0.32uT, which is below the safe limit 0.4 uT. Therefore, the effectiveness of the double layer shield structure is verified with the measurement.

TABLE 5.3 THE MAGNETIC FIELD STRENGTH AT POINT A

	Without shield	With shield
Simulation	90uT	0.1uT
Measurement	85uT	4uT

To evaluate the impact of the double layer shield on power transfer efficiency, a 55 x 65 mm rectangular coil (4.7uH, 0.4Ω) is placed on the side face of the square bowl as shown in Fig. 5-15(a). The system efficiencies at 5W output for with and without the double layer shield are 78% and 82% respectively. The efficiency drop is mainly caused by the core loss in the ferrite layer, which is around 0.3W according to the FEA simulation.

## 5.5 Conclusion

In this chapter, a square-shaped wireless charging bowl is proposed. The coupling coefficient between the transmitter and receiver coil is spatially uniform, and free-positioning wireless charging is enabled in the square-shaped charging bowl. To reduce the stray field level outside the bowl, a magnetic shield is applied and it is found that the attenuation of the stray field is limited due to low permeability of the available high frequency ferrite material. Therefore, a double layer shield structure, which consists of a ferrite layer and a conductive layer, is proposed to reduce the

stray field effectively. The impact of the properties of each layer on the field distribution is evaluated carefully to provide the design guideline of the double layer shield. Finally, a square-shaped charging bowl with the double layer shield is built and the effectiveness of stray field attenuation is verified by measurement results. The system efficiency of charging a smart phone receiver drops from 82% to 78% at 5W output after applying the double layer shield [91].

# Chapter 6 Intelligent Charging Strategy

## 6.1 Introduction

To improve the charging flexibility, omnidirectional WPT systems have been reported for low power applications recently in [44]-[47]. In [44], an omnidirectional WPT system comprising of three spatially distributed orthogonal transmitter coils and a planar receiver coil is proposed. The magnetic field induced by three transmitter coils is mainly in x, y, and z direction in 3D space and is regarded as the basis vector. The total magnetic field at any point is the vector sum of three magnetic field basis vector. The resultant magnetic field vector can be in different directions with a different ratio among different basis vectors by controlling the excitation current of three transmitter coils. Therefore, the angular misalignment is not an issue any more with an omnidirectional power transfer capability. In [56], [74], a modified three transmitter coil structure is implemented in a cubic shape or a bowl shape. In [75], three transmitter coils structure in a planar form is proposed to generate the magnetic field in different directions for a planar receiver coil. The crossed dipole transmitter coils and receiver coils is reported to generate omnidirectional power transfer capability in [46]. In [76], the resonators in receiver devices are tuned at different frequencies so that three transmitter coils can selectively transfer energy to certain receiver coil by changing the operation frequency.

As pointed out in [44], non-identical current control is necessary for true omnidirectional systems. Either amplitude modulation or phase modulation can be adopted for the transmitter coil current in omnidirectional systems [44]-[47]. It is reported that phase modulation among different transmitter coils results in circulating energy in the system in [77]. Regarding this, amplitude modulation control of the transmitter coil current is preferred. However, the amplitude control of

the ac current is implemented with a power amplifier in [44] and [76], the real circuit implementation has not been discussed in the literature for the best knowledge of the author. Therefore, a system circuit structure to implement the amplitude control of the transmitter coil current is proposed in this chapter.

Non-identical current control is further improved to identify the orientation of the receiver device and focus the power flow towards the load in [52]. When the orientation of the receiver device is determined, the directional power flow directly to the load is more efficient than omnidirectional power flow that involves magnetic field towards unnecessary directions without any load. However, the orientation detection algorithm is evaluated under the single load condition in [52]. In [45], a power flow control based on a weighted time sharing scheme for multiple loads is developed to deliver the power to the appropriate directions based on the load requirement. The orientation of receiver coils is not identified in such algorithm; therefore, it cannot directly focus the magnetic field towards the preferred direction by each receiver device.

In this chapter, a novel control algorithm that can detect the orientation of the receiver coil and focus the power flow towards each receiver is proposed in an omnidirectional WPT system with multiple receiver devices. The system structure is introduced in Section 5.2 and the proposed control algorithm is presented in Section 5.3. In section 5.4, the proposed scheme is verified by experimental tests. Section 5.5 concludes the chapter.

## **6.2 Omnidirectional Wireless Charging Bowl System Structure**

The omnidirectional WPT system is gaining attention due to its charging flexibility as compared with its planar counterpart. The transmitter coils structure is re-drawn in Fig. 1. There are three sets of coils: coil 1a and coil 1b, coil 2a and coil 2b, and coil 3. Herein, coil 1a and coil

1b is connected in series, similarly for coil 2a and coil 2b.

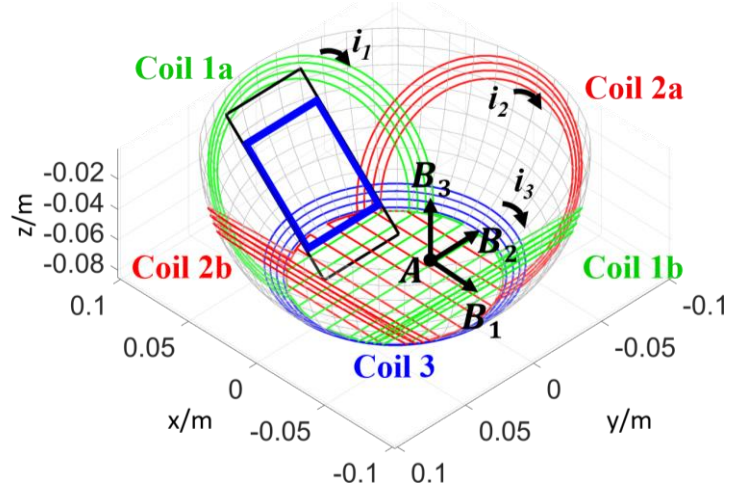


**Fig. 6-1. Transmitter coils structure of an omnidirectional WPT system.**

To generate magnetic field in an omnidirectional manner, non-identical current control must be adopted [44]. The three sets of coils are fed with ac current sources  $i_1$ ,  $i_2$ , and  $i_3$ . The equations for three current are shown in (6.1)-(6.3) [44]. However, it is pointed out that the phase difference among the carrier component (6.78 MHz) of  $i_1$ ,  $i_2$ , and  $i_3$  will cause non-resistive reflected impedance and circulating energy in the system in [77]. Therefore, a double amplitude modulation control for the excitation current is adopted in this chapter. The excitation current in three sets of transmitter coils is illustrated in (6.4)-(6.6).

$$i_1 = I_m \sin(\omega_0 t) \quad (6.1)$$

$$i_2 = I_m \sin(\omega_1 t) \cos(\omega_0 t) \quad (6.2)$$

$$i_3 = I_m \cos(\omega_1 t) \cos(\omega_0 t) \quad (6.3)$$

where:  $\omega_0 = 2\pi \cdot 6.78 \text{MHz}$ ; frequency of the ac current;  $\omega_1 = 2\pi \cdot 450 \text{Hz}$  modulation frequency of the current amplitude;  $I_m$  amplitude of the current.

$$i_1 = I_m \sin(\omega_1 t) \sin(\omega_0 t) \quad (6.4)$$

$$i_2 = I_m \cos(\omega_2 t) \cos(\omega_1 t) \sin(\omega_0 t) \quad (6.5)$$

$$i_3 = I_m \sin(\omega_2 t) \cos(\omega_1 t) \sin(\omega_0 t) \quad (6.6)$$

where:  $\omega_2 = 2\pi \cdot 1kHz$  ,  $\omega_1 = 2\pi \cdot 100kHz$  ,  $\omega_0 = 2\pi \cdot 6.78MHz$  .

The angular frequency  $\omega$  is the system operation frequency, and is 6.78MHz to follow the AirFuel wireless charging standard;  $\omega_1$  and  $\omega_2$  are the modulation frequency to control the amplitude of excitation current. By varying the amplitude of three transmitter coils current, the resultant magnetic field can scan in different directions covering all the directions in 3D manner. The receiving coil always can pick up certain magnetic flux regardless of its orientation. Therefore, there is no angle misalignment issue in the charging setup and the charging flexibility is greatly improved.

In an omnidirectional WPT system, the coils excitation current is controlled to induce the magnetic field in different directions. The cross-coupling among different transmitter coils and the receiver loading effect make the control of the excitation current much more complicated. Therefore, a current source characteristics of the LCCL-LC resonant converter is desired in such systems. As mentioned in Chapter 3, the LCCL-LC resonant converter is a good candidate to drive the transmitter coils at 6.78 MHz in our system. In omnidirectional WPT systems, the amplitude of the transmitter coil excitation current is modulated to scan the magnetic field in different direction. To implement the modulation function, a front buck stage for each transmitter channel is proposed. The proposed system structure is shown in Fig. 6-2. The system input is a dc power source. There are three channel transmitter coil circuits to drive three sets of transmitter coils. The front buck stage controls the input voltage of the LCCL-LC resonant converter stage. The LCCL-LC resonant converter composed of a half bridge, resonant tank and full bridge Schottky rectifier. The down-stream buck charging chip is utilized to charge the device battery with a certain profile.

There are multiple receiver devices in the system.

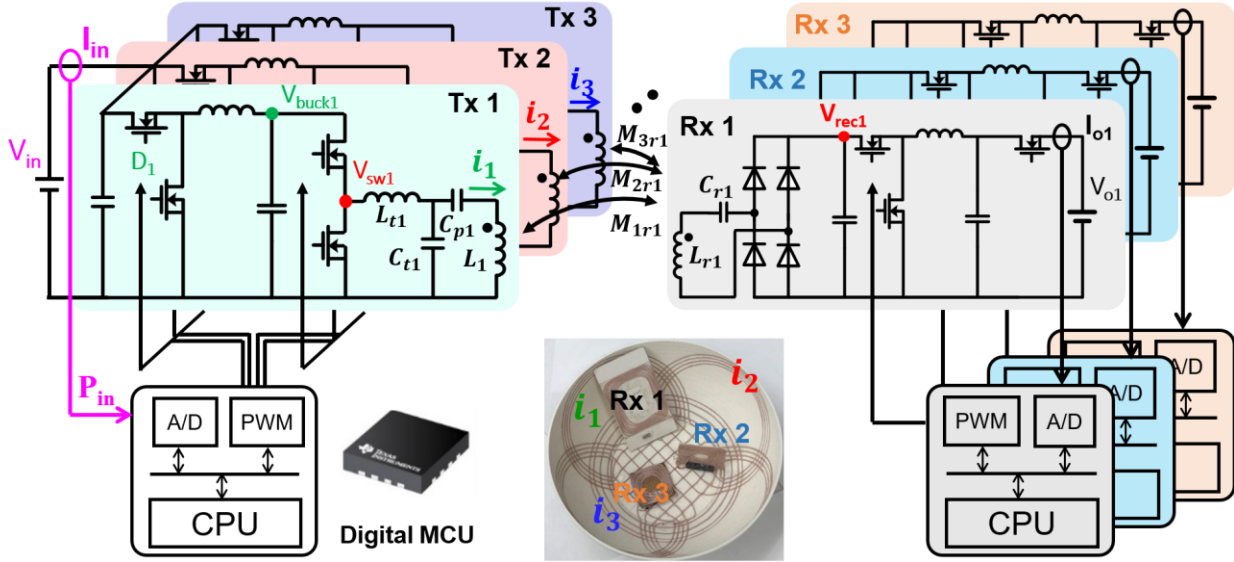


Fig. 6-2. Proposed system structure for the omnidirectional WPT charging bowl system.

As studied in Chapter 4, the amplitude of the excitation current flowing through the transmitter coil in the LCCL-LC converter at the resonant frequency is:

$$I_i = \frac{V_{bucki}}{\omega_0 L_{ri}} \quad (6.7)$$

where:  $I_i$  is the excitation current in the  $i^{th}$  transmitter coil;  $V_{bucki}$  is the output voltage of front buck stage in the  $i^{th}$  transmitter coil circuit;  $\omega_0$  is the system resonant frequency;  $L_{ri}$  is the compensation inductance in the  $i^{th}$  transmitter coil circuit. In (6.7), the transmitter coil excitation current is only determined by output voltage of the front buck stage and the impedance of the compensation inductance, which is independent of the coupling and load conditions. The output voltage of the synchronous buck stage is related to the duty cycle of the top switch ( $D_i$ ) in steady state:

$$V_{bucki} = D_i V_{in} \quad (6.8)$$

where:  $V_{in}$  is the system input voltage.

According to (6.7) and (6.8), the amplitude of the excitation current of the transmitter coil can be controlled by the duty cycle of the front buck stage. A digital micro-controller (MCU) is utilized to give the PWM signal to the front buck stage and control the duty cycle for each transmitter coil circuit. The amplitude modulation function in (6.4)-(6.6) is implemented with a look-up table in the MCU. Meanwhile, the MCU also provide 6.78MHz symmetric complementary PWM signals for the half bridge of the LCCL-LC converter.

In (6.4)-(6.6), the modulation component of the excitation current can be negative; however, the output voltage of the front buck stage is always positive. To achieve negative modulated amplitude, the gate signal of the half-bridge of the LCCL-LC converter need to be delayed  $180^\circ$ . The switching node voltage waveforms and the transmitter coils current waveforms under positive and negative modulation component are demonstrated in Fig. 6-3.

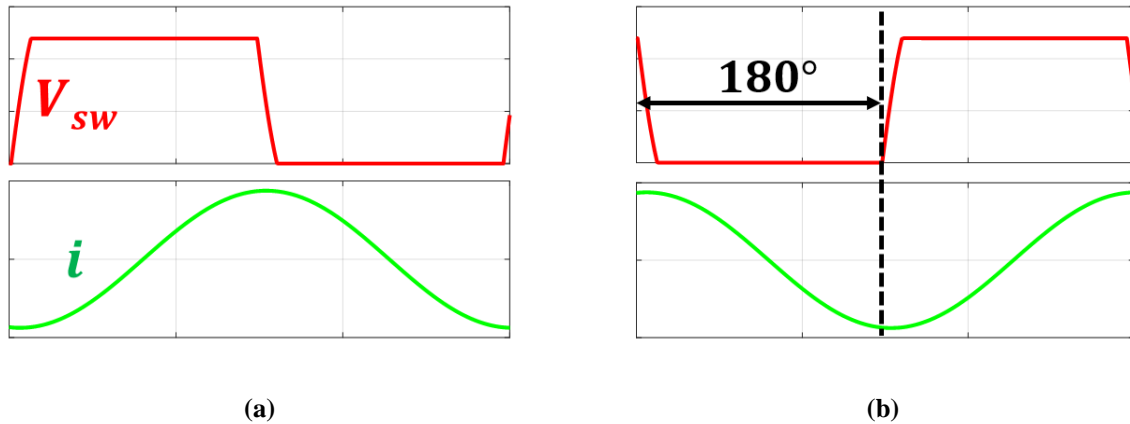


**Fig. 6-3. Switching node voltage and transmitter coil current waveforms under different modulation components. (a). Positive modulation component; (b). Negative modulation component.**

In the proposed system structure, the MCU controls the excitation current flowing through three sets of transmitter coils. With the modulated excitation current, the magnetic field scans in different directions covering all the directions in 3D manner. When the receiver coil picks up enough magnetic flux, the induced voltage in the receiver coil will be large enough to enable the charging chip embedded in the device. Then, the down-stream charging chip provided a regulated

charging power for the battery.

There are three sets of transmitter coils and multiple receiver coils in the proposed omnidirectional WPT system. The coupled coils system is described by the matrix equation in (6.9).

$$\begin{bmatrix} \mathbf{U}_1 \\ \mathbf{U}_2 \\ \mathbf{U}_3 \\ \mathbf{U}_{\text{rec}1} \\ \vdots \\ \mathbf{U}_{\text{rec}j} \end{bmatrix} = \begin{bmatrix} j\omega_0 L_1 & j\omega_0 M_{12} & j\omega_0 M_{13} & j\omega_0 M_{1r1} & \cdots & j\omega_0 M_{1rj} \\ j\omega_0 M_{21} & j\omega_0 L_2 & j\omega_0 M_{23} & j\omega_0 M_{2r1} & \cdots & j\omega_0 M_{2rj} \\ j\omega_0 M_{31} & j\omega_0 M_{32} & j\omega_0 L_3 & j\omega_0 M_{3r1} & \cdots & j\omega_0 M_{3rj} \\ j\omega_0 M_{1r1} & j\omega_0 M_{2r1} & j\omega_0 M_{3r1} & j(\omega_0 L_{r1} - \frac{1}{\omega_0 C_{r1}}) & \cdots & j\omega_0 M_{r1j} \\ \vdots & \vdots & \vdots & \vdots & \ddots & \vdots \\ j\omega_0 M_{1rj} & j\omega_0 M_{2rj} & j\omega_0 M_{3rj} & j\omega_0 M_{rj1} & \cdots & j(\omega_0 L_{rj} - \frac{1}{\omega_0 C_{rj}}) \end{bmatrix} \begin{bmatrix} \mathbf{I}_1 \\ \mathbf{I}_2 \\ \mathbf{I}_3 \\ \mathbf{I}_{r1} \\ \vdots \\ \mathbf{I}_{rj} \end{bmatrix}. \quad (6.9)$$

In (6.9),  $L_i$  is the self-inductance of the  $i^{\text{th}}$  transmitter coil;  $L_{rj}$  is the self-inductance of the  $j^{\text{th}}$  receiver coil;  $M_{ik}$  is the mutual inductance between the  $i^{\text{th}}$  transmitter coil and the  $k^{\text{th}}$  transmitter coil;  $M_{irj}$  is the mutual inductance between the  $i^{\text{th}}$  transmitter coil and the  $j^{\text{th}}$  receiver coil;  $M_{rjk}$  is the mutual inductance between the  $j^{\text{th}}$  receiver coil and the  $k^{\text{th}}$  receiver coil;  $C_{rj}$  is the compensation capacitance for the  $j^{\text{th}}$  receiver coil;  $\mathbf{U}_1$ ,  $\mathbf{U}_2$  and  $\mathbf{U}_3$  are the voltages across the transmitter coils in phasor domain;  $\mathbf{I}_1$ ,  $\mathbf{I}_2$  and  $\mathbf{I}_3$  are the current flowing through the transmitter coils in phasor domain;  $\mathbf{U}_{\text{rec}j}$  is the ac voltage fed to the rectifier bridge in  $j^{\text{th}}$  receiver circuit in phasor domain;  $\mathbf{I}_{rj}$  is the current flowing through the  $j^{\text{th}}$  receiver coil. At the resonant frequency, the reactance of  $L_{rj}$  is cancelled by the reactance of  $C_{rj}$ :

$$j(\omega_0 L_{rj} - \frac{1}{\omega_0 C_{rj}}) = 0. \quad (6.10)$$

In the proposed charging bowl system, the receiver devices are intended to be scattered. In other words, there is no overlapping among different receiver coils. Regarding this, the cross coupling between different receiver coils is neglected in the system analysis. Therefore, the ac voltage fed to the rectifier bridge can be calculated as:

$$V_{recj} = \frac{\pi}{4} \omega_0 (M_{1rj} I_1 + M_{2rj} I_2 + M_{3rj} I_3). \quad (6.11)$$

where:  $I_i$  is the amplitude of the excitation current in the  $i^{th}$  transmitter coil.

In (6.11), the rectifier voltage in the receiver device is determined by the product of the mutual inductance and the corresponding transmitter coil excitation current, which represents the magnetic flux received by the receiver coil. By modulating the amplitude of the transmitter coil current, the magnetic field rotates in 3D manner and covers all the possible directions. When the magnetic field direction is paralleled with the receiver coil plane, the total magnetic flux picked by the receiver coil is zero and the rectifier voltage will be zero. Then the down-stream charging chip cannot be enabled and the battery is not connected to the system. There is no energy transfer. When the angle between the magnetic field and the receiver coil plane is large enough, the received magnetic flux is large enough to generate a rectifier voltage exceeding the threshold voltage of the charging chip. Then the charging chip is enabled, the battery is connected to the system. The output power is determined by the battery status and the charging profile.

With the rotational magnetic field, the receiver can always pick up energy from the charging bowl in certain period. However, there is energy waste period when the received magnetic flux is small. To improve the charging speed, a detection algorithm to find the receiver's location and orientation is desired. With the knowledge of the receiver's positioning information, the charging bowl can freeze the field rotation and focus the energy transfer to the receiver.

## 6.3 Control Algorithm for the Omnidirectional WPT System

### 6.3.1 Review of State-of-Art Control Algorithm

The orientation of the receiver coil impacts the mutual inductance between the receiver coil and each transmitter coil. And the optimal transmitter coil distribution to focus on the energy transfer towards the receiver coil is derived in [52], [70] as (6.12):

$$\frac{I_1 R_1}{M_1} = \frac{I_2 R_2}{M_2} = \frac{I_3 R_3}{M_3}. \quad (6.12)$$

where  $R_1$ ,  $R_2$ ,  $R_3$  stand for the equivalent serial resistance of these three transmitter coils;  $M_1$ ,  $M_2$ ,  $M_3$ , stand for the mutual inductance between the receiver coil and each transmitter coil;  $I_1$ ,  $I_2$ ,  $I_3$  stand for the excitation current for each transmitter coil. If the transmitter coil current follows (6.12), the coil to coil efficiency can be maximized. Therefore, the mutual inductance estimation is the key to identify the positioning and angle information of the receiver coil and the MCU can control the transmitter coil current to focus the energy towards the receiver coil according to (6.12). Some dynamic mutual inductance estimation algorithms have been proposed in [72], [78].

However, only coil conduction losses are accounted in the coil to coil transmission efficiency in [52], [70]. In practice, other converter losses are also significant as demonstrated in Fig. 4-22 in chapter 4. After considering this, the optimal condition for the transmitter coil current distribution in (6.12) cannot hold. Besides, it is assumed that there is just one receiver coil in the setup in [52], [70]. In practice, the number of the receiver coils is flexible and it is very hard to estimate the mutual inductance information under such condition.

In [45], a control algorithm focusing the power requirement is proposed without directly detecting the orientation of the receiver coils. The input power information of each magnetic field

is sensed and recorded while scanning the magnetic field in discrete steps. The input power increases if the magnetic field is good enough to charge certain receiver coil. The input power information is used to predict the load information. Then a power flow control based on a weighted time sharing scheme for multiple loads is developed to deliver the power to the appropriate directions based on the load requirement. In such algorithm, the orientation of receiver coils are not identified; therefore, it cannot directly focus the magnetic field towards the preferred direction of each receiver device. Regarding this, a detection algorithm with multiple scanning process to find the receiver coils' orientation in multiple loads scenario is proposed in this chapter.

### 6.3.2 Proposed Smart Detection Algorithm

As shown in Fig. 6-2, Rx 1 is placed in the charging zone of the coil 1. Therefore, the Rx 1 will be charged as long as the excitation current flowing through coil 1 ( $i_l$ ) is large enough. When the excitation current is modulated as (6.4)-(6.6) in discrete steps, the input power increases as long as  $i_l$  is large enough. Therefore, the output power transferred to Rx 1 appears in the input power information multiple times while the magnetic field is scanning in different direction. If the synthesized magnetic field is good enough charges other receiver devices other than Rx 1, the load power of Rx 1 and other receiver devices will be added up in the total system input power information. Unfortunately, the MCU cannot identify this load power overlapping phenomena with single field scanning process; and therefore receiver devices cannot be identified accurately.

To solve this problem, the MCU excites three transmitter coils one by one at first and identify all the receiver coils which can be charged by single transmitter coil. The MCU sets the duty cycle of the three front buck stage as  $(D_1, D_2, D_3) = (1, 0, 0)$  for certain period and senses the input current and voltage information as shown in Fig. 6-2. The input power is calculated and stored in array  $\mathbf{P}_{in\_1}[1]$  when the transmitter coil 1 set is excited only. If the input power  $\mathbf{P}_{in\_1}[1]$  is larger

than the stand-by power, there is a receiver device which can be charged by the transmitter coil 1 individually. It is worth noting that it is possible there are multiple receiver devices physically under such condition; however, they are identified as one receiver device electronically since they can be charged simultaneously and there is no need to differentiate them in terms of the transmitter coil excitation way. And the MCU sets the load flag array  $\mathbf{F_I} [1] = 1$ ; otherwise,  $\mathbf{F_I} [1] = 0$ . Then the MCU repeats the process for the transmitter coil 2 and 3. The load information is stored in  $\mathbf{F_I} [2]$  and  $\mathbf{F_I} [3]$ . This process is illustrated with the waveforms in Fig. 6-4. In the example receivers' positioning scenario as shown in Fig. 6-2,  $\mathbf{F_I} = [1, 0, 1]$ ; therefore, receiver devices Rx 1 and Rx 3 are identified in the first step.

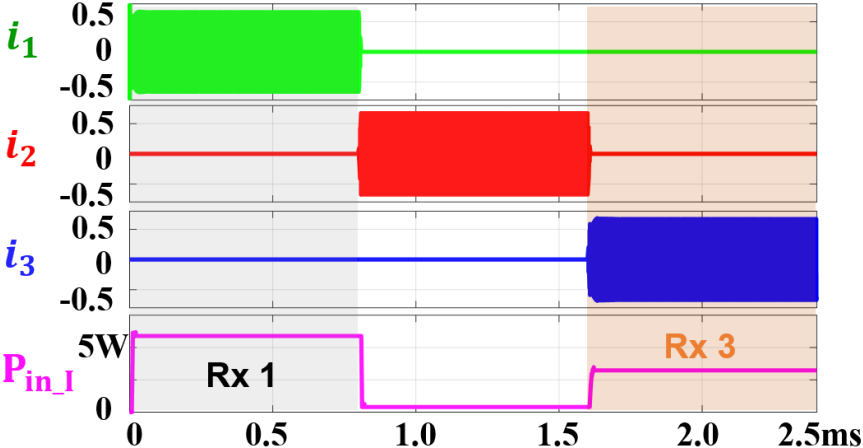


Fig. 6-4. The waveforms under exciting three transmitter coils one by one in the example receiver positioning scenario of Fig. 6-2 .

Secondly, the MCU excites two transmitter coils simultaneously and identify all the receiver coils which can be charged by two transmitter coils. The waveform with the transmitter coil 1 and coil 2 excited with modulated excitation current is shown in Fig. 6-5. The transmitter coil excitation current equation is

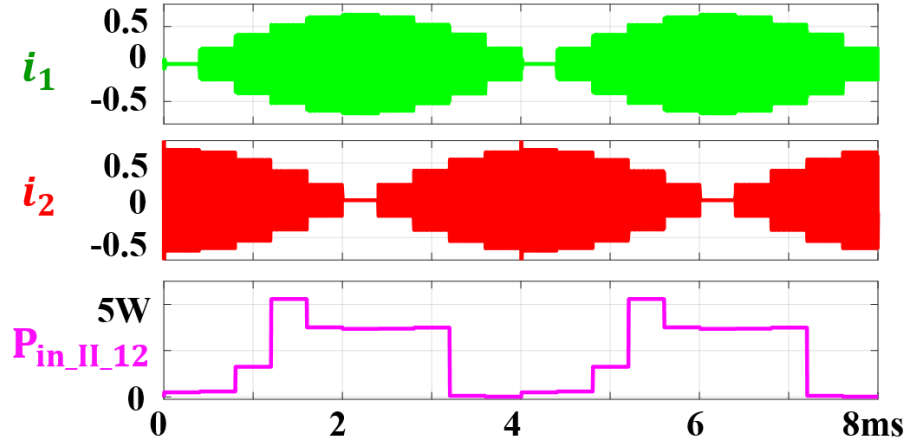


Fig. 6-5. The waveforms under exciting the transmitter coil 1 and coil 2 together with modulated excitation in the example receiver positioning scenario of Fig. 6-2 .

$$i_1 = I_m \sin(\omega_1 t) \sin(\omega_0 t) \quad (6.13)$$

$$i_2 = I_m \cos(\omega_1 t) \sin(\omega_0 t) \quad (6.14)$$

$$i_3 = 0. \quad (6.15)$$

With the excitation current in (6.13)-(6.15), the magnetic field rotates in xy plane covering all the directions in the plane as shown in Fig. 6-8 [79]. With digital implementation in this paper, the magnetic field rotates in 20 directions discretely. The input power information for each field direction is stored in an array named  $\mathbf{P}_{in\_II\_12}$ . Herein, the input power information contains load power of the receiver devices which can be charged by only one transmitter coil. In the example receivers' positioning scenario shown in Fig. 6-2,  $\mathbf{P}_{in\_II\_12}$  contains load power transferred to Rx 1 as long as  $i_1$  is large enough. It is difficult for the MCU to differentiate receiver devices according to  $\mathbf{P}_{in\_II\_12}$  since the load power of Rx 1 appears multiple times. To identify the load power transferred to Rx 1, the MCU disables transmitter coil 1 and senses the input power information. The load information transferred to Rx 1 is then identified in  $\mathbf{P}_{in\_II\_1}$  as shown in Fig. 6-6. By

subtracting  $P_{in\_II\_1}$  from  $P_{in\_II\_12}$ , the input power transferred to receiver devices other than Rx 1 is obtained as

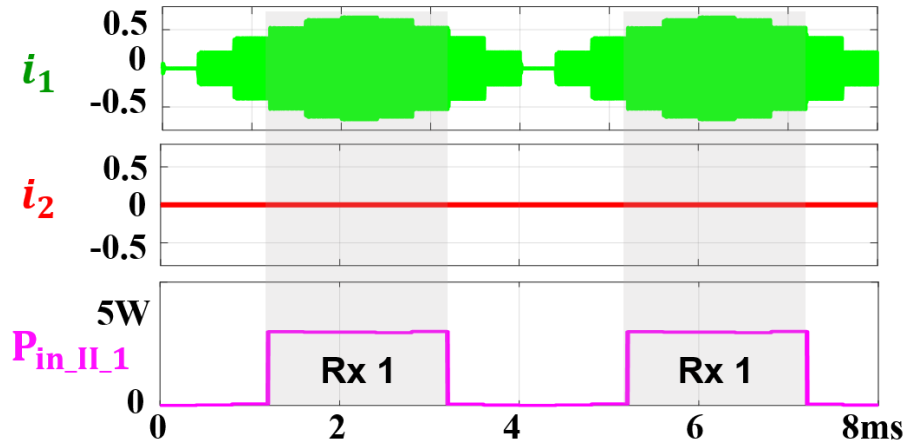


Fig. 6-6. The waveform for identifying the load information transferred to Rx 1 in two transmitter coil 1 and 2 excitation case.

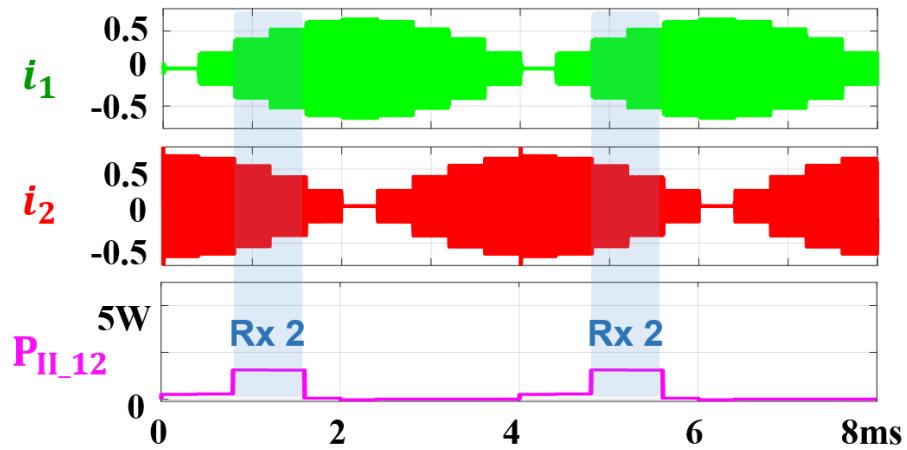


Fig. 6-7. The input power information for transmitter coil 1 and coil excitation case after subtracting load power transferred to Rx 1.

$$P_{II\_12} = P_{in\_II\_12} - P_{in\_II\_1} \quad (6.16)$$

Each plateau area in  $P_{II\_12}$  waveform indicates that a receiver device is charged during such period. It is worth noting that it is possible there are multiple receiver devices physically in each plateau period; however, they are identified as one receiver device electronically. In Fig. 6-7, there

are two symmetric plateaus with the same amount of input power. The receiver's orientation and field directions in xy plane for the example case is illustrated in Fig. 6-8. The black arrows represent 20 different magnetic field directions. When the magnetic field is in the shaded period, the receiver coil receives enough flux. The induced voltage is high enough to enable the charging chip and therefore the system transfers certain energy to the battery based on the charging profile and battery status. A plateau is formed in  $\mathbf{P}_{II\_12}$  waveform during such period. Due to symmetry, there would be two plateaus for one receiver device: one with field flowing into the receiver plane; the other one with field flowing out of the receiver plane. The magnetic field direction to charge the receiver is selected as the blue arrow in the middle of the shaded period. The MCU calculates the transmitter coils excitation current vector for charging Rx 2 as follows

$$\mathbf{I}_{\text{Rx}_2} = \left( \frac{I_1[m] + I_1[n]}{2}, \frac{I_2[m] + I_2[n]}{2}, 0 \right). \quad (6.17)$$

where  $(I_1[m], I_2[m], 0)$  is the current amplitude of each transmitter coil when the input power rises to the plateau;  $(I_1[n], I_2[n], 0)$  is the current amplitude of each transmitter coil when the input power falls from the plateau. The MCU records the excitation current set and ends the detection process for the case of transmitter coil 1 and coil 2 excited simultaneously. Then the MCU repeats the process for transmitter coil 2 and coil 3 and identifies all the receiver devices which can be charged by these two coils. Similar process is also conducted for transmitter coil 1 and coil 3.

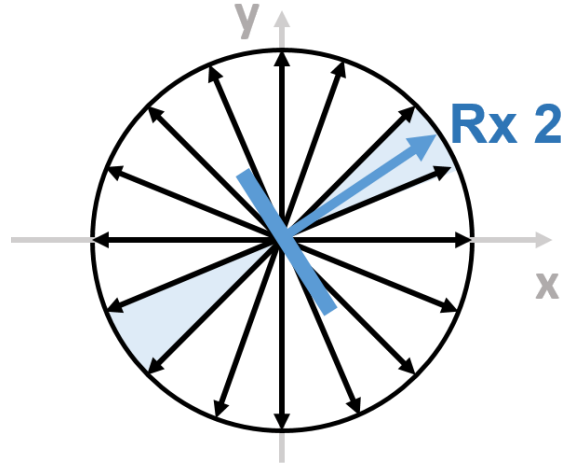


**Fig. 6-8. The magnetic field directions in xy plane when the transmitter coil 1 and coil 2 are excited simultaneously in step II.**

Thirdly, the MCU excites all three set of transmitter coils together according to (6.4)-(6.6). The magnetic field rotates in 3D manner and the input power information for each field direction is recorded in an array named  $\mathbf{P}_{in\_III}$ . Similarly as two coils excitation case, the load information of receiver devices detected in previous step appears multiple times in  $\mathbf{P}_{in\_III}$ . Therefore, the MCU identifies all these load information by disabling certain transmitter coils. Then the MCU subtracts these information from  $\mathbf{P}_{in\_III}$ . The plateau in the resultant input power information indicates a receiver device is charged during such period. In this step, receiver devices which can only be charged when three transmitter coils excited are identified.

In summary, the MCU identifies all the receiver devices which can be charged by at least one transmitter coil in the first step by exciting three transmitter coils sequentially. In the second step, the MCU identifies all the receiver devices which can be charged by at least two transmitter coils. Finally, the MCU identifies the receiver devices which can be charged by three transmitter coils. The excitation current vector for each identified receiver device is recorded in the MCU as:

$$\mathbf{I}_{Rx\_j} = (I_{1\_Rx\_j}, I_{2\_Rx\_j}, I_{3\_Rx\_j}) \quad (6.18)$$

where:  $j$  represents the  $j^{th}$  receiver device;  $I_{1\_Rx\_j}$ ,  $I_{2\_Rx\_j}$ , and  $I_{3\_Rx\_j}$  are the excitation current amplitude of each transmitter coil preferred by the  $j^{th}$  receiver device.

### 6.3.3 Maximum Efficiency Tracking Function

As mentioned in section 6.3.2, the MCU selectively excites three transmitter coils sequentially and identify the receiver devices which can be charged by one transmitter coil in the first step. If there is a receiver device in a certain transmitter coil charging zone, the transmitter transfers energy to the receiver coil and the circuit schematic under such case is shown in Fig. 6-9. In the detection phase, the duty cycle of the front buck stage ( $D$ ) is set as 100% to make sure the excitation current of the transmitter coil is large enough to enable the charging chip embedded in the receiver device. However, 100% duty cycle is not necessarily the optimum duty cycle in terms of the system efficiency. Therefore, a maximum efficiency tracking function to find the optimum duty cycle is implemented in our system.

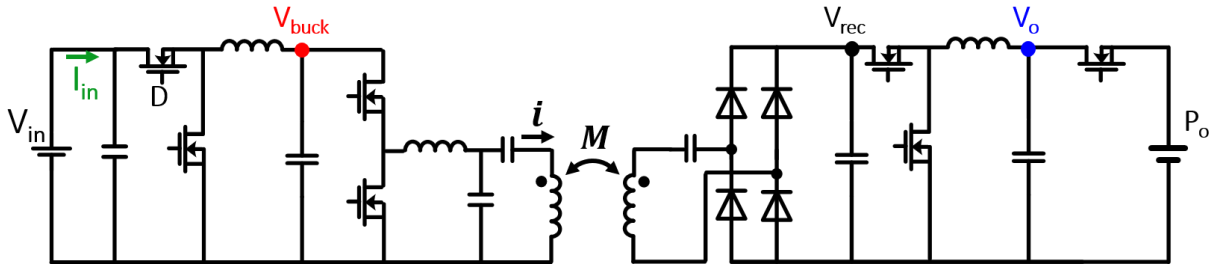


Fig. 6-9. The circuit diagram under one transmitter and one receiver case.

When the duty cycle decreases, the output voltage of the front buck stage reduces and therefore the transmitter coil excitation current decreases according to (6.7). The transmitter coil conduction loss and the switching loss of the half bridge devices also reduces. On the other hand, the rectifier voltage in the receiver side also decreases according to (6.11). Since the output power is determined by the battery status and the charging profile, it can be regarded as constant during

a short period. Therefore, the current flowing through receiver coil becomes larger and the conduction loss of the receiver coil and rectifier diodes increase. Regarding this, there is an optimum duty cycle to achieve the minimum total loss. Since the output power is constant, the input power will be smallest at the optimum duty cycle. A perturbation and observation algorithm is adopted in this paper to search the optimum duty cycle based on the sensed input current information. The upper boundary of the duty cycle is set as 100%. The lower boundary is the duty cycle where the input power decreases rapidly because the induced voltage in receiver coil is not large enough to enable the charging chip when the duty cycle is too small.

After the maximum efficiency tracking process, the excitation current vector  $\mathbf{I}_{\mathbf{R}_x_j}$  for such receiver device is updated with the optimum excitation current amplitude to achieve efficient operation.

#### 6.3.4 Power Flow Control

After identification of all the receiver devices, the MCU controls the power flow towards the receiver devices by pointing the magnetic field to the receiver coil. A time division multiplex strategy can be adopted in the system [80]. Herein, the MCU excites the transmitter coils according to  $\mathbf{I}_{\mathbf{R}_x_j}$  in a time sharing manner. Therefore, the magnetic field only rotates to the required area and the charging speed is improved.

To further improve the charging speed, different receiver devices are powered simultaneously if possible. The general load combination algorithm is described by

$$\begin{aligned} &\text{When } I_{i_{Rx_1}} \times I_{i_{Rx_2}} \times \cdots \times I_{i_{Rx_j}} \geq 0 \\ &|I_{com_i}| = \max(|I_{i_{Rx_1}}|, |I_{i_{Rx_2}}|, \dots, |I_{i_{Rx_j}}|), I_{com_i} \times I_{i_{Rx_j}} \geq 0. \end{aligned} \quad (6.19)$$

where  $I_{com\_i}$  is the final amplitude of the excitation current flowing through the  $i^{th}$  transmitter coil after the load combination;  $I_{i\_Rx\_j}$  is the amplitude of the excitation current flowing through the  $i^{th}$  transmitter coil required by the  $j^{th}$  receiver device. If the transmitter coil excitation current required by different receiver devices has no phase conflict, these loads can be combined together by exciting the transmitter coil with the maximum amplitude required by the receiver devices.

According to (6.11), the rectifier voltage in the  $j^{th}$  receiver device under preferred excitation current vector is:

$$V_{recj} = \frac{\pi}{4} \omega_0 (M_{1rj} I_{1\_Rx\_j} + M_{2rj} I_{2\_Rx\_j} + M_{3rj} I_{3\_Rx\_j}). \quad (6.20)$$

After the load combination strategy, the rectifier voltage in the  $j^{th}$  receiver device is:

$$V_{com\_recj} = \frac{\pi}{4} \omega_0 (M_{1rj} I_{com\_1} + M_{2rj} I_{com\_2} + M_{3rj} I_{com\_3}). \quad (6.21)$$

Subtract (6.20) from (6.21), (6.22) is obtained as

$$V_{com\_recj} - V_{recj} = \frac{\pi}{4} \omega_0 \sum_{i=1}^3 M_{irj} (I_{com\_i} - I_{i\_Rx\_j}) \geq 0. \quad (6.22)$$

Therefore, the rectifier voltage will not decrease after the load combination strategy under the circumstance of (6.19). The system still charges the receiver as long as the rectifier voltage exceeds the threshold voltage of the charging chip. Regarding this, all the receiver devices under  $I_{i\_Rx\_1} \times I_{i\_Rx\_2} \times \dots \times I_{i\_Rx\_j} \geq 0$  can be charged simultaneously with the load combination strategy.

As mentioned in section 6.2, the negative amplitude of the transmitter coil excitation current is implemented by delaying the gate signal of the 6.78MHz half bridge. Therefore, different phase relationship of the gate signal is required if the sign of  $I_{i\_Rx\_j}$  is different; and load combination

strategy cannot be implemented due to phase conflict of the LCCL-LC half bridge. In such condition, the time-division multiplex strategy is adopted.

In the example receiver positioning in Fig. 2, the excitation current vector for three receiver devices are:  $\mathbf{I}_{\text{Rx}_1} = (0.75, 0, 0)$ ;  $\mathbf{I}_{\text{Rx}_2} = (0.7, 0.7, 0)$ ;  $\mathbf{I}_{\text{Rx}_3} = (0, 0, 0.9)$ . According to the load combination strategy, the final excitation current vector is (1, 0.7, 1) to charge three devices together. It is worth noting that the load combination strategy is under the assumption that the transmitter circuits are capable to provide the required energy by the receiver devices. Otherwise, the overcurrent protection circuit in the transmitter circuit is enabled. To avoid this, the load combination strategy increases one by one until the overcurrent limitation is reached.

In summary, a smart scanning algorithm with multiple steps is firstly executed to identify the preferred excitation current vector for each receiver device. Then the MCU focuses the power flow towards the receiver devices by the proposed load combination strategy. The system stays at the energy transfer phase for a certain period. The load demands might change as the users take some receiver devices away or some devices are fully charged. Therefore, a re-scanning process is enabled periodically to guarantee that power is delivered to receiver devices efficiently.

## 6.4 Experimental Verification

An omnidirectional wireless charging bowl system is built and the picture of the experiment setup is shown in Fig. 6-10. The system structure is already shown in Fig. 6-2. The system is powered by an Agilent E3631A DC power source at 24 V. The TI microcontroller TMS320C28379 demo board is used to give the PWM signals for the front buck stage and the half bridge of the LCCL-LC circuit. Meanwhile, the MCU senses the dc input voltage and current information and calculates the input power information. Three synchronous front buck stages in the transmitter side

operate at 500 kHz with the EPC2007. The EPC8004 devices are adopted in the half bridge to operate at 6.78 MHz. The parameter of the passive components is present in Table 6.1. In the receiver side, four discrete DFSL130 diodes are adopted for the rectifier bridge. After the rectifier bridge, a close loop regulated buck converter (TPS5410) is utilized to give 5V regulated output for the resistor. This regulated buck converter emulates the downstream battery charging chip in the real application scenario. The output power for three receiver devices are set as 2.5 W, 1.25W, 1.25W.

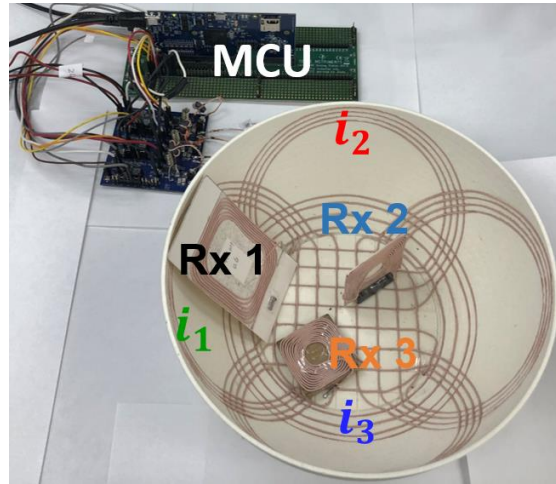


Fig. 6-10. The picture of the experiment setup.

TABLE 6.1 PARAMETER OF PASSIVE COMPONENTS IN THE SYSTEM

Specifications	Symbol	Practical Value
Compensation inductance	$L_{t1}, L_{t2}, L_{t3}$	531nH, 560nH, 549nH
Compensation capacitance	$C_{t1}, C_{t2}, C_{t3}$	1.1nF, 980pF, 1.0nF
Compensation capacitance	$C_{p1}, C_{p2}, C_{p3}$	92pF, 89pF, 160pF
Self-inductance of each transmitter coil	$L_1, L_2, L_3$	6.2uH, 6.4uH, 3.5uH
Self-inductance of receiver coil Rx 1, Rx 2, and Rx 3	$L_{r1}, L_{r2}, L_{r3}$	4.7uH, 7.5uH, 7uH
Compensation capacitance for Rx 1, Rx 2, and Rx 3	$C_{r1}, C_{r2}, C_{r3}$	118pF, 74pF, 78pF
Mutual inductance between Rx 1 and each transmitter coil	$M_{1r1}, M_{2r1}, M_{3r1}$	550nH, 30nH, 50nH
Mutual inductance between Rx 2 and each transmitter coil	$M_{1r2}, M_{2r2}, M_{3r2}$	248nH, 267nH, 32nH

Mutual inductance between Rx 3 and each transmitter coil	$M_{1r3}, M_{2r3}, M_{3r3}$	20nH, 35nH, 345nH
--	-----------------------------	-------------------

### 6.4.1 Smart Detection Algorithm Verification

The smart detection algorithm is implemented in the MCU. The experiment waveforms to illustrate the detection process is demonstrated in Fig. 6-11. As mentioned in section 6.3, there are three steps in the detection process: step 1: one coil excitation phase; step 2: two coils excitation phase and step 3: three coils excitation phase. In step 1, three transmitter coils are selectively excited sequentially and the input current rises as transmitter coil 1 and transmitter coil 3 is excited separately as shown in the zoom in picture in Fig. 6-11. Therefore, Rx 1 and Rx 3, which are located in coil 1 and coil 3 charging zone, are identified. In step 2, two different transmitter coils are excited at the same time. It is worth noting that only half cycle of the modulation period is excited in the test since the magnetic field is symmetric as shown in Fig. 8. In this step, the load power of previous detected receiver devices (Rx 1, Rx 3) in step 1 is identified and subtracted from the input power information. In this step, Rx 2, which standing on the base of the charging bowl, is identified when transmitter coil 1 and coil 2 are excited together. The horizontal magnetic field induced by transmitter coil 1 and coil 2 at base area synthesizes a magnetic field preferred by Rx 2. In step 3, three transmitter coils are excited at the same time. The load power transferred to previous detected receiver devices in step 1 and 2 are identified and subtracted from the input power information. In the example receiver positioning case, there is no plateau in the input power information after the subtraction in step 3, indicating there is no more receiver devices in the setup other than Rx 1, Rx 2 and Rx 3. Finally, the MCU outputs the excitation current vector for these receiver devices as shown in Fig. 6-11. The smart detection result matches the real scenario very well.

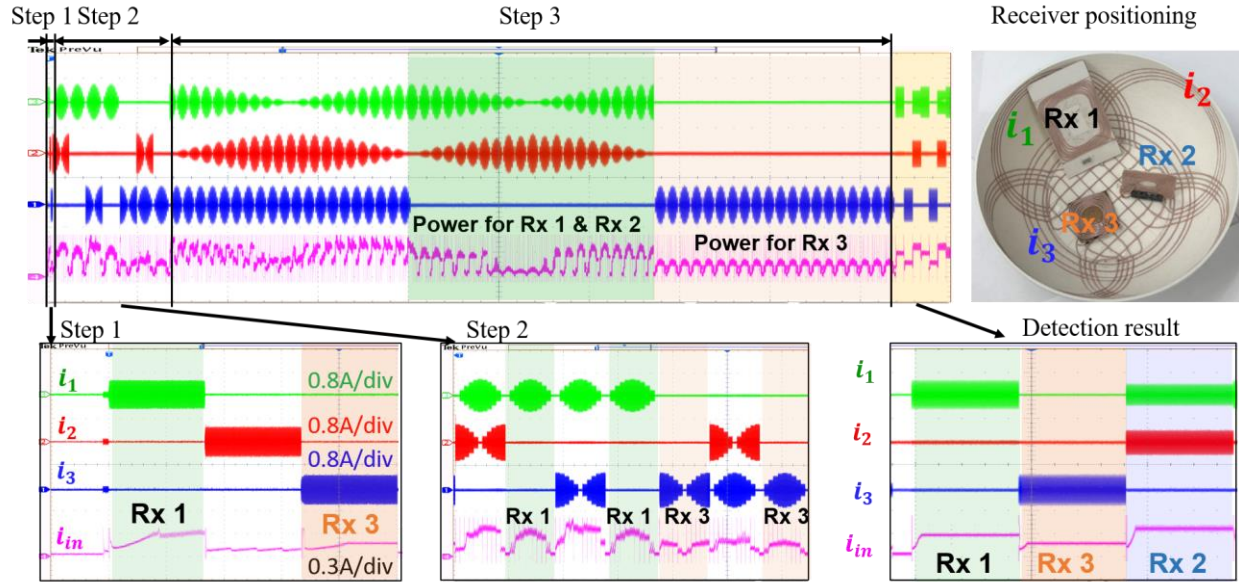


Fig. 6-11. Experimental waveforms for smart detection algorithm.

#### 6.4.2 Maximum Efficiency Tracking Function Verification

After identification of the receiver devices, maximum efficiency tracking function can be implemented to improve the system efficiency. The experimental waveforms for the maximum efficiency tracking for Rx 1 is shown in Fig. 6-12.  $V_o$ ,  $V_{buck}$  and  $I_{in}$  are defined as the system output voltage, the output voltage of the front buck and the input current in Fig. 6-9. The MCU sweeps the duty cycle of the front buck stage and controls the bus voltage  $V_{buck}$ . Herein, the bus voltage  $V_{buck}$  decreases gradually from 24V to 10V, where the sensed input current drops substantially. There is no need to further reduce  $V_{buck}$  after 10V due to rapid drop of the input power. Meanwhile, the MCU records the input current and input voltage information and calculates the input power information for each operation point. Then the MCU finds the optimum point with the minimum input power. In the example case for Rx 1, the optimum operation point for  $V_{buck}$  is at 18 V and the system efficiency improves from 64 % at  $V_{buck} = 24$  V to 66 % at  $V_{buck} = 18$  V. The optimum excitation current vector  $(I_1, I_2, I_3)$  for Rx 1 will be (0.75, 0, 0).

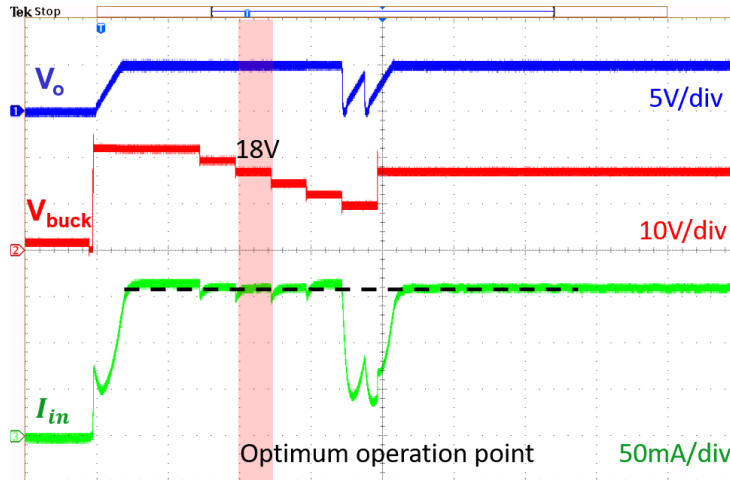


Fig. 6-12. Experimental waveforms for the maximum efficiency tracking function for Rx 1.

### 6.4.3 Power Flow Control Verification

After the smart detection algorithm with maximum efficiency tracking function, the preferred excitation current vector for three receiver devices are:  $\mathbf{I}_{Rx\_1} = (0.75, 0, 0)$ ;  $\mathbf{I}_{Rx\_2} = (0.7, 0.7, 0)$ ;  $\mathbf{I}_{Rx\_3} = (0, 0, 0.9)$ . According to the load combination strategy, the final excitation current vector is  $(0.75, 0.7, 0.9)$  to charge three devices together. The load implementation strategy is implemented in the MCU and the experimental waveforms to demonstrate the algorithm is shown in Fig. 6-13.

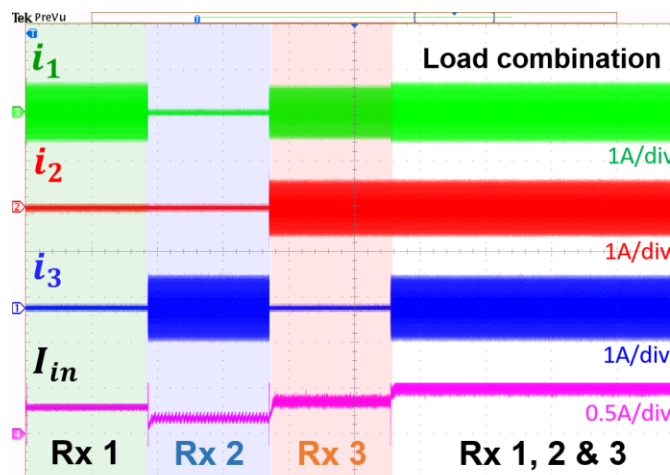
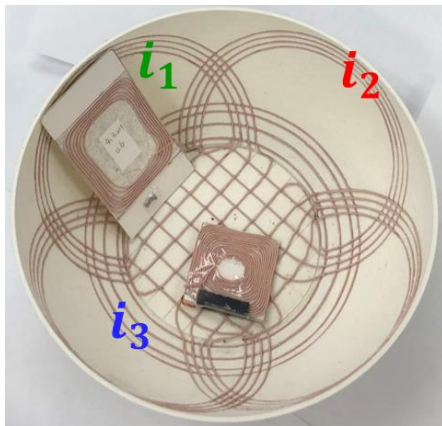


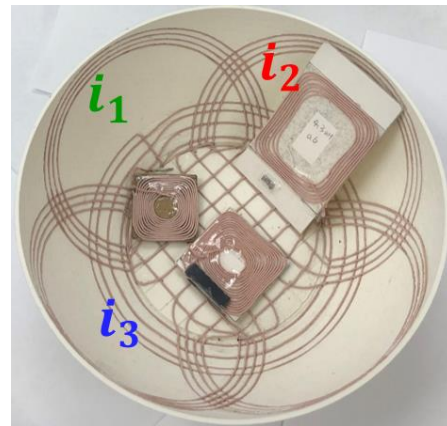
Fig. 6-13. Experimental waveforms for the load combination strategy.

Up to now, the smart detection algorithm and power flow control is verified under one example receiving devices positioning case. To further verify the control scheme, several tests are conducted under different receiving positioning cases. The receiving positioning scenario under four different tests is shown in Fig. 6-14. The test results are summarized in Table 6.2 and the MCU successfully finds all the receiving devices under different cases. The detailed experimental waveforms under different cases is provided in Fig. 6-15.

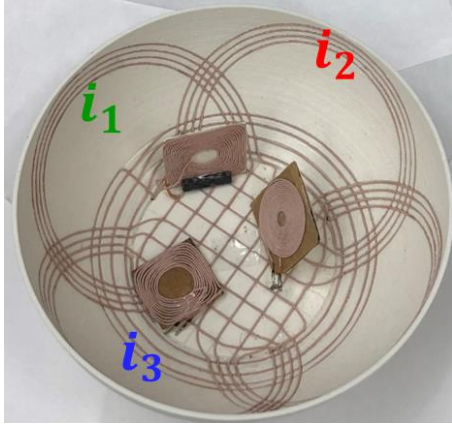
It is worth noting that only two receiving devices are identified in case II although there are three physical receiving devices in the setup. Herein, two receiving devices at the base of the bowl can be charged simultaneously by coil 3 and are identified as one receiving device electrically. In addition, Rx 2 and Rx 3 in case III require different phase relationship of the gate signals of the LCCL-LC half bridge and therefore these two receiving devices cannot be combined together. Regarding this, a time sharing strategy is implemented to charge Rx 2 and Rx 3 in different periods.



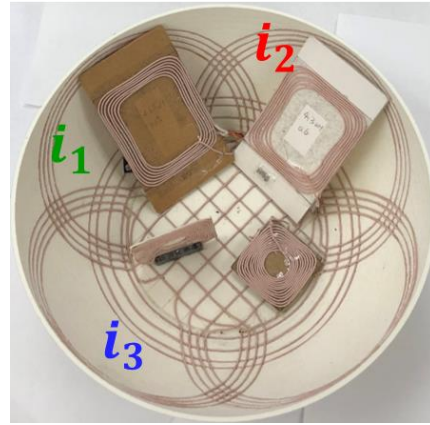
(a)



(b)



(c)

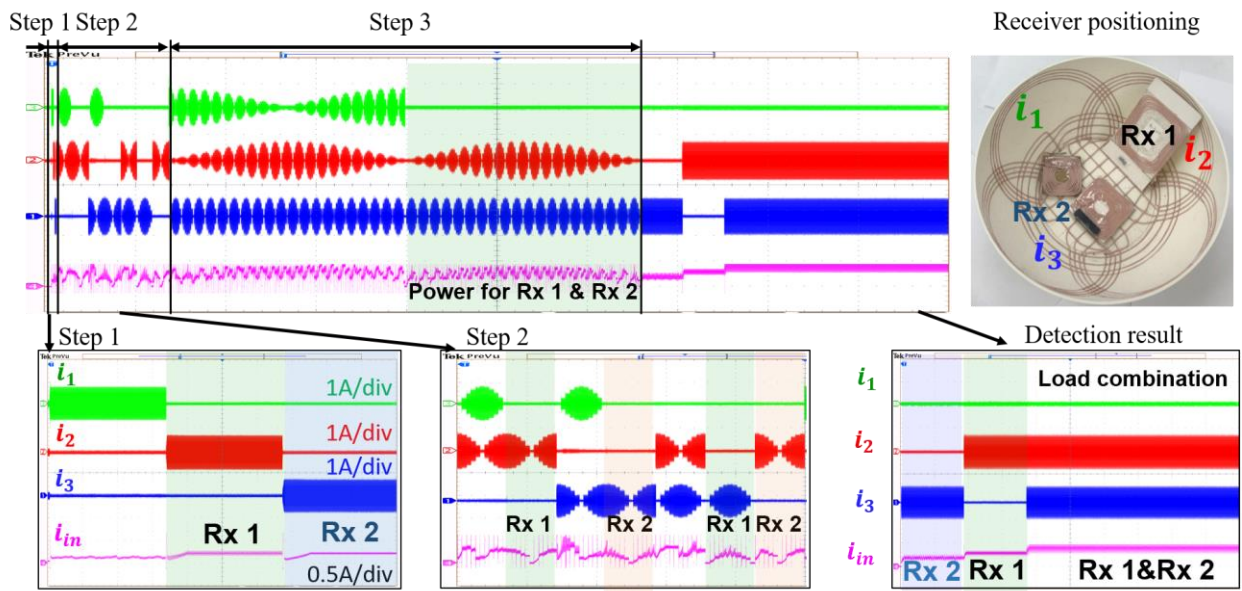
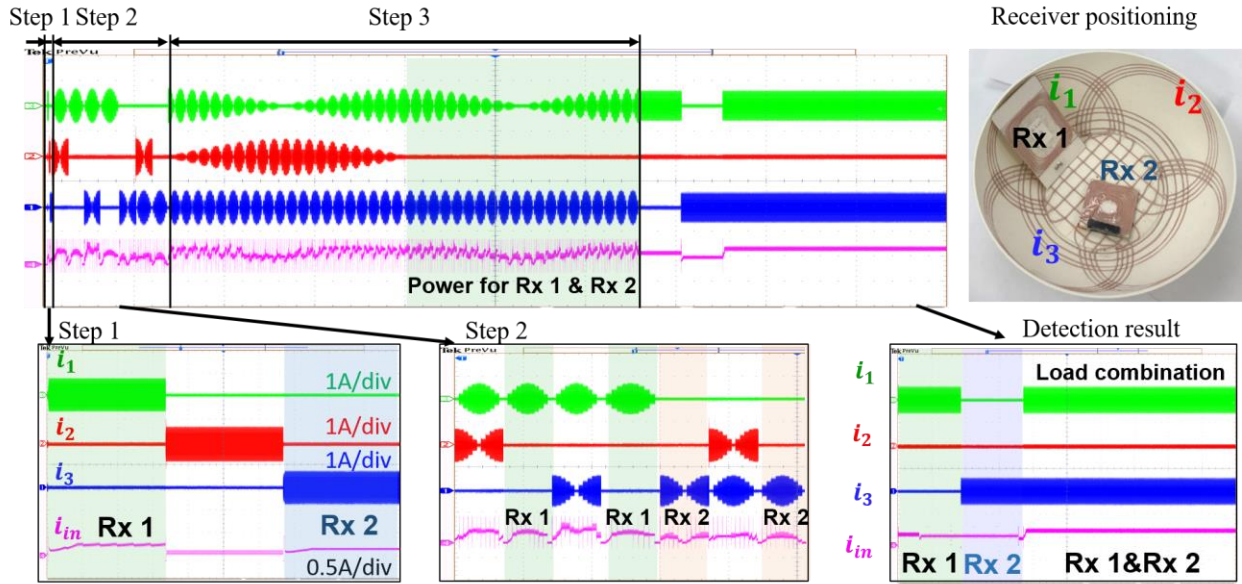


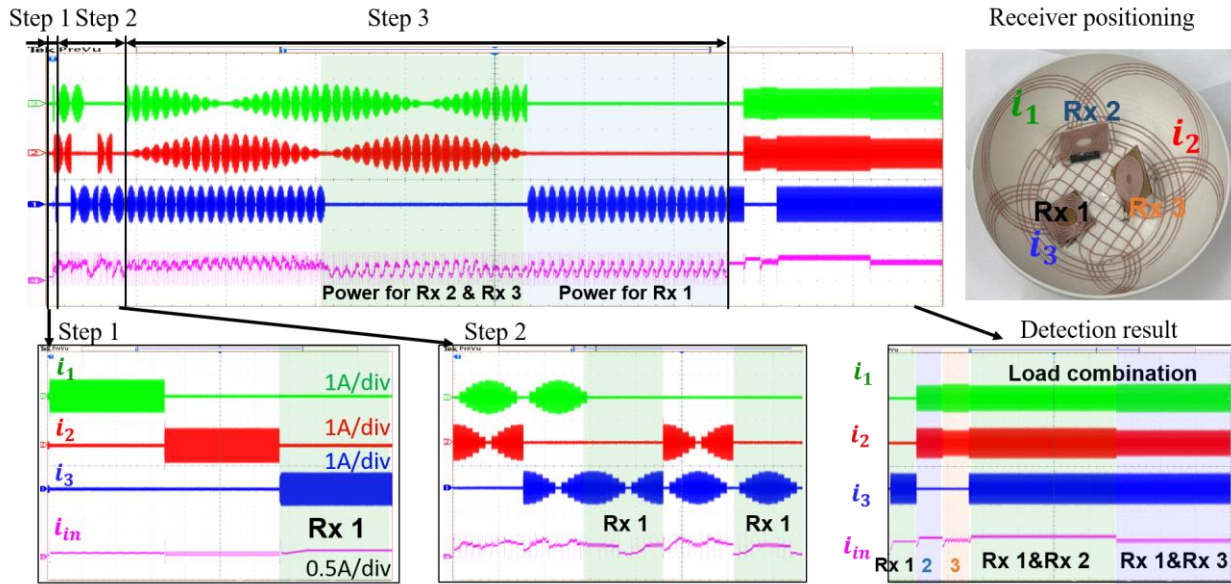
(d)

**Fig. 6-14.** The picture of receiver positioning under different test scenarios. (a). Case I. (b). Case II. (c). Case III. (d).

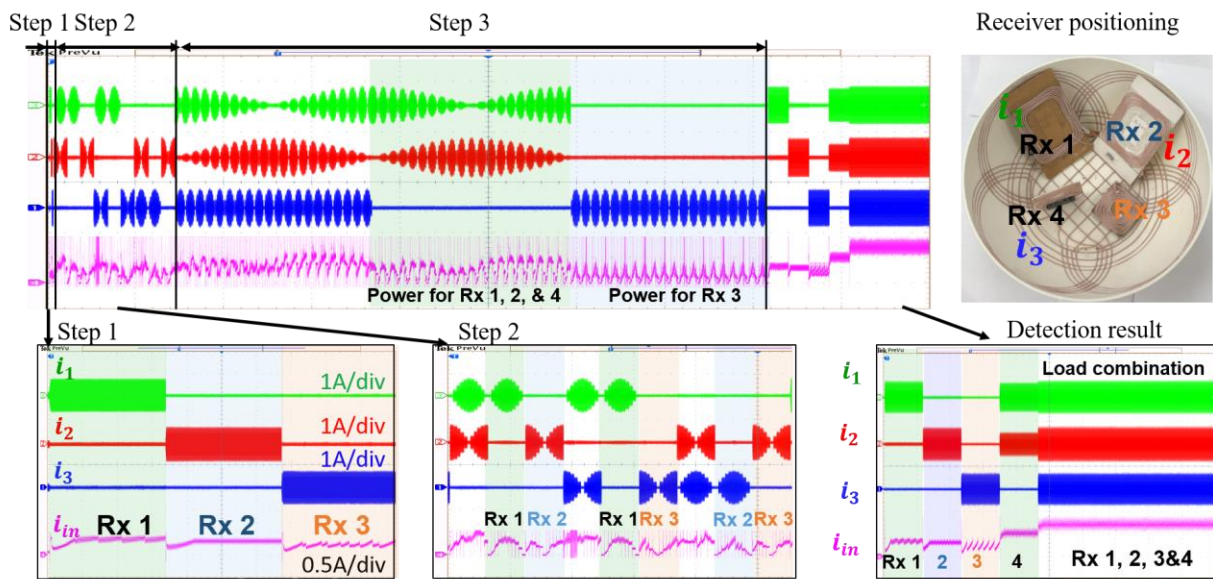
TABLE 6.2 SUMMARY FOR TEST RESULT UNDER DIFFERENT CASES

	Excitation current vector for each receiving device	Final excitation current vector after load combination	System efficiency
Case I	$\mathbf{I}_{Rx\_1}: (0.65, 0, 0)$ $\mathbf{I}_{Rx\_2}: (0, 0, 0.7)$	$\mathbf{I}_{Rx}: (0.65, 0, 0.7)$	55%
Case II	$\mathbf{I}_{Rx\_1}: (0, 0.7, 0)$ $\mathbf{I}_{Rx\_2}: (0, 0, 0.8)$	$\mathbf{I}_{Rx}: (0, 0.7, 0.8)$	60%
Case III	$\mathbf{I}_{Rx\_1}: (0, 0, 0.9)$ $\mathbf{I}_{Rx\_2}: (0.6, 0.8, 0)$ $\mathbf{I}_{Rx\_3}: (0.8, -0.6, 0)$	$\mathbf{I}_{Rx}: (0.6, 0.8, 0.9) \&$ $(0.8, -0.6, 0.9)$	50%
Case IV	$\mathbf{I}_{Rx\_1}: (0.7, 0, 0)$ $\mathbf{I}_{Rx\_2}: (0, 0.7, 0)$ $\mathbf{I}_{Rx\_3}: (0, 0, 0.9)$ $\mathbf{I}_{Rx\_4}: (0.9, 0.4, 0)$	$\mathbf{I}_{Rx}: (0.9, 0.7, 0.9)$	52%





(c)



(d)

Fig. 6-15. Experimental waveforms for smart detection algorithm under different cases. (a). Case I. (b) Case II. (c). Case III. (d). Case IV.

## 6.5 Conclusion

The chapter provides a comprehensive discussion on the control principles of omnidirectional WPT systems. A front buck stage is added before resonant converter to implement the current amplitude control and maximum efficiency point tracking. A smart scanning process identifies the load positioning gradually based on the input power information of each magnetic field vector. The self-learning process enables the identification of multiple loads in the system. Then a load combination algorithm is proposed to transfer energy to multiple loads simultaneously as many as possible. A time-multiplexing strategy is adopted to charge the loads which cannot be powered simultaneously. With proposed power flow control, the omnidirectional WPT system focuses energy towards targeted loads and maximize the power transfer capability of the transmitter circuit.

## Chapter 7 Summary

First, a three-dimensional (3D) coils structure is proposed to transfer energy in omnidirectional manner to improve the charging flexibility compared with the planar coils structure for consumer electronics application. A modulated excitation current scheme is adopted to rotate the magnetic field in different directions and covers all the directions in 3D space in the setup. With omnidirectional magnetic field, the charging platform can provide energy transfer in any direction; therefore, the angle alignment between the transmitter coil and receiver coil is no longer needed. Meanwhile, the transmitter coils geometry is optimized to achieve free-positioning of the receiving devices and the energy transfer efficiency.

Second, the LCCL-LC resonant converter is derived to drive the transmitter coils at 6.78 MHz. In WPT system, the coupling coefficient between the transmitting coil and the receiving coil is subject to the receiver's positioning. The variable coupling condition is a big challenge to the resonant topology selection. The optimal operating point of the LCCL-LC converter is independent of coupling condition. Therefore, the energy transfer is guaranteed in different receiving positioning scenarios. As mentioned, the transmitter coil current should be controlled tightly to achieve the rotation of the magnetic field in the omnidirectional WPT system. The transmitter coil current of the LCC-LC converter is independent of coupling and load condition. With this special merit, the LCCL-LC converter achieves the transmitter coil current control easily in the omnidirectional WPT system.

Thirdly, a design methodology of the LCCL-LC converter to achieve ZVS operation is proposed the omnidirectional WPT system. In consumer electronics applications, Megahertz (MHz) WPT systems are used to improve the charging spatial freedom. The zero voltage switching

(ZVS) operation of the switching devices reduces the switching loss and the switching related electromagnetic interference (EMI) issue in a MHz system. With the proposed design methodology, over 75% system efficiency is achieved for smart phone charging scenario.

Fourthly, a double layer shield structure, which consists of a ferrite layer and a conductive layer, is proposed to reduce the stray field effectively. The impact of the properties of each layer on the field distribution is evaluated carefully to provide the design guideline of the double layer shield. Finally, a square-shaped charging bowl with the double layer shield is built and the effectiveness of stray field attenuation is verified by measurement results. The system efficiency of charging a smart phone receiver drops from 82% to 78% at 5W output after applying the double layer shield.

Lastly, a smart detection algorithm for identifying the positioning and orientation of receiver devices based on the input power information is presented. A smart scanning process identifies the load positioning gradually, based on the input power information of each magnetic field vector. The self-learning process enables the identification of multiple loads in the system. Then a load combination algorithm is proposed to transfer energy to multiple loads, simultaneously, and to as many as possible. A time-multiplexing strategy is adopted to charge the loads which cannot be powered simultaneously. With the proposed intelligent charging strategy, the omnidirectional WPT system focuses energy towards targeted loads and maximizes the power transfer capability of the transmitter circuit.

In this dissertation, a complete battery charging solution for the consumer electronics application is proposed. The energy transfer efficiency is as good as commercial charging pad; however, the charging spatial freedom and orientation freedom is greatly improved with the

omnidirectional power transfer capability. And the safety concern is well addressed with the double layer shielding. With the proposed charging setup, the users can simply drop their devices in the bowl and don't need to worry about the alignment and health issue any more. The authors believe that the proposed system is a promising solution for the battery charging in the consumer electronics application.

## Reference

- [1] J.C. Maxwell. "A dynamical theory of the electromagnetic field". Philosophical Transactions of the Royal Society of London. 155: 459–512, 1865.
- [2] H.R. Hertz, "Ueber einen Einfluss des ultravioletten Lichtes auf die electriche Entladung", Annalen der Physik, vol. 267, no. 8, p. 983–1000, June 1887.
- [3] G. Marconi, "Transmitting electrical signal", US patent 586, 193, July 1897.
- [4] N. Tesla, "Apparatus for transmitting electrical energy", US patent 1,119,732, December 1914.
- [5] Robert Lomas, "The who invented the twentieth century: Nicola Tesla, forgotten genius of electricity," *Headline*; 1999.
- [6] C. C. Mi, G. Buja, S. Y. Choi and C. T. Rim, "Modern Advances in Wireless Power Transfer Systems for Roadway Powered Electric Vehicles," in *IEEE Transactions on Industrial Electronics*, vol. 63, no. 10, pp. 6533-6545, Oct. 2016.
- [7] F. E. Terman, *Radio Engineers' Handbook*, (McGraw-Hill, 1943), p. 37.
- [8] W. H. Ko, S. P. Liang, and C. D. F. Fung, "Design of rf-powered coils for implant instruments," *Med. Biol. Eng. Comput.*, vol. 15, pp. 634–640, 1977.
- [9] E. Hochmair, "System optimization for improved accuracy in transcutaneous signal and power transmission," *IEEE Trans. Biomed. Eng.*, vol. BME-31, no. 2, pp. 177–186, Feb. 1984
- [10] W. G. Hurley and J. Kassakian, "Induction heating of circular ferromagnetic plates," *IEEE Trans. Magn.*, vol. 15, no. 4, pp. 1174–1181, Jul. 1979.
- [11] Wireless Power Consortium Website. (2013). [Online]. Available: <http://www.wirelesspowerconsortium.com>.
- [12] Gartner Press Release. 7 February 2017. [Online]. Available: <https://www.gartner.com/newsroom/id/3598917>.

- [13] D. Bastos, M. Shackleton and F. El-Moussa, "Internet of Things: A survey of technologies and security risks in smart home and city environments," *Living in the Internet of Things: Cybersecurity of the IoT - 2018*, London, 2018, pp. 1-7.
- [14] <https://technology.ihc.com/Services/509494/wireless-power-intelligence-service/Analysis>
- [15] M. Ettorre, W. A. Alomar and A. Grbic, "Radiative Wireless Power-Transfer System Using Wideband, Wide-Angle Slot Arrays," in *IEEE Transactions on Antennas and Propagation*, vol. 65, no. 6, pp. 2975-2982, June 2017.
- [16] Brown WC. Experimental airborne microwave supported platform. Spencer Lab Report, Raytheon CO: Burlington MA; 1965.
- [17] Dickinson RM. Safety issues in SPS wireless power transmission. *Space Policy*. 2000;16(2):117–22.
- [18] Aakash Sahai, and David Graham, "Optical wireless power transmission at long wavelengths," *IEEE International Conference on Space Optical Systems and Applications (ICSOS)*, Santa Monica, CA, pp. 164{170; 2011.
- [19] I. Adithyan, and Neehar Mavuduru, "Space based solar power system: analysis of atmospheric transmittance for laser beam propagation," *2013 International Conference on Power, Energy and Control (ICPEC)*, Dindiu, Tamil Nadu, India; 6-8 Feb 2013.
- [20] S. Y. R. Hui, W. X. Zhong, and C. K. Lee, "A critical review on recent progress of mid-range wireless power transfer," *IEEE Transactions on Power Electronics*, vol. 29, no. 9, pp. 4500–4511, Sept. 2014.
- [21] G. A. Landis, "Applications for Space Power by Laser Transmission," *SPIE Proceedings on Laser Power Beaming*, vol. 2121, pp. 252{255; Jan 1994.
- [22] Johnson I. Agbinya, \Wireless Power Transfer," River Publishers. pp. 1-2;2012.
- [23] H. Zhang, F. Lu, H. Hofmann, W. Liu and C. C. Mi, "A four-plate compact capacitive coupler design and LCL-compensated topology for capacitive power transfer in electric vehicle charging application," *IEEE Trans. Power Electronics*, vol. 31, no. 12, pp. 8541-8551, Dec. 2016.

- [24] M. Kline, I. Izyumin, B. Boser and S. Sanders, "Capacitive power transfer for contactless charging," 2011 Twenty-Sixth Annual IEEE Applied Power Electronics Conference and Exposition (APEC).
- [25] G. A. Covic and J. T. Boys, "Modern Trends in Inductive Power Transfer for Transportation Applications," in *IEEE Journal of Emerging and Selected Topics in Power Electronics*, vol. 1, no. 1, pp. 28-41, March 2013.
- [26] Chwei-Sen Wang, O. H. Stielau and G. A. Covic, "Design considerations for a contactless electric vehicle battery charger," *IEEE Trans. Industrial Electronics*, vol. 52, no. 5, pp. 1308-1314, Oct. 2005.
- [27] Chwei-Sen Wang, G. A. Covic and O. H. Stielau, "Power transfer capability and bifurcation phenomena of loosely coupled inductive power transfer systems," *IEEE Trans. Industrial Electronics*, vol. 51, no. 1, pp. 148-157, Feb. 2004.
- [28] F. Y. Lin, G. A. Covic and J. T. Boys, "Evaluation of magnetic pad sizes and topologies for electric vehicle charging," *IEEE Trans. Power Electronics*, vol. 30, no. 11, pp. 6391-6407, Nov. 2015.
- [29] A. Kurs, A. Karalis, R. Moffatt, J. D. Joannopoulos, P. Fisher, and M. Soljacic, "Wireless power transfer via strongly coupled magnetic resonances," *Science*, vol. 317, no. 5834, pp. 83-86, Jul. 2007.
- [30] S. Cheon, Y. H. Kim, S. Y. Kang, M. L. Lee, J. M. Lee, and T. Zyung, "Circuit-model-based analysis of a wireless energy-transfer system via coupled magnetic resonances," *IEEE Trans. Ind. Electron.*, vol. 58, no. 7, pp. 2906-2914, Jul. 2011.
- [31] C. K. Lee, W. X. Zhong, and S. Y. R. Hui, "Effects of magnetic coupling of non-adjacent resonators on wireless power domino-resonator systems," *IEEE Trans. Power Electron.*, vol. 27, no. 4, pp. 1905-1916, Apr. 2012.
- [32] W. X. Zhong, C. K. Lee, and S. Y. R. Hui, "Wireless power dominoresonator systems with non-coaxial axes and circular structures," *IEEE Trans. Power Electron.*, vol. 27, no. 11, pp. 4750-4762, Nov. 2012.

- [33] W. X. Zhong, C. K. Lee, and S. Y. R. Hui, "General analysis on the use of tesla's resonators in domino forms for wireless power transfer," *IEEE Trans. Ind. Electron.*, vol. 60, no. 1, pp. 261–270, Jan. 2013.
- [34] C.-G. Kim, D.-H. Seo, J.-S. You, J.-H. Park, and B. H. Cho, "Design of a contactless battery charger for cellular phone," *IEEE Transactions on Industrial Electronics*, vol. 48, no. 6, pp. 1238–1247, Dec. 2001.
- [35] B. Choi, J. Nho, H. Cha, T. Ahn, and S. Choi, "Design and implementation of low-profile contactless battery charger using planar printed circuit board windings as energy transfer device," *IEEE Transactions on Industrial Electronics*, vol. 51, no. 1, pp. 140–147, Feb. 2004.
- [36] W. Zhong, X. Liu, and S. Hui, "A novel single-layer winding array and receiver coil structure for contactless battery charging systems with freepositioning and localized charging features," *IEEE Trans. Ind. Electron.*, vol. 58, no. 9, pp. 4136–4143, Sep. 2011.
- [37] Z. Zhang, H. Pang, A. Georgiadis and C. Cecati, "Wireless Power Transfer—An Overview," in *IEEE Transactions on Industrial Electronics*, vol. 66, no. 2, pp. 1044-1058, Feb. 2019.
- [38] D. Wang, Y. Zhu, H. Guo, X. Zhu, T. Mo and Q. Huang, "Enabling multi-angle wireless power transmission via magnetic resonant coupling," in *Computing and Convergence Technology International Conference*, Seoul, 2012, pp. 1395-1400.
- [39] J. Kim, D. H. Kim, J. Choi, K. H. Kim and Y. J. Park, "Free-Positioning Wireless Charging System for Small Electronic Devices Using a Bowl-Shaped Transmitting Coil," *IEEE Transactions on Microwave Theory and Techniques*, vol. 63, no. 3, pp. 791-800, March 2015.
- [40] E. R. Green, M. R. Bynum, N. A. Redfield "Wireless charging device having concave charging station" U.S. patent 0188339, Jul.2, 2015.
- [41] O. Jonah, S. V. Georgakopoulos and M. M. Tentzeris, "Orientation insensitive power transfer by magnetic resonance for mobile devices," in *IEEE Wireless Power Transfer (WPT)*, Perugia, 2013, pp. 5-8.
- [42] C. Park, S. Lee, G. Cho, S. Choi, and Chun T. Rim, "Two dimensional inductive power transfer system for mobile robots using evenly displaced multiple pickups," *IEEE Transactions on Industrial Applications*, vol. 50, no. 1, pp. 558-565, Jan. 2014.

- [43] H. Li, G. Li, X. Xie, Y. Huang and Z. Wang, "Omnidirectional wireless power combination harvest for wireless endoscopy," 2014 IEEE Biomedical Circuits and Systems Conference (BioCAS) Proceedings, Lausanne, 2014, pp. 420-423.
- [44] W. Ng, C. Zhang, D. Lin, and S. Hui, "Two- and three dimensional omnidirectional wireless power transfer," IEEE Transactions on Power Electronics, vol. 29, no. 9, pp. 4470-4474, Jan. 2014.
- [45] C. Zhang, D. Lin and S. Y. Hui, "Basic Control Principles of Omnidirectional Wireless Power Transfer," IEEE Transactions on Power Electronics, vol. 31, no. 7, pp. 5215-5227, July 2016.
- [46] B. H. Choi; E. S. Lee.; Y. H. Sohn, G. C. Jang, C. T. Rim, "Six Degrees of Freedom Mobile Inductive Power Transfer by Crossed Dipole Tx and Rx Coils," IEEE Transactions on Power Electronics, vol.31, no.4, pp.3252-3272, April 2016.
- [47] E. S. Lee, Y. H. Sohn, B. G. Choi, S. H. Han and C. T. Rim, "A Modularized IPT With Magnetic Shielding for a Wide-Range Ubiquitous Wi-Power Zone," IEEE Transactions on Power Electronics, vol. 33, no. 11, pp. 9669-9690, Nov. 2018.
- [48] Ming Lu, "Synergetic Attenuation of Stray Magnetic Field in Inductive Power Transfer", Ph.D. dissertation, Virginia Tech, 2017.
- [49] C. Zheng et al., "High-Efficiency Contactless Power Transfer System for Electric Vehicle Battery Charging Application," IEEE Journal of Emerging and Selected Topics in Power Electronics, vol. 3, no. 1, pp. 65-74, March 2015.
- [50] Q. Chen, S. C. Wong, C. K. Tse and X. Ruan, "Analysis, Design, and Control of a Transcutaneous Power Regulator for Artificial Hearts," IEEE Transactions on Biomedical Circuits and Systems, vol. 3, no. 1, pp. 23-31, Feb. 2009.
- [51] W. Zhang, S. Wong, C. K. Tse and Q. Chen, "Design for Efficiency Optimization and Voltage Controllability of Series-Series Compensated Inductive Power Transfer Systems," IEEE Transactions on Power Electronics, vol. 29, no. 1, pp. 191-200, Jan. 2014.
- [52] D. Lin; C. Zhang; S. Y. R. Hui, "Mathematical Analysis of Omnidirectional Wireless Power Transfer: Part-II 3-Dimensional Systems," IEEE Transactions on Power Electronics, vol. no.99, pp.1-1

- [53] W. X. Zhong and S. Y. R. Hui, "Maximum Energy Efficiency Tracking for Wireless Power Transfer Systems," *IEEE Transactions on Power Electronics*, vol. 30, no. 7, pp. 4025-4034, July 2015.
- [54] X. Qu, Y. Jing, H. Han, S. Wong and C. K. Tse, "Higher Order Compensation for Inductive-Power-Transfer Converters With Constant-Voltage or Constant-Current Output Combating Transformer Parameter Constraints," *IEEE Transactions on Power Electronics*, vol. 32, no. 1, pp. 394-405, Jan. 2017.
- [55] J. Larsson, "Electromagnetics from a quasi-static perspective," *American Journal of Physics*, vol. 75, no. 3, 2007.
- [56] J. Feng, Q. Li and F. C. Lee, "Coil and Circuit Design of Omnidirectional Wireless Power Transfer System for Portable Device Application," 2018 IEEE Energy Conversion Congress and Exposition (ECCE), Portland, OR, 2018, pp. 914-920.
- [57] M. T. Mehari et al., "Efficient Identification of a Multi-Objective Pareto Front on a Wireless Experimentation Facility," *IEEE Transactions on Wireless Communications*, vol. 15, no. 10, pp. 6662-6675, Oct. 2016.
- [58] M. Lu and K. D. T. Ngo, "Pareto fronts for coils' efficiency versus stray magnetic field in inductive power transfer," in *IEEE PELS Workshop on Emerging Technologies: Wireless Power Transfer (WoW)*, Knoxville, TN, 2016, pp. 140-144.
- [59] W. Zhang and C. C. Mi, "Compensation Topologies of High-Power Wireless Power Transfer Systems," *IEEE Transactions on Vehicular Technology*, vol. 65, no. 6, pp. 4768-4778, June 2016.
- [60] B. Lu, W.D. Liu, Y. Liang, F. C. Lee and J. D. van Wyk, "Optimal design methodology for LLC resonant converter," in *Applied Power Electronics Conference and Exposition (APEC)*, 2006.
- [61] B. Hesterman, *Analysis and modeling of magnetic coupling*. Advanced Energy Industries, Tech. Rep., 2007. <http://www.denverpels.org>.
- [62] J. Feng, M. Fu, Q. Li and F. C. Lee, "Resonant converter with coupling and load independent resonance for omnidirectional wireless power transfer application," 2017 IEEE Energy Conversion Congress and Exposition (ECCE), Cincinnati, OH, 2017, pp. 2596-2601.

- [63] M. Liu, C. Zhao, J. Song and C. Ma, "Battery Charging Profile-Based Parameter Design of a 6.78-MHz Class E2 Wireless Charging System," *IEEE Transactions on Industrial Electronics*, vol. 64, no. 8, pp. 6169-6178, Aug. 2017.
- [64] R. Tseng, B. von Novak, S. Shevde and K. A. Grajski, "Introduction to the alliance for wireless power loosely-coupled wireless power transfer system specification version 1.0," 2013 IEEE Wireless Power Transfer (WPT), Perugia, 2013, pp. 79-83.
- [65] Y. Wang, H. Wang, T. Liang, X. Zhang, D. Xu and L. Cai, "Analysis and design of an LCC/S compensated resonant converter for inductively coupled power transfer," 2017 IEEE Transportation Electrification Conference and Expo, Asia-Pacific, Harbin, 2017, pp. 1-5.
- [66] M. Fu, Z. Tang and C. Ma, "Analysis and Optimized Design of Compensation Capacitors for a Megahertz WPT System Using Full-Bridge Rectifier," in *IEEE Transactions on Industrial Informatics*, vol. 15, no. 1, pp. 95-104, Jan. 2019.
- [67] S. Park and J. M. Rivas, "Design of a Class-DE Rectifier with Shunt Inductance and Nonlinear Capacitance for High-Voltage Conversion," in *IEEE Transactions on Power Electronics*, vol. 33, no. 3, pp. 2282-2294, March 2018.
- [68] J. Feng, Q. Li and F. C. Lee, "Omnidirectional wireless power transfer for portable devices," 2017 IEEE Applied Power Electronics Conference and Exposition (APEC), Tampa, FL, 2017, pp. 1675-1681.
- [69] Texas Instruments, "I2C Multi-Chemistry Battery Buck-Boost Charge Controller With System Power Monitor and Processor Hot Monitor" bq25703A datasheet, May 2017.
- [70] C. Zhang, D. Lin and S. Y. R. Hu, "Efficiency optimization method of inductive coupling wireless power transfer system with multiple transmitters and single receiver," 2016 IEEE Energy Conversion Congress and Exposition (ECCE), Milwaukee, WI, 2016, pp. 1-6.
- [71] Prasad Kumara Sampath Jayathurathnage, A. Alphones, D. Mahinda Vilathgamuwa, Andrew Ong, "Optimum Transmitter Current Distribution for Dynamic Wireless Power Transfer With Segmented Array", *Microwave Theory and Techniques IEEE Transactions on*, vol. 66, no. 1, pp. 346-356, 2018.

- [72] J. Yin, D. Lin, T. Parisini and S. Y. Hui, "Front-End Monitoring of the Mutual Inductance and Load Resistance in a Series–Series Compensated Wireless Power Transfer System," in *IEEE Transactions on Power Electronics*, vol. 31, no. 10, pp. 7339-7352, Oct. 2016.
- [73] D. Ahn and S. Hong, "Effect of Coupling Between Multiple Transmitters or Multiple Receivers on Wireless Power Transfer," *IEEE Transactions on Industrial Electronics*, vol. 60, no. 7, pp. 2602-2613, July 2013.
- [74] N. Ha-Van and C. Seo, "Analytical and Experimental Investigations of Omnidirectional Wireless Power Transfer Using a Cubic Transmitter," *IEEE Transactions on Industrial Electronics*, vol. 65, no. 2, pp. 1358-1366, Feb. 2018.
- [75] A. Sharma, G. Singh, D. Bhatnagar, I. J. Garcia Zuazola and A. Perallos, "Magnetic field forming Using Planar Multicoil Antenna to Generate Orthogonal H-Field Components," *IEEE Transactions on Antennas and Propagation*, vol. 65, no. 6, pp. 2906-2915, June 2017.
- [76] Z. Dai, Z. Fang, H. Huang, Y. He and J. Wang, "Selective Omnidirectional Magnetic Resonant Coupling Wireless Power Transfer With Multiple-Receiver System," *IEEE Access*, vol. 6, pp. 19287-19294, 2018.
- [77] J. Feng, Q. Li and F. C. Lee, "Soft Switching Realization of LCCL-LC Resonant Converter for Wireless Power Transfer Application," 2019 IEEE Applied Power Electronics Conference and Exposition, Anaheim, CA, USA, 2019, pp. 664-670.
- [78] Brijesh Kumar Kushwaha, Gautam Rituraj, Praveen Kumar, "3-D Analytical Model for Computation of Mutual Inductance for Different Misalignments With Shielding in Wireless Power Transfer System", *Transportation Electrification IEEE Transactions on*, vol. 3, no. 2, pp. 332-342, 2017.
- [79] J. Feng, Q. Li, F. Lee and M. Fu, "LCCL-LC Resonant Converter and Its Soft Switching Realization for Omnidirectional Wireless Power Transfer Systems," in *IEEE Transactions on Power Electronics*.
- [80] M. Fu, H. Yin and C. Ma, "Megahertz Multiple-Receiver Wireless Power Transfer Systems With Power Flow Management and Maximum Efficiency Point Tracking," *IEEE Transactions on Microwave Theory and Techniques*, vol. 65, no. 11, pp. 4285-4293, Nov. 2017.

- [81] Wireless Power Consortium, "The Qi Wireless Power Transfer System Power Class 0 Specification," Part 1 and 2: Interface Definitions Version 1.2.2, Apr. 2016.
- [82] S. C. Tang, S. Y. Hui and H. S. -. Chung, "Evaluation of the shielding effects on printed-circuit-board transformers using ferrite plates and copper sheets," in *IEEE Transactions on Power Electronics*, vol. 17, no. 6, pp. 1080-1088, Nov. 2002.
- [83] M. Duffy, S. Kulkarni and S. Roy, "Improved Shielding Performance Using High Permeability Electroplated Thin Films in Printed Circuit Boards," in *IEEE Transactions on Magnetics*, vol. 47, no. 10, pp. 4282-4285, Oct. 2011.
- [84] H. Kim, C. Song, D. Kim and J. Kim, "Design of conductive shield for wireless power transfer system for electric vehicle considering automotive body," 2015 IEEE International Symposium on Electromagnetic Compatibility (EMC), Dresden, 2015, pp. 1369-1374.
- [85] International Commission on Non-Ionizing Radiation Protection, "ICNIRP guidelines for limiting exposure to time-varying electric, magnetic and electromagnetic fields (up to 300GHz)," *Health Phys.*, vol. 74, no. 4, pp. 494–522, 1998.
- [86] IEEE standard for Safety Levels With Respect to Human Exposure to Radio Frequency Electromagnetic Fields 3 kHz to 300 GHz, IEEE, IEEE Std. C96.1–2005, Apr. 2006.
- [87] [https://www.ecfr.gov/cgi-bin/retrieveECFR?gp=1&SID=8006cf4e2b6ab49e2ea4789cf715363e&ty=HTML&h=L&mc=true&r=SECTION&n=se47.1.1\\_11310](https://www.ecfr.gov/cgi-bin/retrieveECFR?gp=1&SID=8006cf4e2b6ab49e2ea4789cf715363e&ty=HTML&h=L&mc=true&r=SECTION&n=se47.1.1_11310)
- [88] C.T. Burket, "Magnetic shield influence on low power wireless power designs," 2013 Wireless Power Summit, Austin, Texas, 2013.
- [89] <https://www.langer-emv.de/en/category/lf-passive-100-khz-bis-50-mhz/36>
- [90] J. Feng, Q. Li, F. C. Lee and M. Fu, "Transmitter Coils Design for Free-Positioning Omnidirectional Wireless Power Transfer System," in *IEEE Transactions on Industrial Informatics*, vol. 15, no. 8, pp. 4656-4664, Aug. 2019.
- [91] J. Feng, Q. Li and F. C. Lee, "A Square-Shaped Omnidirectional Wireless Charging Bowl with a Double Layer Electromagnetic Shield for Portable Device Applications," *2019 IEEE*

*Energy Conversion Congress and Exposition (ECCE)*, Baltimore, MD, USA, 2019, pp. 4961-4966.

# **Appendix: A Planar Omnidirectional Wireless Power Transfer System**

## **A.1 Introduction**

In previous chapter, a three dimensional wireless charging setup is proposed. However, the three dimensional structure might not be favorable for certain application. For example, it is difficult to integrate the charging setup within a desk. Considering this, a planar charging setup is desired for certain applications. For the conventional planar charging pad, there are two main limitations as shown in Fig A. 1 and Fig A. 2: 1. the energy transfer range is limited in short range; 2. the energy transfer is directional. To solve limitation 1, a large spiral transmitter coil with high frequency operation should be adopted as illustrated in Chapter 1.4. To deal with limitation 2, omnidirectional magnetic field distribution is desired above the charging pad. In [46] and [75], planar transmitter coils structure is proposed to generate two dimensional rotating magnetic field; however, the two dimensional rotating field cannot provide fully orientation insensitive charging for a planar receiver coil. Therefore, a planar transmitter coils structure with omnidirectional field in three dimensional manner is proposed in the appendix.

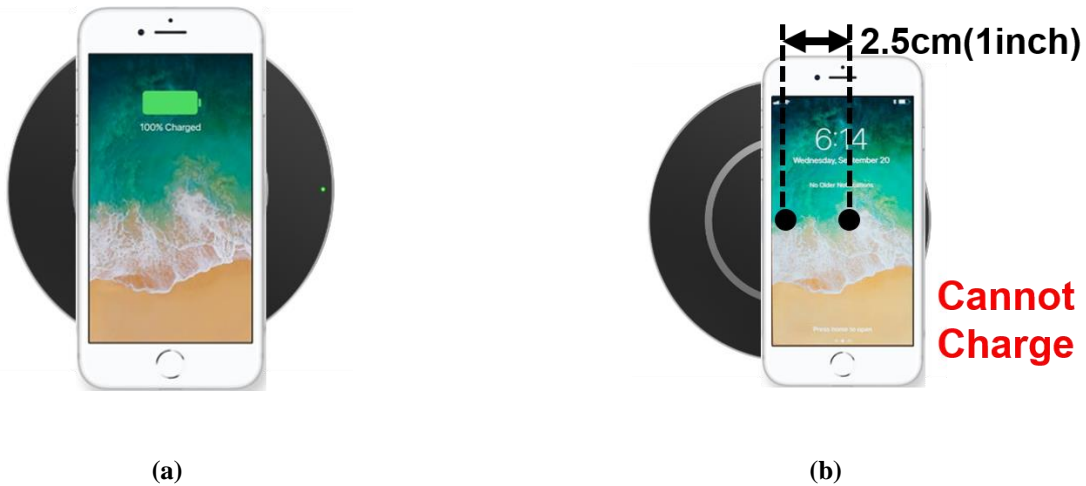


Fig A. 1. Two charging scenario for smart phone device of a commercial Qi charging pad. (a). There is no misalignment between transmitter and receiver. (b). There is misalignment between transmitter and receiver.



Fig A. 2. Two charging scenario for wearable device of a planar charging pad (a). Receiver device is in perpendicular with the magnetic field. (b). Receiver device is in parallel with the magnetic field.

## A.2 Proposed Planar Transmitter Coils Structure

As illustrated by Chapter 2, it is essential to generate three orthogonal magnetic field vector basis with the transmitter coils structure in an omnidirectional WPT system. A planar transmitter coils structure shown in Fig A. 3(a) is proposed to induce three orthogonal magnetic field vector basis. There are three sets of transmitter coils: coil x1 and coil x2; coil y1 and coil y2; coil z in the proposed coils structure. As shown in Fig A. 3(b), (c) and (d), the magnetic field induced by coil

x, coil y and coil z at point A is in x, y and z direction separately. The total magnetic field at point A is the vector summation of three magnetic field vector:

$$\mathbf{B} = f(i_1)\mathbf{B}_x + f(i_2)\mathbf{B}_y + f(i_3)\mathbf{B}_z$$

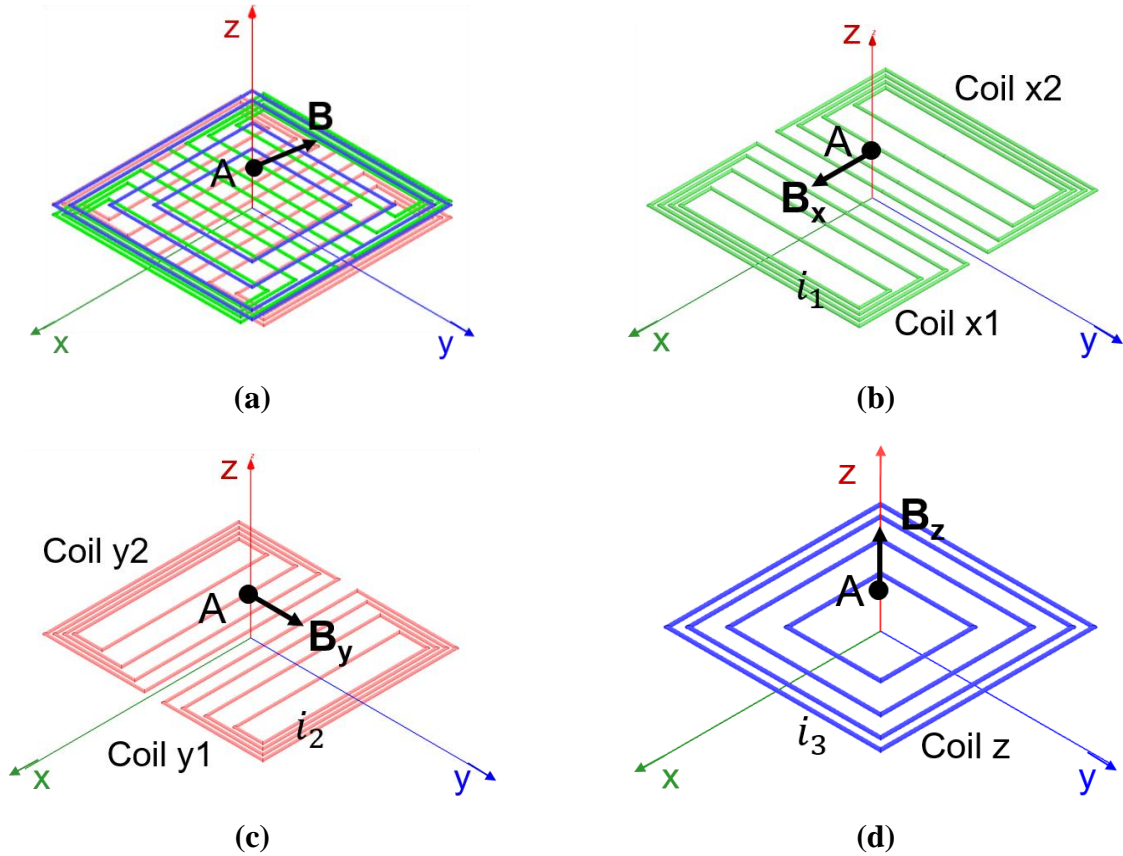


**Fig A. 3. The proposed planar transmitter coils structure. (a). Three sets of transmitter coils. (b). Transmitter coil x set. (c). Transmitter coil y set. (d). Transmitter coil z.**

By controlling the excitation current flowing through three transmitter coils set, the total magnetic field can be directed in any direction. With the modulated excitation current, the total magnetic field vector induced at point A for different time instants is shown in Fig A. 4, which is obtained by 3D finite element analysis software. As demonstrated by Fig A. 4, the omnidirectional field is achieved at point A with the proposed transmitter coils structure in a time perspective.

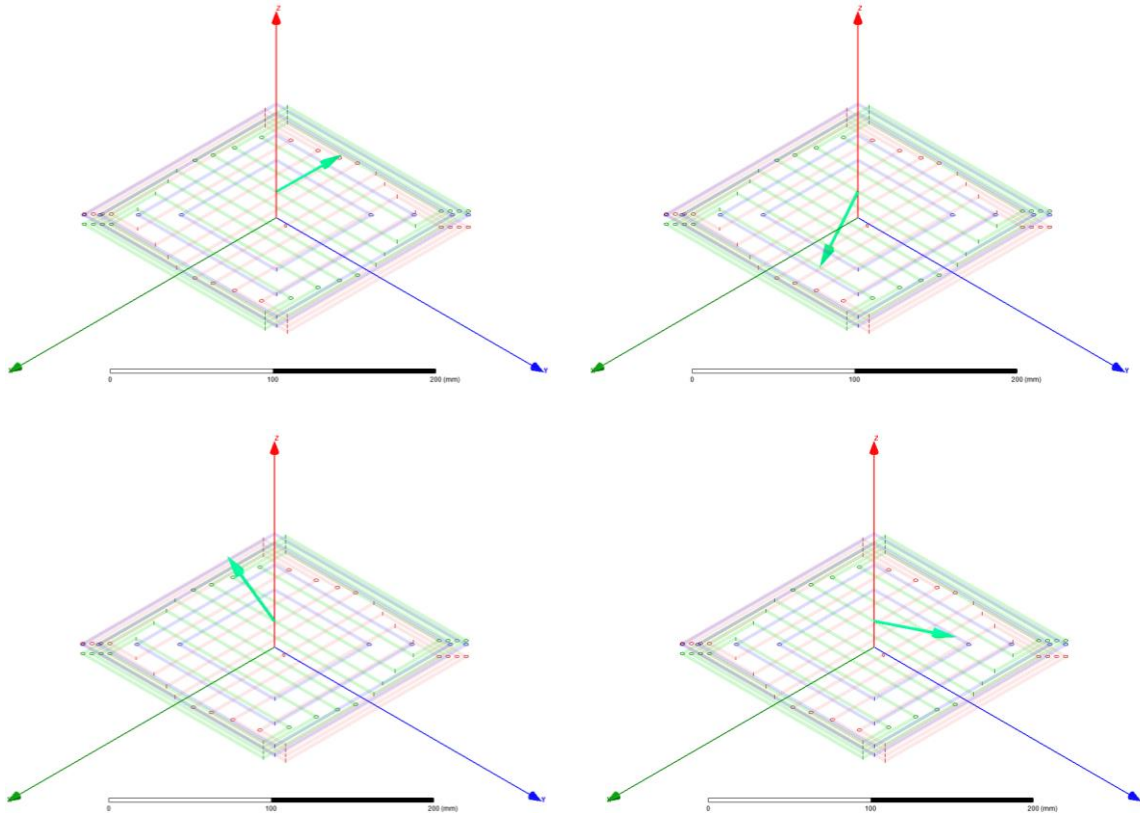


**Fig A. 4. The total magnetic field vector induced at point A for different time instants.**

Similarly, the magnetic field distribution above the planar charging surface at different time instants is shown in Fig A. 5. As illustrated by Fig A. 5, the omnidirectional field distribution is induced in the region above the charging setup. Therefore, there is no need to align the receiver coil with the transmitter coil anymore. The transmitter can transfer energy in any direction and the charging orientation freedom is greatly improved.

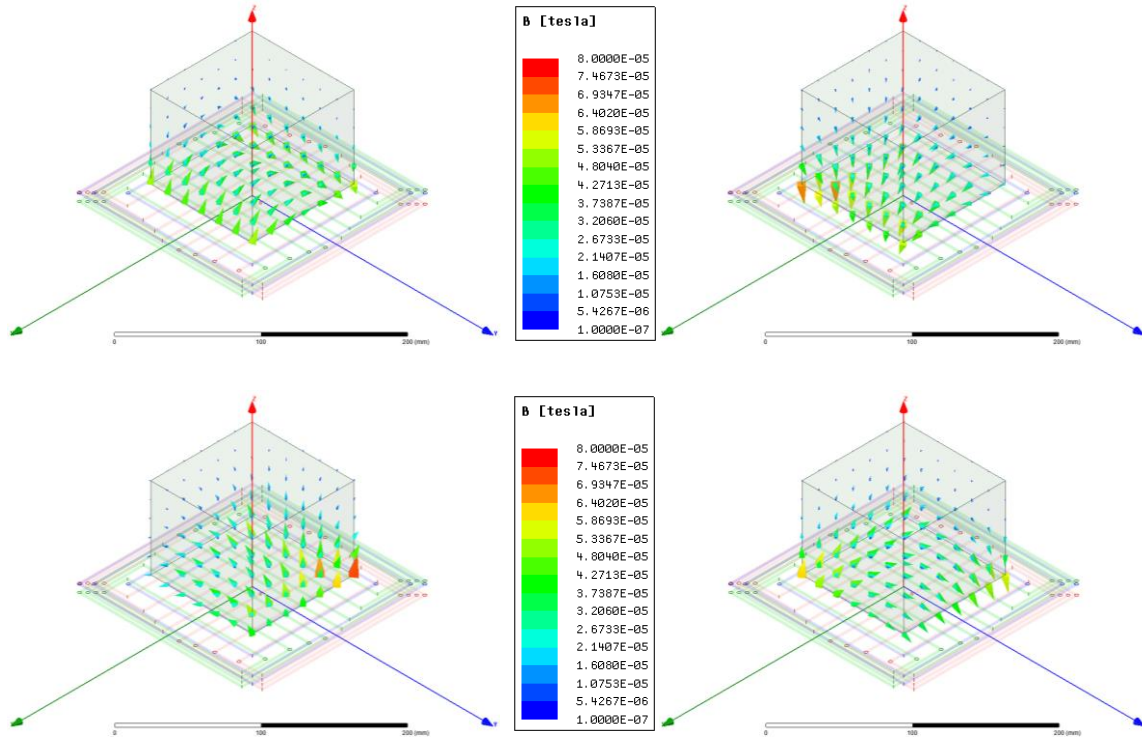


**Fig A. 5. The magnetic field distribution above the proposed transmitter coils structure.**

### **A.3 Reduce Parasitic Capacitances**

The mature PCB fabrication technology can be adopted to implement the proposed planar transmitter coils structure in a low-cost manner. There are three different transmitter coils sets in the proposed structure and different transmitter coil sets will be printed in different layers of the PCB. For a standard 4 layer PCB implementation, the distance between layer 1 and layer 2 is only 0.3mm. The small distance increases the parasitic capacitance between different transmitter coils set. The capacitance matrix of the proposed coils structure in a standard 4 layer PCB board with FR4 substrate is shown in Fig A. 6. Herein, the transmitter coil set x is in layer 1; the transmitter coil z is in layer 2 and the transmitter coil set y is in layer 4. In the capacitance matrix, there are two types parasitic capacitance: inter-coil capacitance between two different coils and equivalent parallel capacitance (EPC) of single coil. The equivalent parallel capacitance is in the diagonal

position of the matrix. For example, the EPC of z coil is 72pF. Since the self-inductance of z coil is 3uH, the self-resonance frequency of z coil is 10.8MHz. To follow the Airfuel wireless charging standard, the operating frequency is selected as 6.78MHz. Therefore, the EPC is so large that the self-resonance will happen near the operating frequency, which means large electric field and extra dielectric loss. In addition, the large inter-coil capacitance leads to unnecessary circulation energy flowing among different transmitter coils and the circulating energy also results in extra loss. Considering this, it is essential to reduce the parasitic capacitances.

To reduce the parasitic capacitance, the transmitter coils structure is modified to minimize the overlapping among different transmitter coils as shown in Fig A. 7. Compared with Fig A. 6, the width of coil x, y decreases to reduce overlapping between coil x and coil y in the corner region of the PCB board. Meanwhile, z coil is modified to circular shape from square shape to reduce overlapping with coil x and coil y. After the modification, the parasitic capacitance matrix is shown in Fig A. 7. As demonstrated by the capacitance matrix, the parasitic capacitance reduces more than 50% for most cases. The self-resonance frequency of z coils now moves to 20MHz with the modified design, which is away from the operating frequency 6.78MHz.

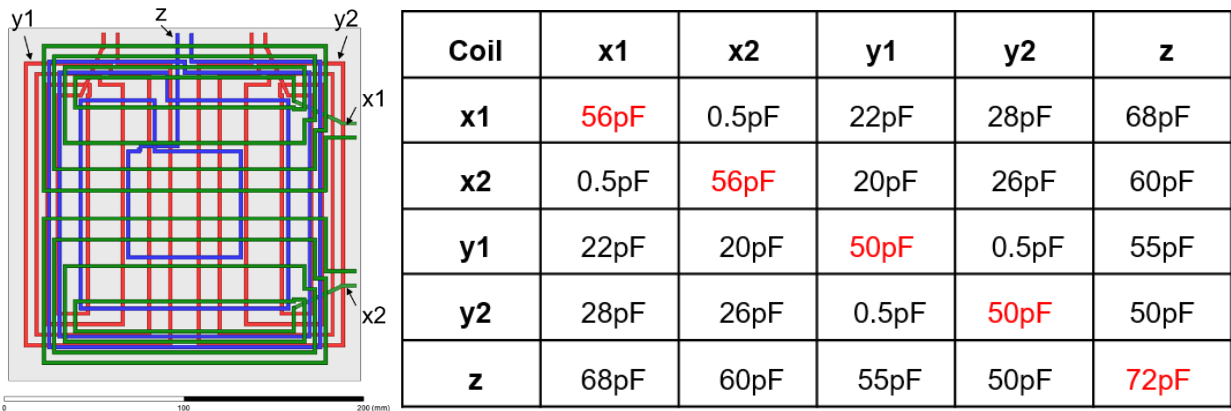


Fig A. 6. The capacitance matrix among different transmitter coils before modification.



Fig A. 7. The capacitance matrix among different transmitter coils after modification.

To further reduce the parasitic capacitances, the distance among different layers is increased. There are three sets of coils in the proposed coils structure and one PCB layer is wasted when it is implemented with a standard four layer board. Regarding this, a customized three layer PCB with larger distance among different layers is utilized to implement the proposed coils structure. The stack up of two different implementations is shown in Fig A. 8. The capacitance matrix with the 3 layer PCB implementation is demonstrated in Fig. A. 9 and the parasitic capacitance is further reduced after the distance between different layers increases.

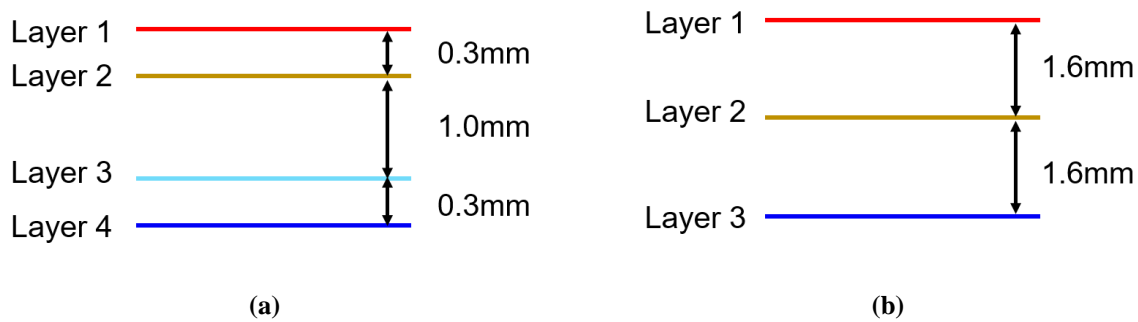


Fig A. 8. The stack up of 4 layer standard PCB and 3 layer customized PCB. (a). 4 layer standard PCB. (b). 3layer customized PCB.



Fig A. 9. The capacitance matrix among different transmitter coils with 3 layer customized PCB.

### A.4 Experimental Results

A 200 x 200 mm planar charging platform with the proposed transmitter coils structure is built with three layer PCB as shown in Fig A. 10(a). A 65 x 50 mm rectangular receiver coil (4.7 uH, 0.6  $\Omega$ ) for a typical smart phone is fabricated. To describe the receiver coil positioning in the charging platform, a planar coordinate system is built as shown in Fig A. 10(b). Therefore, the x, y coordinate of the center of the receiver coil is utilized to describe the positioning of the receiving device.



Fig A. 10. The picture of the planar charging pad. (a). Without smart phone receiver device. (b). With smart phone receiver device.

In the charging test, only z coil is selectively excited since the smart phone receiver lay down on the charging surface, and other transmitter coils are not excited. The z coil is driven by the LCCL-LC resonant converter in chapter 3. The output voltage and system efficiency under different receiving positioning, is shown in Fig A. 11 and Fig A. 12. Due to the symmetry of the transmitter coils structure, test results in only one quarter of the charging pad are plotted. As shown in Fig A. 12, the system efficiency is 80~87 % at 5 W output for all possible receiver positioning.

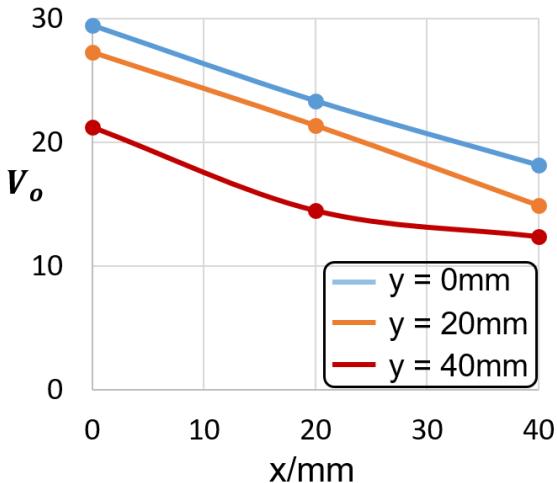


Fig A. 11. The measured output voltage for the smart phone receiver under different positioning.

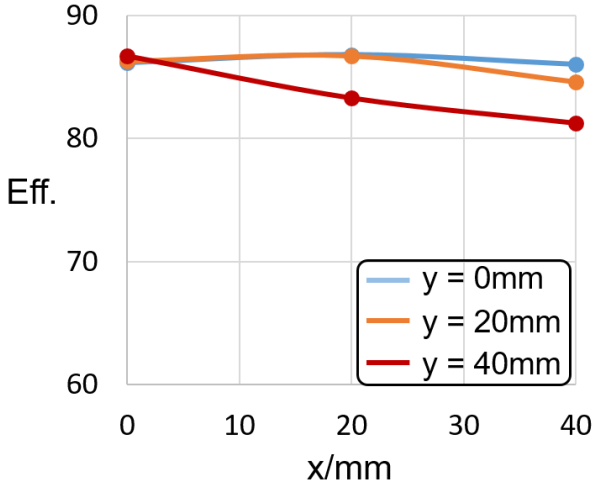


Fig A. 12. The measured system efficiency for the smart phone receiver under different positioning.

A 35 x 35mm square receiver coil (7.0  $\mu\text{H}$ , 1.1  $\Omega$ ) for an Apple Watch is fabricated to verify free positioning and omnidirectional powering characteristics. When the receiver coil stands on the base, the orientation is flexible and is characterized by yaw rotation angle  $\theta$ , as defined in Fig A. 13. To generate horizontal magnetic field for the standing receiving device. The x and y coil are both excited with 6.78 MHz sinusoidal current and the excitation current has 90° phase difference with each other to generate rotating field. With the modulation excitation current, the output voltage and system efficiency test results for different orientations for two positions (0, 0mm) and (30, 30mm) are shown in Fig A. 14 and Fig A. 15.

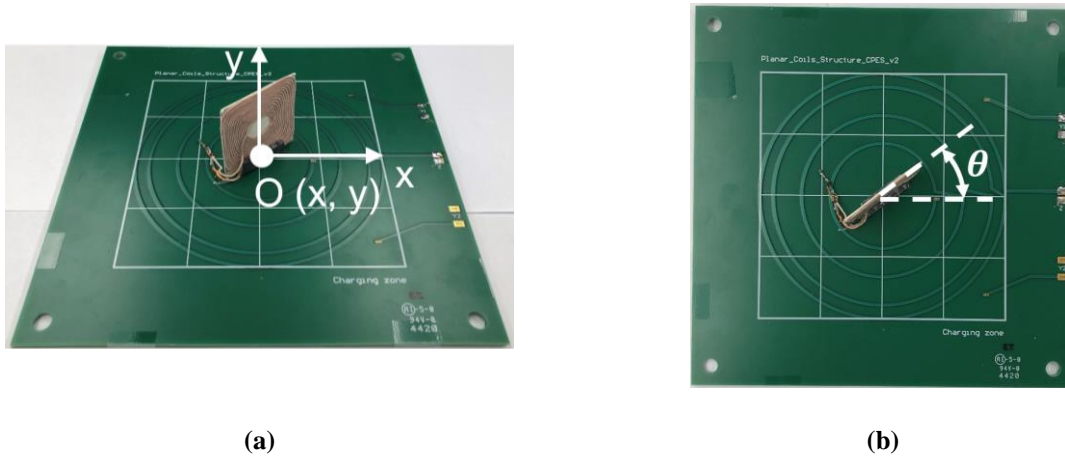


Fig A. 13. The picture of the testing setup for a wearable device. (a). 3D front view. (b). Top view.

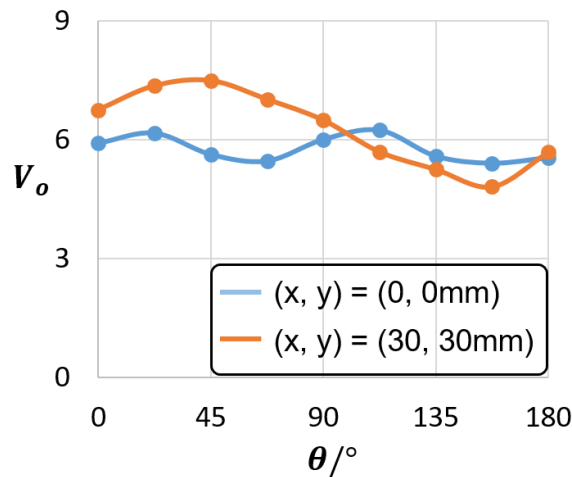
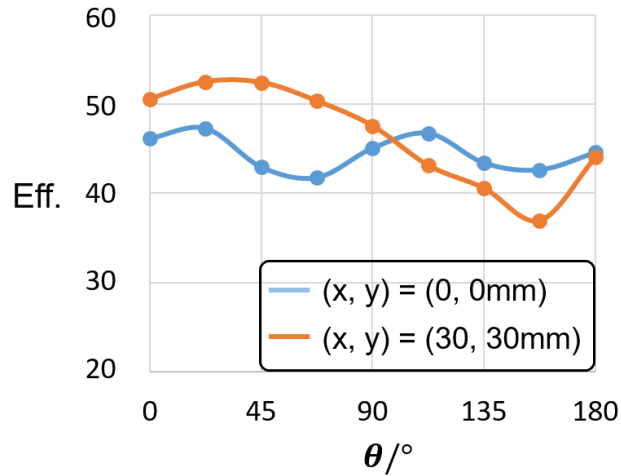


Fig A. 14. The measured output voltage for the small wearable device with different orientations under different positioning.



**Fig A. 15. The measured system efficiency for the small wearable device with different orientations under different positioning.**

According to the measurement results, the output voltage is 4.8 ~7.5V and the system efficiency is 38 ~52% for different orientations of a smart watch receiver under different positioning in the setup. Free positioning and omnidirectional powering characteristics are verified. There is no longer a need to align a small portable device receiver unit with the transmitter coils, making it more convenient for customer use. Compared with the charging bowl structure in chapter 2, the proposed planar charging platform is much easier to integrate with the common furniture at home.